論文 / 著書情報
Article / Book Information

題目(和文)	磁性ナノ粒子を用いた磁気バイオセンシングのための交流磁化の周波数スペクトル解析に関する研究
Title(English)	Study on analysis of frequency spectrum in alternating current magnetization of magnetic nanoparticles for magnetic biosensing
著者(和文)	CHEN YE
Author(English)	Ye Chen
出典(和文)	学位:博士(工学), 学位授与機関:東京工業大学, 報告番号:甲第12628号, 授与年月日:2023年12月31日, 学位の種別:課程博士, 審査員:北本 仁孝,曽根 正人,SLAVAKIS KONSTANTINO,林 智広,藤枝 俊宣,CHANG TSO-FU
Citation(English)	Degree:Doctor (Engineering), Conferring organization: Tokyo Institute of Technology, Report number:甲第12628号, Conferred date:2023/12/31, Degree Type:Course doctor, Examiner:,,,,,
学位種別(和文)	博士論文
Type(English)	Doctoral Thesis

Study on analysis of frequency spectrum in alternating current magnetization of magnetic nanoparticles for magnetic biosensing

Ye Chen

Doctoral Dissertation

submitted to the
Department of Materials Science and Engineering
School of Materials and Chemical Technology
Tokyo Institute of Technology

in partial fulfillment of the requirements for the degree of
Doctor of Engineering
Human Centered Science and Biomedical Engineering Major

October 2023

Doctoral supervisor: Professor Yoshitaka Kitamoto
Professor Konstantinos Slavakis

Abstract

As a wash-free and simple method for detecting biomolecules, magnetic susceptometry based biosensing method provides both simplicity in manipulation and comparable accuracy in detection. In such method, the analysis of the frequency spectrum in the alternating current (AC) magnetization of magnetic nanoparticles (MNPs) is crucial. In previous studies, it was presumed that the interactions between MNPs and biomolecules were homogeneous. Such an assumption is inaccurate in real-world applications, limiting the applicability and accuracy of magnetic biosensing-based on Brownian relaxation. To overcome the above issue, this research proposes a method for estimating the information including distribution and concentration of MNPs via solving an inverse problem with Debye relaxation model or a proposed experimental model. Then we establish the relationship between the estimated information and the concentration of target molecules for magnetic biosensing. The feasibility of using the proposed method and established relationship for biosensing are confirmed in ferrogel and liquid biomolecule detection situations. From the results, the concentrations of target molecules estimated via the proposed method and established relationship show higher consistency with the true concentrations of target molecules comparing to the previous relaxation frequency-based method. It suggests the potential of the proposed method for establishing a more precise relationship between MNPs and target molecules to achieve more accurate detection of target molecules than the previous relaxation frequency-based method.

Table of contents

List of figures

List of table

1 General introduction

The world has been significantly impacted by the COVID-19 pandemic. Due to a lack of available medical resources after infection, many people have perished. Additionally, even in this post-COVID-19 era, many people are still struggling with the long-term impacts of the virus [1]. As a result, in this post-COVID-19 era, health monitoring, early-stage diagnosis and prevention are as essential as the innovative treatment technologies. Currently, conventional methods for diagnosis include enzyme-linked immunosorbent assay (ELISA) [2], polymerase chain reaction (PCR) [3,4] and so on. Although above methods provide high sensitivities, they are time-consuming, labor-intensive, and expensive [5]. The development of biosensing has attracted a great deal of interest as a means of overcoming the problems with conventional methods.

Biosensing is the detection of target biomarkers such as enzymes, DNA [6,7], RNA [8,9], antibodies [10,11], antigen [12], and so on. In biosensing, generally, there are two steps [13]. The first step is the recognition/immobilization of target biomarkers, and the second step is the detection of target biomarkers via properties of the transducer. In the first step, the recognition/immobilization is realized via specific biomolecule interactions such as avidin-biotin interaction, antibody-antigen interaction and so on. In the second step, the binding of target biomarkers can be measured by using various transduction techniques, such as electrochemical [14,15], calorimetric [16], optical [17,18] and magnetic [19] methods. In the second step, there are two main categories of detection methods which are label-based methods and label-free methods [20]. According to its name, label-free biosensing relies on changes in physicochemical properties such as surface charge, electrical impedance, index

of refraction and so on for detection [21]. Because of the development of nanotechnology, the sensitivity of label-free biosensing has been increasing [22,23] and its convenience of use is promising for the capital-intensive detection in the future. However, it is still challenging to detect the target biomarker in the complex medium where there are various biomarkers exist. And label-free biosensing is relatively less sensitive than label-based biosensing, in which signals are amplified by labels [24]. Because of this issue, it is still vital to develop artificial labels for biosensing. In the past decades, nanoparticles and nanostructures are mainly investigated as labels for biosensing due to their high surface to volume ratio and shape-dependent properties [25]. In the following sections, label-based biosensing using nanoparticles is reviewed and discussed.

1.1 Label-based biosensing using nanoparticles

In label-based biosensing, nanoparticle-based labels are used for capturing the target biomarkers and further quantitative measurements are performed by measuring characteristic response of labels. Characteristic response is the key point for label-based biosensing and determined by the physicochemical properties of materials of labels. For instance, gold nanoparticles are some of the most investigated nanoparticles for optical biosensing due to their easy fabrication, chemical stability and tunable optical properties [26] including localized surface plasmon resonance [27], surface enhanced Raman scattering [28], fuorescence [29], etc. In a second instance, magnetic nanoparticles (MNPs) are the only option for magnetic phenomena based biosensing because other types of nanomaterials exhibit an extremely low magnetic response.

Compared to other types of nanoparticles, the most significant features of MNPs are their ease of separation [30] and low background noise [31,32] during magnetic measurements. By using MNPs, it is easy to remove the unwanted biomarkers and enrich the target biomarkers, which are promising for further measurements. In addition, biomarkers exhibit nearly no magnetic background [33], allowing for highly sensitive measurements. Moreover, low magnetic background of matters except MNPs makes it easy to design biosensing systems and perform biosensing. For instance, for optical biosensing systems, it is crucial to consider the optical properties of the matter existing in the systems, as there is a risk that the optical readout could be affected by the matter (e.g., the colored component in the blood [34]). Thus, the design of biosensing systems and situations is limited. In contrast, for magnetic phenomena based biosensing systems, the magnetic field and the resulting magnetic readout have high transmissibility over a wide range of substances, including the majority of biomarkers and inorganic materials, allowing for greater flexibility in the design of the systems. Besides above features, MNPs also provide other features including tunable size and ease of surface modification, which are important for biosensing. The remarkable features of MNPs are concluded in the Fig 1-1. To fully use the features of MNPs especially low background noise during magnetic measurements, MNP-based biosensing in this thesis means magnetic phenomena based biosensing using MNPs as labels.

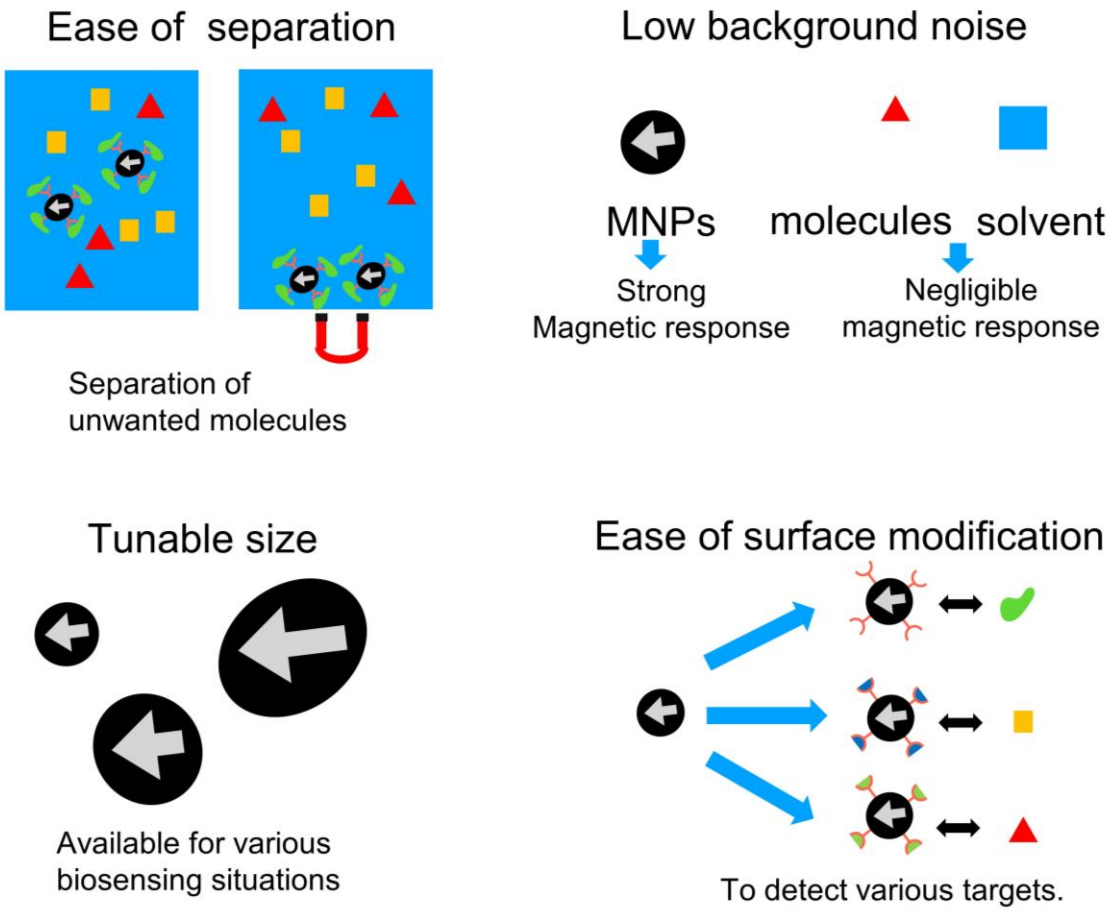

FIG. 1-1. Remarkable features of MNPs.

1.2 MNP-based biosensing and issue

Magnetoresistance (MR) sensors [35,36], Hall sensors [37,38], nuclear magnetic resonance (NMR) relaxometry [39,40], and magnetic susceptometry based biosensing based method [41,42] are representative examples of MNPs based biosensing. These methods employ two labeling strategies: the fixing strategy, employed in MR sensors and conventional SQUID magnetometry, and the clustering strategy, utilized in NMR relaxometry and magnetic susceptometry based biosensing method as shown in Fig. 1-2.

In the fixing strategy, MNPs are immobilized on the solid sensor surface through interactions with target biomarkers. The detection of biomarkers is achieved by measuring the MR or Hall effect of the immobilized MNPs. In contrast, the clustering strategy involves functionalizing MNPs with probes, which then bind to target biomarkers in the liquid phase. This results in the formation of MNP clusters or aggregations. Changes in the aggregation status of MNPs can be measured using NMR relaxometry or magnetic susceptometry based biosensing. NMR relaxometry specifically measures alterations in the transverse relaxation rate (T2) of water protons [43]. Magnetic susceptometry based biosensing measures changes in the relaxation behavior of MNPs [44]. One of the key advantages of fixing-based methods is their high sensitivity. However, these methods also come with drawbacks, such as the complexity involved in fabricating solid surfaces and the need for bound/free separation. On the other hand, clustering-based methods offer potential for simple and rapid detection compared to fixing-based strategies. While magnetic susceptometry based biosensing may have lower sensitivity than the aforementioned methods, it holds promise as a simple detection method, particularly in poverty areas where the fabrication of devices for MR sensors or NMR sensing devices is challenging. This is attributed to the simplicity of both the detection procedure such as wash-free and the fabrication of coil-based sensing devices.

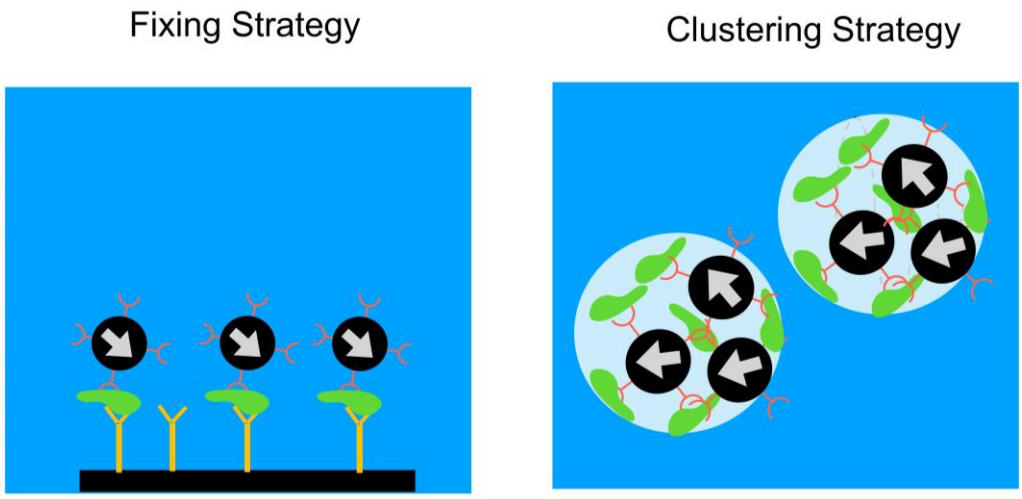

FIG. 1-2. Label strategies of MNP-based biosensing.

Although magnetic susceptometry based biosensing provides the potential for simple and low cost biosensing, the assumption in the traditional method based on the relaxation frequency limits the application ranges. Before describing the issue of magnetic susceptometry based biosensing, the mechanism of such method as shown in Fig. 1-3 is briefly reviewed. Magnetic susceptometry based biosensing in the liquid phase using alternating current (AC) magnetization spectra (In the present study, we use AC magnetization spectra instead of AC susceptibility spectra with the reason explained in **Section** 2.1) was proposed by Connolly and St. Pierre [45]. A frequency-dependent magnetic magnetization represents the magnetic response of MNP suspension in the AC magnetic fields. The AC magnetization spectra corresponds to the relaxation behaviors of MNPs. Brownian relaxation (rotational relaxation of MNPs) has been mainly employed to magnetic susceptometry based biosensing. As mentioned above, functionalized MNPs bind to biomolecules to form MNP clusters, resulting in larger effective hydrodynamic size. Because

the Brownian relaxation time increases with the increase of hydrodynamic size of MNPs [46] (detailed explanations of Brownian relaxation will be done in **Section** 2.1), the increase in the effective hydrodynamic size leads to an increase of effective Brownian relaxation time, which causes a decrease of effective relaxation frequency $f_{\text{peak}} = \frac{1}{2\pi\tau_B}$ in AC magnetization spectra [47].

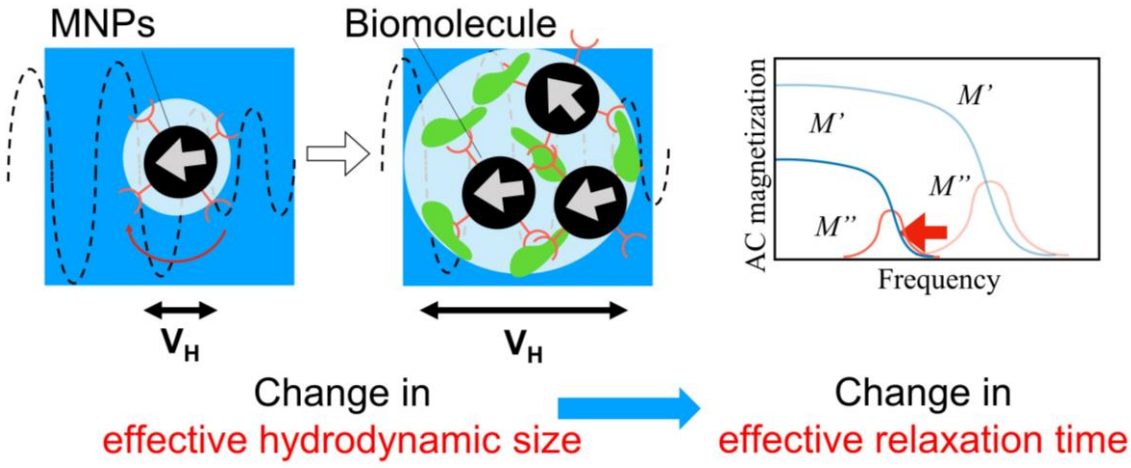

FIG. 1-3. Mechanism of magnetic susceptometry based biosensing.

As shown in Fig. 1-4, in the method based on the relaxation frequency, the assumption is that the distribution of MNP clusters is homogeneous. The increase of hydrodynamic size of MNP clusters is proportional to the increase of the amount of biomolecules. Because the effective relaxation time corresponds the effective hydrodynamic size, it is possible to use effective relaxation time, in other words, effective relaxation frequency to perform biosensing. Clustering between MNPs and biomolecules and their interaction are, however, heterogeneous as shown in Fig. 1-4 [48,49], and consequently various types of clusters, characterized by the number of MNP and biomolecules bound, conformations, and kinetic

constants as well as by the effective hydrodynamic size, are formed in the suspension as shown in Fig. 1-5(a) [50]. Thus, as shown in Fig. 1-4, in practical situations, when the change in the concentration of biomolecules is slight, there is only shape change occurred rather than a significant shift in the effective relaxation frequency in the AC magnetization spectrum. In such situation, a new method for analyzing the AC magnetization spectra and detecting biomolecule is necessary.

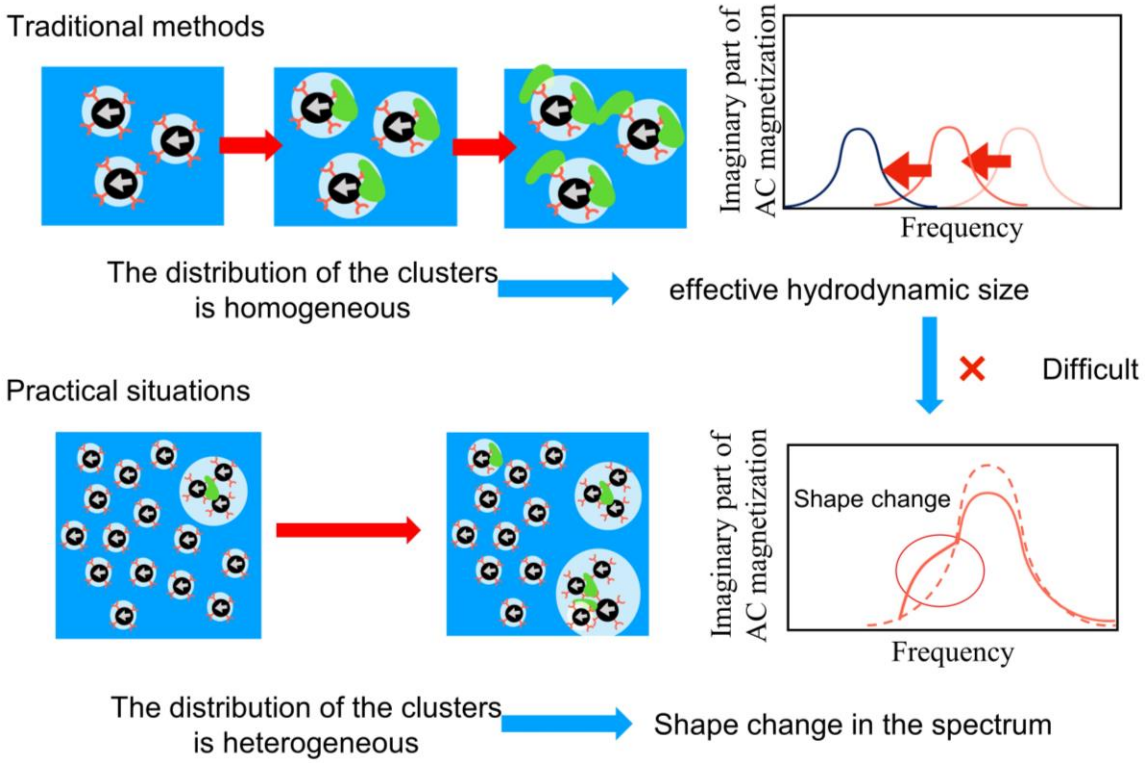

FIG. 1-4. Issue of the relaxation frequency based method for analyzing the AC magnetization spectra.

1.3 Original research approach

As described in **Section** 1.2, the assumption that the distribution of MNP clusters formed among MNPs and biomolecules is homogenous is not suitable for practical situations where

the distribution of the clusters is heterogeneous. The distribution of the various clusters corresponds to various amounts of biomolecules [51]. Therefore, identifying the distribution of each type of clusters enables to precisely estimate the amount of biomolecules [48]. Dynamic light scattering (DLS), which measures the hydrodynamic size distribution of MNPs, provides inaccurate results especially with coexistence of larger clusters in samples [52].

To overcome the above issue, we focus on the hydrodynamic size distribution of MNP clusters. As shown in Fig. 1-5, our assumption is that the AC magnetization spectra for functionalized MNPs and MNP clusters formed among MNPs and biomolecules dominated by Brownian relaxation are regarded as the linear superposition of AC magnetization spectra that are derived from clusters formed by MNPs and biomolecules [49]. By this assumption, the modulation in AC magnetization spectra including the shift in relaxation frequency and shape of spectra is caused by the change in the hydrodynamic size distribution of the clusters. Thus, it is possible to estimate the distribution of the clusters from AC magnetization spectra by using an inverse method. Bender et al. [53] reported the estimation of the hydrodynamic size distribution of MNPs from AC magnetization spectra by solving an inverse method. However, their estimation was based on Debye relaxation model, however, the model ignores the interaction such as the dipole-dipole interaction among MNPs and cannot be directly applied to complex clusters that involve biomolecules, resulting in inaccurate estimation of the distribution [54].

In the present study, we propose a method by estimating the hydrodynamic size distribution of major clusters as shown in Fig. 1-5 by solving an inverse problem. To overcome the issue of Debye relaxation model, we propose an experimental model to form the matrix equation

for the inverse problem. In addition, we not only focus on the distribution, but also on the mass concentration of MNPs. Moreover, the estimated information including the distribution and mass concentration of MNPs are used to establish models for biosensing.

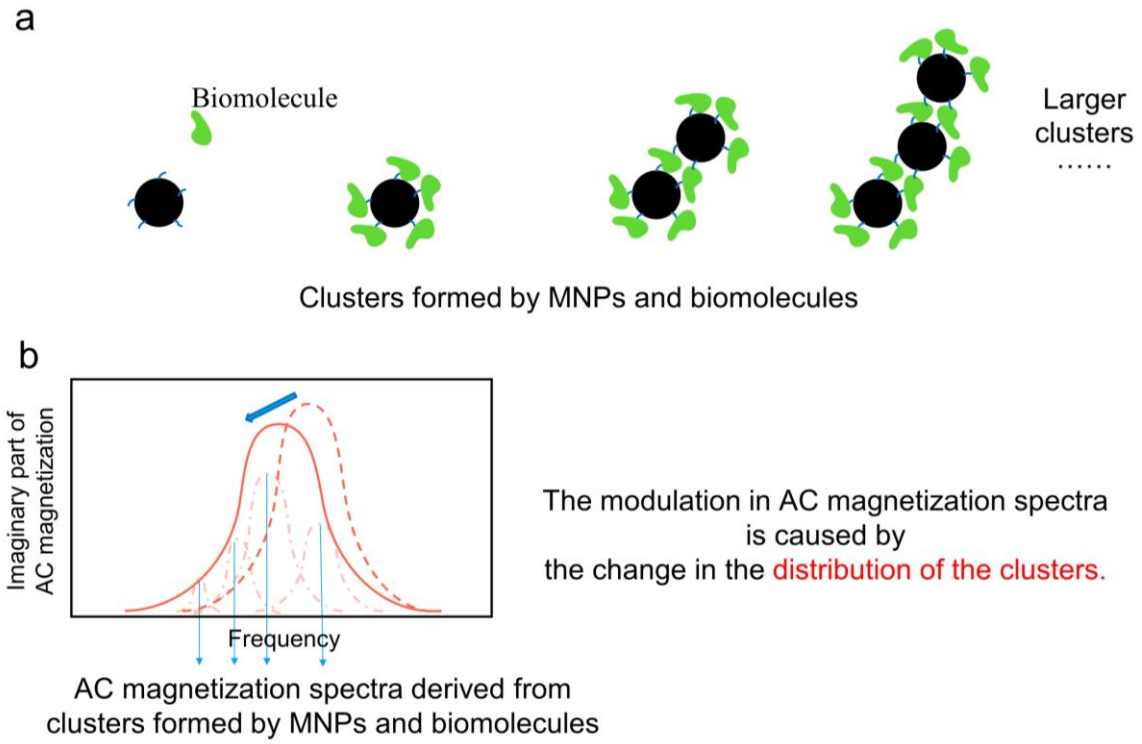

FIG. 1-5. Schematic illustration of (a) different types of MNP clusters with the presence biomolecules and (b) The assumption of the modulation in AC magnetization spectra.

1.4 Thesis aims and scope

In summary, after the COVID-19 pandemic, limited healthcare resources have struggled to meet the demands of large-scale treatment of infectious diseases, particularly in poverty areas. Therefore, simple yet reliable methods for health monitoring and biomarker detection have gained increasing attention. Magnetic susceptometry based biosensing is one such approach. A crucial aspect of magnetic susceptometry based biosensing involves AC

magnetization spectra. In the past, the application of magnetic susceptometry based biosensing has been limited by analysis methods based on the effective relaxation frequency. To address this issue, a novel analysis method is required. Considering that the distribution of MNPs plays a pivotal role in magnetic susceptometry based biosensing, the first aim of this study is to establish a method for estimating the hydrodynamic behavior of magnetic nanoparticles from the AC magnetization curve. Simultaneously, this research aims to validate the proposed method's feasibility through experimental demonstration of biosensing, thereby demonstrating its potential for future health monitoring and biomarker detection.

In brief, this research is to propose a method to estimate the information (which includes hydrodynamic size distribution and the mass concentration) of MNPs or MNP clusters from the AC magnetization spectra and investigate models to use the estimated information for biosensing. And then both simulation data and experimental data are used to confirm the feasibility of the proposed method. These are primarily specified by the following objectives:

1. To propose a method for estimating the information of MNP clusters from AC magnetization spectra.
2. To confirm the feasibility of proposed method for estimating the distribution of MNP clusters on the simulation data generated based on the Debye relaxation model.
3. To confirm the feasibility of the proposed method on the experimental data and establish models to use the estimated information for biosensing.
4. To confirm the feasibility of the proposed method for analyzing AC magnetization with fewer frequency points.

To achieve the above objectives, studies have been performed as following:

1. A method for estimating the information of MNP clusters from AC magnetization spectra is proposed. We discuss the method to form the matrix equation for the inverse problem in two situations where the interaction among MNPs inside cluster is negligible or not (Chapter 2).
2. The hydrodynamic size distributions of MNP clusters are estimated from simulated AC magnetization spectra and compared with the true distributions. The mass concentrations of MNP clusters are also estimated from simulated AC magnetization spectra (Chapter 3).
3. The proposed method is applied onto experimental data. A pH-sensitive magnetic hydrogel is synthesized and used to confirm the feasibility of the proposed method based on Debye relaxation model for estimating the mass concentration of MNPs. The estimated mass concentration of MNPs is used to for a demonstration of the detection of ammonia gas (Chapter 4). In addition, the hydrodynamic size distribution of MNP clusters formed by MNPs and biomolecules is estimated by proposed method based on an experimental model. Then the estimated distribution of MNP clusters and the amount of streptavidin are used to establish a linear regression model for demonstrating the detection of streptavidin (Chapter 5).
4. Experimental data used in chapter 4&5 is used to generated AC magnetization spectra with fewer frequency points. The proposed method is applied onto the reduced spectra and the detection of the ammonia gas and streptavidin as described in chapter 4&5 are used for evaluation (Chapter 6).

1.5 Significance of this study

In previous studies, relaxation frequency has been used as a factor for biosensing using magnetic susceptometry. However, due to multiple possible distributions that can correspond to an effective relaxation frequency, it is difficult for the method based on relaxation frequency to establish a one-to-one relationship between relaxation frequency and the concentration of biomolecules. In contrast, the proposed method in this study analyzes the whole AC magnetization spectra to estimate the information such as the hydrodynamic size distribution of MNP clusters rather than relying on a specific point such as relaxation frequency, and then it is possible to establish a relationship between the estimated information and the concentration of target molecules for biosensing.

In addition, the relaxation frequency based method requires a sufficient number of data points to obtain the relaxation frequency, which adversely influences the time efficiency of the measurement process. In contrast, our proposed method has the potential for improving the time efficiency of the measurement process by analyzing reduced spectra through changing the coefficient matrix in the matrix equation.

1.6 Reference

[1] S. Lopez-Leon, T. Wegman-Ostrosky, C. Perelman, R. Sepulveda, P.A. Rebolledo, A. Cuapio, S. Villapol, More than 50 long-term effects of COVID-19: a systematic review and meta-analysis, Sci. Rep. 11 (2021) 16144–16144. https://doi.org/10.1038/s41598-021-95565-8.

[2] L. Ma, J. Zhang, H. Chen, J. Zhou, Y. Ding, Y. Liu, An overview on ELISA techniques for FMD, Virol. J. 8 (2011) 419. https://doi.org/10.1186/1743-422X-8-419.

[3] M. Kubista, J.M. Andrade, M. Bengtsson, A. Forootan, J. Jonák, K. Lind, R. Sindelka, R. Sjöback, B. Sjögreen, L. Strömbom, A. Ståhlberg, N. Zoric, The real-time polymerase

chain reaction, Real-Time Polym. Chain React. 27 (2006) 95–125. https://doi.org/10.1016/j.mam.2005.12.007.
[4] J. Ye, G. Coulouris, I. Zaretskaya, I. Cutcutache, S. Rozen, T.L. Madden, Primer-BLAST: A tool to design target-specific primers for polymerase chain reaction, BMC Bioinformatics. 13 (2012) 134. https://doi.org/10.1186/1471-2105-13-134.
[5] H.O. Kaya, A.E. Cetin, M. Azimzadeh, S.N. Topkaya, Pathogen detection with electrochemical biosensors: Advantages, challenges and future perspectives, J. Electroanal. Chem. 882 (2021) 114989–114989. https://doi.org/10.1016/j.jelechem.2021.114989.
[6] H. Chai, W. Cheng, D. Jin, P. Miao, Recent Progress in DNA Hybridization Chain Reaction Strategies for Amplified Biosensing, ACS Appl. Mater. Interfaces. 13 (2021) 38931–38946. https://doi.org/10.1021/acsami.1c09000.
[7] G. Zito, G. Sanità, B. Guilcapi Alulema, S.N. Lara Yépez, V. Lanzio, F. Riminucci, S. Cabrini, M. Moccia, C. Avitabile, A. Lamberti, V. Mocella, I. Rendina, S. Romano, Label-free DNA biosensing by topological light confinement, 10 (2021) 4279–4287. https://doi.org/10.1515/nanoph-2021-0396.
[8] Y. Su, M.C. Hammond, RNA-based fluorescent biosensors for live cell imaging of small molecules and RNAs, Curr. Opin. Biotechnol. 63 (2020) 157–166. https://doi.org/10.1016/j.copbio.2020.01.001.
[9] M. Tian, M. Qiao, C. Shen, F. Meng, L.A. Frank, V.V. Krasitskaya, T. Wang, X. Zhang, R. Song, Y. Li, J. Liu, S. Xu, J. Wang, Highly-sensitive graphene field effect transistor biosensor using PNA and DNA probes for RNA detection, Appl. Surf. Sci. 527 (2020) 146839–146839. https://doi.org/10.1016/j.apsusc.2020.146839.
[10] S. Bian, M. Shang, M. Sawan, Rapid biosensing SARS-CoV-2 antibodies in vaccinated healthy donors, Biosens. Bioelectron. 204 (2022) 114054–114054. https://doi.org/10.1016/j.bios.2022.114054.
[11] S. Sharma, H. Byrne, R.J. O'Kennedy, Antibodies and antibody-derived analytical biosensors, Essays Biochem. 60 (2016) 9–18. https://doi.org/10.1042/EBC20150002.
[12] A. Yakoh, U. Pimpitak, S. Rengpipat, N. Hirankarn, O. Chailapakul, S. Chaiyo, Paper-based electrochemical biosensor for diagnosing COVID-19: Detection of SARS-CoV-2 antibodies and antigen, Biosens. Bioelectron. 176 (2021) 112912–112912. https://doi.org/10.1016/j.bios.2020.112912.
[13] F. Cui, Y. Yue, Y. Zhang, Z. Zhang, H.S. Zhou, Advancing Biosensors with Machine Learning, ACS Sens. 5 (2020) 3346–3364. https://doi.org/10.1021/acssensors.0c01424.
[14] H.S. Magar, R.Y.A. Hassan, A. Mulchandani, Electrochemical impedance spectroscopy (Eis): Principles, construction, and biosensing applications, Sensors. 21 (2021). https://doi.org/10.3390/s21196578.
[15] A. Sanati, M. Jalali, K. Raeissi, F. Karimzadeh, M. Kharaziha, S.S. Mahshid, S. Mahshid, A review on recent advancements in electrochemical biosensing using carbonaceous nanomaterials, Microchim. Acta. 186 (2019) 773–773. https://doi.org/10.1007/s00604-019-3854-2.
[16] A.B. Das, T. Kumari, P.P. Sahu, Calorimetric biosensors: core principles, techniques, fabrication and application, Biosens. Food Saf. Qual. CRC Press. (2022) 11–21.

[17] X. Tian, L.C. Murfin, L. Wu, S.E. Lewis, T.D. James, Fluorescent small organic probes for biosensing, Chem. Sci. 12 (2021) 3406–3426. https://doi.org/10.1039/d0sc06928k.
[18] P. Rees, J.W. Wills, M.R. Brown, C.M. Barnes, H.D. Summers, The origin of heterogeneous nanoparticle uptake by cells, Nat. Commun. 10 (2019) 2341–2341. https://doi.org/10.1038/s41467-019-10112-4.
[19] L. Wang, J. Lin, Recent advances on magnetic nanobead based biosensors: From separation to detection, TrAC Trends Anal. Chem. 128 (2020) 115915–115915. https://doi.org/10.1016/j.trac.2020.115915.
[20] S. Anand, M. Samuel, C.-S. Ang, S. Keerthikumar, S. Mathivanan, Label-Based and Label-Free Strategies for Protein Quantitation, in: S. Keerthikumar, S. Mathivanan (Eds.), Proteome Bioinforma., Springer New York, New York, NY, 2017: pp. 31–43. https://doi.org/10.1007/978-1-4939-6740-7_4.
[21] V.R. Samuel, K.J. Rao, A review on label free biosensors, Biosens. Bioelectron. X. 11 (2022) 100216–100216. https://doi.org/10.1016/j.biosx.2022.100216.
[22] R. Goswami, B. Bhowmick, Comparative Analyses of Circular Gate TFET and Heterojunction TFET for Dielectric-Modulated Label-Free Biosensing, IEEE Sens. J. 19 (2019) 9600–9609. https://doi.org/10.1109/JSEN.2019.2928182.
[23] S. Sang, Y. Wang, Q. Feng, Y. Wei, J. Ji, W. Zhang, Progress of new label-free techniques for biosensors: a review, Crit. Rev. Biotechnol. 36 (2016) 465–481. https://doi.org/10.3109/07388551.2014.991270.
[24] L. He, R. Huang, P. Xiao, Y. Liu, L. Jin, H. Liu, S. Li, Y. Deng, Z. Chen, Z. Li, N. He, Current signal amplification strategies in aptamer-based electrochemical biosensor: A review, Chin. Chem. Lett. 32 (2021) 1593–1602. https://doi.org/10.1016/j.cclet.2020.12.054.
[25] V. Harish, D. Tewari, M. Gaur, A.B. Yadav, S. Swaroop, M. Bechelany, A. Barhoum, Review on Nanoparticles and Nanostructured Materials: Bioimaging, Biosensing, Drug Delivery, Tissue Engineering, Antimicrobial, and Agro-Food Applications, Nanomaterials. 12 (2022) 457–457. https://doi.org/10.3390/nano12030457.
[26] P. Si, N. Razmi, O. Nur, S. Solanki, C.M. Pandey, R.K. Gupta, B.D. Malhotra, M. Willander, A. De La Zerda, Gold nanomaterials for optical biosensing and bioimaging, Nanoscale Adv. 3 (2021) 2679–2698. https://doi.org/10.1039/d0na00961j.
[27] L. Zheng, G. Cai, S. Wang, M. Liao, Y. Li, J. Lin, A microfluidic colorimetric biosensor for rapid detection of Escherichia coli O157:H7 using gold nanoparticle aggregation and smart phone imaging, Biosens. Bioelectron. 124–125 (2019) 143–149. https://doi.org/10.1016/j.bios.2018.10.006.
[28] Y.-C. Ou, X. Wen, C.A. Johnson, D. Shae, O.D. Ayala, J.A. Webb, E.C. Lin, R.C. DeLapp, K.L. Boyd, A. Richmond, A. Mahadevan-Jansen, M. Rafat, J.T. Wilson, J.M. Balko, M.N. Tantawy, A.E. Vilgelm, R. Bardhan, Multimodal Multiplexed Immunoimaging with Nanostars to Detect Multiple Immunomarkers and Monitor Response to Immunotherapies, ACS Nano. 14 (2020) 651–663. https://doi.org/10.1021/acsnano.9b07326.
[29] N. Elahi, M. Kamali, M.H. Baghersad, B. Amini, A fluorescence Nano-biosensors immobilization on Iron (MNPs) and gold (AuNPs) nanoparticles for detection of Shigella

spp, Mater. Sci. Eng. C. 105 (2019) 110113–110113. https://doi.org/10.1016/j.msec.2019.110113.
[30] C. Wyatt Shields Iv, C.D. Reyes, G.P. López, Microfluidic cell sorting: A review of the advances in the separation of cells from debulking to rare cell isolation, Lab. Chip. 15 (2015) 1230–1249. https://doi.org/10.1039/c4lc01246a.
[31] C. Billings, M. Langley, G. Warrington, F. Mashali, J.A. Johnson, Magnetic particle imaging: Current and future applications, magnetic nanoparticle synthesis methods and safety measures, Int. J. Mol. Sci. 22 (2021). https://doi.org/10.3390/ijms22147651.
[32] F. Qiu, X. Gan, B. Jiang, R. Yuan, Y. Xiang, Electrode immobilization-free and sensitive electrochemical sensing of thrombin via magnetic nanoparticle-decorated DNA polymers, Sens. Actuators B Chem. 331 (2021) 129395–129395. https://doi.org/10.1016/j.snb.2020.129395.
[33] J. Llandro, J.J. Palfreyman, A. Ionescu, C.H.W. Barnes, Magnetic biosensor technologies for medical applications: a review, Med. Biol. Eng. Comput. 48 (2010) 977–998. https://doi.org/10.1007/s11517-010-0649-3.
[34] N.M. Elkassabany, G.M. Meny, R.R. Doria, C. Marcucci, Green Plasma—Revisited, Anesthesiology. 108 (2008) 764–765. https://doi.org/10.1097/ALN.0b013e3181672668.
[35] C. Ren, Q. Bayin, S. Feng, Y. Fu, X. Ma, J. Guo, Biomarkers detection with magnetoresistance-based sensors, Biosens. Bioelectron. 165 (2020) 112340–112340. https://doi.org/10.1016/j.bios.2020.112340.
[36] D. Su, K. Wu, R. Saha, C. Peng, J.P. Wang, Advances in magnetoresistive biosensors, Micromachines. 11 (2020). https://doi.org/10.3390/mi11010034.
[37] N. Li, T. Tang, J. Li, L. Luo, C. Li, J. Shen, J. Yao, Highly sensitive biosensor with graphene-MoS2 heterostructure based on photonic spin Hall effect, J. Magn. Magn. Mater. 484 (2019) 445–450. https://doi.org/10.1016/j.jmmm.2019.04.003.
[38] Y. Yang, T. Lee, M. Kim, C. Jung, T. Badloe, D. Lee, S. Lee, H.-J. Lee, J. Rho, Dynamic Optical Spin Hall Effect in Chitosan-Coated All-Dielectric Metamaterials for a Biosensing Platform, IEEE J. Sel. Top. Quantum Electron. 27 (2021) 1–8. https://doi.org/10.1109/JSTQE.2021.3065826.
[39] S. Huber, C. Min, C. Staat, J. Oh, C.M. Castro, A. Haase, R. Weissleder, B. Gleich, H. Lee, Multichannel digital heteronuclear magnetic resonance biosensor, Biosens. Bioelectron. 126 (2019) 240–248. https://doi.org/10.1016/j.bios.2018.10.052.
[40] P. Khramtsov, I. Barkina, M. Kropaneva, M. Bochkova, V. Timganova, A. Nechaev, I. Byzov, S. Zamorina, A. Yermakov, M. Rayev, Magnetic nanoclusters coated with albumin, casein, and gelatin: Size tuning, relaxivity, stability, protein corona, and application in nuclear magnetic resonance immunoassay, Nanomaterials. 9 (2019). https://doi.org/10.3390/nano9091345.
[41] A. Fornara, P. Johansson, K. Petersson, S. Gustafsson, Q. Jian, E. Olsson, D. Iiver, A. Krozer, M. Muhammed, C. Johansson, Tailored magnetic nanoparticles for direct and sensitive detection of biomolecules in biological samples, Nano Lett. 8 (2008) 3423–3428. https://doi.org/10.1021/nl8022498.
[42] T.Z.G. de la Torre, A. Mezger, D. Herthnek, C. Johansson, P. Svedlindh, M. Nilsson, M. Strømme, Detection of rolling circle amplified DNA molecules using probe-tagged magnetic nanobeads in a portable AC susceptometer, Biosens. Bioelectron. 29 (2011) 195–199. https://doi.org/10.1016/j.bios.2011.08.019.

[43] J.B. Haun, T.J. Yoon, H. Lee, R. Weissleder, Magnetic nanoparticle biosensors, Wiley Interdiscip. Rev. Nanomed. Nanobiotechnol. 2 (2010) 291–304. https://doi.org/10.1002/wnan.84.
[44] A. Prieto Astalan, C. Jonasson, K. Petersson, J. Blomgren, D. Ilver, A. Krozer, C. Johansson, Magnetic response of thermally blocked magnetic nanoparticles in a pulsed magnetic field, Proc. Sixth Int. Conf. Sci. Clin. Appl. Magn. Carr. 311 (2007) 166–170. https://doi.org/10.1016/j.jmmm.2006.10.1182.
[45] J. Connolly, T.G. St Pierre, Proposed biosensors based on time-dependent properties of magnetic fluids, J. Magn. Magn. Mater. 225 (2001) 156–160. https://doi.org/10.1016/S0304-8853(00)01245-2.
[46] S.-H. Chung, A. Hoffmann, K. Guslienko, S.D. Bader, C. Liu, B. Kay, L. Makowski, L. Chen, Biological sensing with magnetic nanoparticles using Brownian relaxation (invited), J. Appl. Phys. 97 (2005) 10R101-10R101. https://doi.org/10.1063/1.1853694.
[47] S.H. Chung, A. Hoffmann, S.D. Bader, C. Liu, B. Kay, L. Makowski, L. Chen, Biological sensors based on Brownian relaxation of magnetic nanoparticles, Appl. Phys. Lett. 85 (2004) 2971–2973. https://doi.org/10.1063/1.1801687.
[48] K. Wu, J. Liu, D. Su, R. Saha, J.-P. Wang, Magnetic Nanoparticle Relaxation Dynamics-Based Magnetic Particle Spectroscopy for Rapid and Wash-Free Molecular Sensing, ACS Appl. Mater. Interfaces. 11 (2019) 22979–22986. https://doi.org/10.1021/acsami.9b05233.
[49] K. Park, T. Harrah, E.B. Goldberg, R.P. Guertin, S. Sonkusale, Multiplexed sensing based on Brownian relaxation of magnetic nanoparticles using a compact AC susceptometer, Nanotechnology. 22 (2011). https://doi.org/10.1088/0957-4484/22/8/085501.
[50] J. Zhong, K.-J. Janssen, S. Draack, T. Viereck, M. Schilling, F. Ludwig, Dependence of biomolecule detection on magnetic nanoparticle concentration, J. Magn. Magn. Mater. 517 (2021) 167408–167408. https://doi.org/10.1016/j.jmmm.2020.167408.
[51] K. Wu, V.K. Chugh, A. di Girolamo, J. Liu, R. Saha, D. Su, V.D. Krishna, A. Nair, W. Davies, Y.A. Wang, M.C.-J. Cheeran, J.-P. Wang, A Portable Magnetic Particle Spectrometer for Future Rapid and Wash-Free Bioassays, ACS Appl. Mater. Interfaces. 13 (2021) 7966–7976. https://doi.org/10.1021/acsami.0c21040.
[52] S.P. Yeap, J. Lim, H.P. Ngang, B.S. Ooi, A.L. Ahmad, Role of particle–particle interaction towards effective interpretation of Z-average and particle size distributions from dynamic light scattering (DLS) analysis, J. Nanosci. Nanotechnol. 18 (2018) 6957–6964.
[53] P. Bender, C. Balceris, F. Ludwig, O. Posth, L.K. Bogart, W. Szczerba, A. Castro, L. Nilsson, R. Costo, H. Gavilán, D. González-Alonso, I.D. Pedro, L.F. Barquin, C. Johansson, Distribution functions of magnetic nanoparticles determined by a numerical inversion method, New J. Phys. 19 (2017). https://doi.org/10.1088/1367-2630/aa73b4.
[54] A.O. Ivanov, P.J. Camp, Theory of the dynamic magnetic susceptibility of ferrofluids, Phys. Rev. E. 98 (2018) 50602–50602. https://doi.org/10.1103/PhysRevE.98.050602.

2 Theoretical background and methodology

A method for estimating the distributions of MNP clusters from AC magnetization spectra is one of the essential concepts of this study. This chapter discusses the theoretical background of AC magnetization spectra derived from suspensions of MNP clusters. The theoretical background includes relaxation behaviors of suspensions of MNPs, and the relationship between relaxation behaviors and magnetic response of suspensions of MNPs. To overcome the issue mentioned in the Chapter 1, a method for estimating the distributions of MNP clusters by solving an inverse problem is proposed. In magnetic susceptometry based biosensing, whether the interaction between MNPs can be ignored or not significantly changes the magnetic response of MNPs. Hence, this chapter also discusses how to form the matrix equation of the proposed method in two situations where the dipole-dipole interaction among MNPs can be ignored or cannot be ignored.

2.1 AC magnetization spectra of MNP suspensions

As mentioned in **Section** 1.2, AC magnetization spectra corresponds to relaxation behavior of MNPs dispersed in suspensions. Thus, before discussing about the AC magnetization spectra, it is important to explain relaxation behavior of MNPs at first. For MNPs dispersed in suspensions, relaxation mechanisms of them are generally classified as Neel (moment) relaxation and Brownian (physical rotation) relaxation. The Neel relaxation time depends on the primary size d_c and the magneto crystalline anisotropy K_U of MNPs and is given by [1]:

$$\tau_N = \tau_0 \exp\left(\frac{\pi K_U d_c^3}{6K_B T}\right); 10^{-10}s \leq \tau_0 \leq 10^{-10}s, \qquad (2-1)$$

where K_B and T represent temperature, and Boltzmann constant, respectively. Meanwhile, The Brownian relaxation time depends on the hydrodynamic diameter d_h of the MNPs, and is given by [2]:

$$\tau_B = \frac{\eta \pi d_h^3}{2K_B T} \qquad (2-2)$$

where η represents viscosity of the medium. The effective relaxation of MNPs is considered as the contributions of both relaxation mechanisms. However, the contribution of Neel relaxation in the magnetization can be ignored until the frequency until about 10^5 Hz [3]. In addition, increase in the hydrodynamic diameter of functionalized MNPs caused by the formation of clusters among MNPs and biomolecules during biosensing mainly changes the Brownian relaxation time as a whole more than the Neel relaxation time. Thus, in this thesis, we focus on the Brownian relaxation behavior since we focus on biosensing applications in the low frequency range (~10 kHz) where Brownian relaxation is generally considered as dominant.

For The magnetic response of MNPs suspension to a small AC magnetic field [4] with angular frequency $\omega = 2\pi f$ can be considered as a linear response and expressed by an AC magnetization spectrum $\boldsymbol{M}$ (AC susceptibility spectrum χ is generally used. However, in the linear response region with an external magnetic field H, $\boldsymbol{\chi} = \boldsymbol{M}/H$, in other words, the shape of the spectrum of AC susceptibility and AC magnetization is same. In this thesis, we use AC magnetization spectra for further analysis). The AC magnetization spectrum $\boldsymbol{M}$ includes two components, which are the real part $\boldsymbol{M}'$ corresponding to in-phase response and the imaginary part $\boldsymbol{M}''$ corresponding to out of phase response. The relationship between $\boldsymbol{M}$, $\boldsymbol{M}'$ and $\boldsymbol{M}''$ is given by $\boldsymbol{M} = \boldsymbol{M}' - \mathrm{i}\boldsymbol{M}''$. As mentioned in **Section** 1.2, in practice situations,

various types of MNP clusters coexists in suspensions, resulting the relaxation time of suspended MNP clusters are polydisperse. When relaxation time of suspended MNP clusters polydisperse without interaction among MNP clusters, the real part M' and imaginary part *M"* of the AC magnetization spectrum are given by:

$$M'(\omega) = \sum_{i=1}^{K} p(d_{h,i}) M'(\omega, d_{h,i})\, \Delta d_h, \qquad (2-3)$$

$$M''(\omega) = \sum_{i=1}^{K} p(d_{h,i}) M''(\omega, d_{h,i})\, \Delta d_h, \qquad (2-4)$$

where $p(d_{h,i})$, $M'(\omega,\ d_{h,i})$, $M''(\omega,\ d_{h,i})$ are the probability density function of MNP clusters with hydrodynamic size $d_{h,i}$ the real part of magnetization of MNPs with hydrodynamic size $d_{h,i}$ and the imaginary part of magnetization of MNPs with hydrodynamic size $d_{h,i}$, respectively. As discussed in the previous study [5], when suspended MNPs follow Debye relaxation model (no dipole-dipole interaction among MNPs) and Brownian relaxation is dominant, $M''(\omega, d_{h,i})$, $M''(\omega, d_{h,i})$ and relaxation time are given by:

$$M'(\omega, d_{h,i}) = M_0 \frac{1}{1 + \left(\omega\tau(d_{h,i})\right)^2}, \qquad (2-5)$$

$$M''(\omega, d_{h,i}) = M_0 \frac{\omega\tau(d_{h,i})}{1 + \left(\omega\tau(d_{h,i})\right)^2}, \qquad (2-6)$$

$$\tau(d_{h,i}) = \tau_B(d_{h,i}) = \frac{\pi\eta d_{h,i}^3}{2k_B T}, \qquad (2-7)$$

where $d_{h,i}$ is the hydrodynamic particle diameter and M_0 is the static magnetization. M_0 is given by:

$$M_0 = H\frac{\mu_0 n m^2}{3k_B T}, \qquad (2-8)$$

with vacuum permeability μ_0, number density of MNP clusters $n = \frac{N}{V}$ (where N is the number of MNPs with primary size, and V is the volume of the medium), magnetic moment $m=M_s V_c$ (where M_s is the saturation magnetization and V_c is the mean primary volume of MNPs), and external magnetic field H. Generally, the number of MNPs with primary size N is equal to $\frac{m_{total}}{\rho V_c}$, where m_{total} is the total mass of MNPs in suspension, and ρ is the density of MNPs. Then the static magnetization M_0 is rewritten by,

$$M_0 = H\frac{\mu_0 m_{total} V_c (M_s)^2}{3k_B T V \rho}. \qquad (2-9)$$

From eq (2-9), the static magnetization is proportional to the mass concentration of MNPs in suspension.

2.2 Estimation of distribution of MNP clusters following Debye relaxation model

To estimate the distribution of MNP clusters following Debye relaxation model, it is proper to rewrite the eq (2-5) and eq (2-6) to a matrix equation to simplify further computation. When the number of sampling points of angular frequency ω is N_s, the matrix equation is given as follows:

$$\boldsymbol{Ax} = \boldsymbol{y}, \qquad (2-10)$$

$$\boldsymbol{A} = \begin{pmatrix} \boldsymbol{A}_r \\ \boldsymbol{A}_i \end{pmatrix}, \qquad (2-11)$$

$$\boldsymbol{A}_r = \begin{pmatrix} \frac{1}{1+(\omega_1\tau(d_{h,1}))^2} & \cdots & \frac{1}{1+(\omega_1\tau(d_{h,K}))^2} \\ \vdots & \ddots & \vdots \\ \frac{1}{1+(\omega_{Ns}\tau(d_{h,1}))^2} & \cdots & \frac{1}{1+(\omega_{Ns}\tau(d_{h,K}))^2} \end{pmatrix}, \quad (2-12)$$

$$\boldsymbol{A}_i = \begin{pmatrix} \frac{\omega_1\tau(d_{h,1})}{1+(\omega_1\tau(d_{h,1}))^2} & \cdots & \frac{\omega_1\tau(d_{h,K})}{1+(\omega_1\tau(d_{h,K}))^2} \\ \vdots & \ddots & \vdots \\ \frac{\omega_{Ns}\tau(d_{h,1})}{1+(\omega_{Ns}\tau(d_{h,1}))^2} & \cdots & \frac{\omega_{Ns}\tau(d_{h,K})}{1+(\omega_{Ns}\tau(d_{h,K}))^2} \end{pmatrix}, \quad (2-13)$$

$$\boldsymbol{x} = \left(M_0 p(d_{h,1})\Delta d_h, \cdots, M_0 p(d_{h,K})\Delta d_h\right)^T, \quad (2-14)$$

$$\boldsymbol{y} = \begin{pmatrix} \boldsymbol{y}_r \\ \boldsymbol{y}_i \end{pmatrix}, \quad (2-15)$$

$$\boldsymbol{y}_r = \left(M'^{(\omega_1)}, \cdots, M'^{(\omega_{Ns})}\right)^T, \quad (2-16)$$

$$\boldsymbol{y}_i = \left(M''^{(\omega_1)}, \cdots, M''^{(\omega_{Ns})}\right)^T, \quad (2-17)$$

The $2N_s \times K$ matrix $\boldsymbol{A}$ is the coefficient matrix formed by the real part $\boldsymbol{A}_\mathrm{r}$ and the imaginary part $\boldsymbol{A}_\mathrm{i}$ of AC magnetization spectra with various angular frequency and hydrodynamic size of MNP clusters. $K \times 1$ vector $\boldsymbol{x}$ represents the distribution of MNP clusters. $2N_s \times 1$ vector $\boldsymbol{y}$ includes the real part $\boldsymbol{y}_r$ and imaginary part $\boldsymbol{y}_i$ of AC magnetization spectra.

To estimate hydrodynamic size distribution of MNP clusters $\boldsymbol{x}$ from $\boldsymbol{A}$ and $\boldsymbol{y}$, the following ridge regression [6] is used:

$$\underset{\boldsymbol{x}}{\operatorname{argmin}} \left|\left|\boldsymbol{A}\boldsymbol{x} - \boldsymbol{y}\right|\right|^2 + \lambda \left|\left|\boldsymbol{x}\right|\right|^2, \quad (2-18)$$

where $||\cdot||$ is the standard Euclidean vector norm and λ is the regularization parameter. The numerical solution of $\boldsymbol{x}$ in eq (2-18) is obtained with a given λ by eq (2-19),

$$\hat{\boldsymbol{x}} = (\boldsymbol{A}^T\boldsymbol{A} + \lambda\boldsymbol{I})^{-1}\boldsymbol{A}^T\boldsymbol{y}. \quad (2-19)$$

After $\hat{\boldsymbol{x}}$ was estimated, the ratio of cluster with hydrodynamic size $d_{h,i}$ was calculated by eq (2-20) as follows:

$$r_{d_{h,i}} = \frac{|x_i|}{\sum_{i=1}^{K}|x_i|}, \qquad (2-20)$$

where $|\cdot|$ is the absolute value of given number, $r_{d_{h,i}}$ is the ratio of cluster with hydrodynamic size $d_{h,i}$ and x_i is the ith element of $\hat{\boldsymbol{x}}$.

Moreover, from eq (2-14), the static magnetization M_0 is also included in the estimated $\hat{\boldsymbol{x}}$, resulting that $\sum_{i=1}^{K}|x_i|$ is proportional to the mass concentration of MNPs in suspension.

Generally, relaxation frequency corresponding to the effective hydrodynamic size of MNP clusters is obtained from the imaginary part of AC magnetization spectra. The matrix equation for estimating the distribution of MNP clusters is given by:

$$\boldsymbol{A}_i\boldsymbol{x} = \boldsymbol{y_i}, \qquad (2-21)$$

$$\hat{\boldsymbol{x}} = (\boldsymbol{A}_i{}^T\boldsymbol{A}_i + \lambda\boldsymbol{I})^{-1}\boldsymbol{A}_i{}^T\boldsymbol{y_i}, \qquad (2-22)$$

where $\boldsymbol{A}_i$,and $\boldsymbol{y_i}$ are given in eq (2-13) and eq (2-17). By using eq (2-22), the distribution of MNP clusters is estimated by only using the imaginary part of AC magnetization spectra.

2.3 Estimation of distribution of MNPs with interactions among MNPs

In practical situations, MNPs aggregate via biomolecules, resulting in that the dipole-dipole interaction among MNPs could not be ignored. Debye model does not accurately describe the AC magnetization spectra of MNPs, particularly when there are dipole-dipole interactions existing between MNPs [7]. Thus, estimation from eq (2-19) based on Debye relaxation model is incorrect. To estimate the distribution of MNP clusters more accurately, a more accurate model is necessary. However, the model for multi-core MNP clusters with

the dipole-dipole interaction exists is complicated, and there is still no accurate model. Thus, an alternate model is necessary. Here, we propose a method using experimental AC magnetization spectra data of MNP clusters as column vector to form coefficient matrix in eq (2-10). The assumption of this method is that we ignore the interaction among clusters as shown in Fig 2-1. The reason that we use experimental AC magnetization spectra data is because the interaction between MNPs has been included in the experimental data. The $N_s \times K$ matrix formed by the experimental data is denoted as $\boldsymbol{A}_{\mathbf{exp}}$ and given as follows:

$$\boldsymbol{A}_{\boldsymbol{exp}} = \begin{pmatrix} \boldsymbol{A}_{\boldsymbol{exp,r}} \\ \boldsymbol{A}_{\boldsymbol{exp,i}} \end{pmatrix}, \tag{2-23}$$

$$\boldsymbol{A}_{\boldsymbol{exp,r}} = \begin{pmatrix} M_{\mathrm{exp,r}}(d_{h,1}, \omega_1) & \cdots & M_{\mathrm{exp,r}}(d_{h,K}, \omega_1) \\ \vdots & \ddots & \vdots \\ M_{\mathrm{exp,r}}(d_{h,1}, \omega_{Ns}) & \cdots & M_{\mathrm{exp,r}}(d_{h,K}, \omega_{Ns}) \end{pmatrix}, \tag{2-24}$$

$$\boldsymbol{A}_{\boldsymbol{exp,i}} = \begin{pmatrix} M_{\mathrm{exp,i}}(d_{h,1}, \omega_1) & \cdots & M_{\mathrm{exp,i}}(d_{h,K}, \omega_1) \\ \vdots & \ddots & \vdots \\ M_{\mathrm{exp,i}}(d_{h,1}, \omega_{Ns}) & \cdots & M_{\mathrm{exp,i}}(d_{h,K}, \omega_{Ns}) \end{pmatrix}, \tag{2-25}$$

where $M_{\mathrm{exp,r}}(d_{h,1}, \omega_j)$ and $M_{\mathrm{exp,i}}(d_{h,1}, \omega_j)$ are the real part and imaginary part of measured AC magnetization spectra data sample from MNPs with cluster size $d_{h,k}$ at ω_j, respectively. The meaning of vector $\boldsymbol{x}$ becomes mass ratio vector of MNPs with cluster size $d_{h,k}$, by assuming static magnetization is proportional to mass of MNP clusters. The $\boldsymbol{x}$ corresponding to $\boldsymbol{A}_{\boldsymbol{exp}}$ is renamed as $\boldsymbol{x}_{\boldsymbol{exp}}$ and given as follows:

$$\boldsymbol{x}_{\boldsymbol{exp}} = \left(c_{d_{h,1}}, \cdots, c_{d_{h,K}}\right)^T, \tag{2-26}$$

where $c_{d_{h,i}}$ is the mass ratio of MNPs cluster with size $d_{h,i}$. Similarly, the numerical solution of $\boldsymbol{x}_{\boldsymbol{exp}}$ is obtained by using eq (2-19) with $\boldsymbol{A}_{\boldsymbol{exp}}$ and $\boldsymbol{y}$. the estimated mass ratio vector of

MNPs is calculated by substituting $\hat{\boldsymbol{x}}_{\boldsymbol{exp}}$ into eq (2-20) to obtain $c_{d_{h,i}}$. After $c_{d_{h,i}}$ is obtained, the number of the MNPs cluster with hydrodynamic size $d_{h,i}$ can be calculated by eq (2-27),

$$n_{d_{h,i}} = \frac{c_{d_{h,i}} \mathrm{m}_{total}}{\rho_{Fe_3O_4} \frac{4}{3}\pi \left(\frac{d_{h,i}}{2}\right)^3}, \qquad (2-27)$$

where $n_{d_{h,i}}$ is the number of the MNPs cluster with hydrodynamic size $d_{h,i}$, m_{total} is the total mass of MNPs in the suspension, and $\rho_{Fe_3O_4}$ is the density of Fe_3O_4.

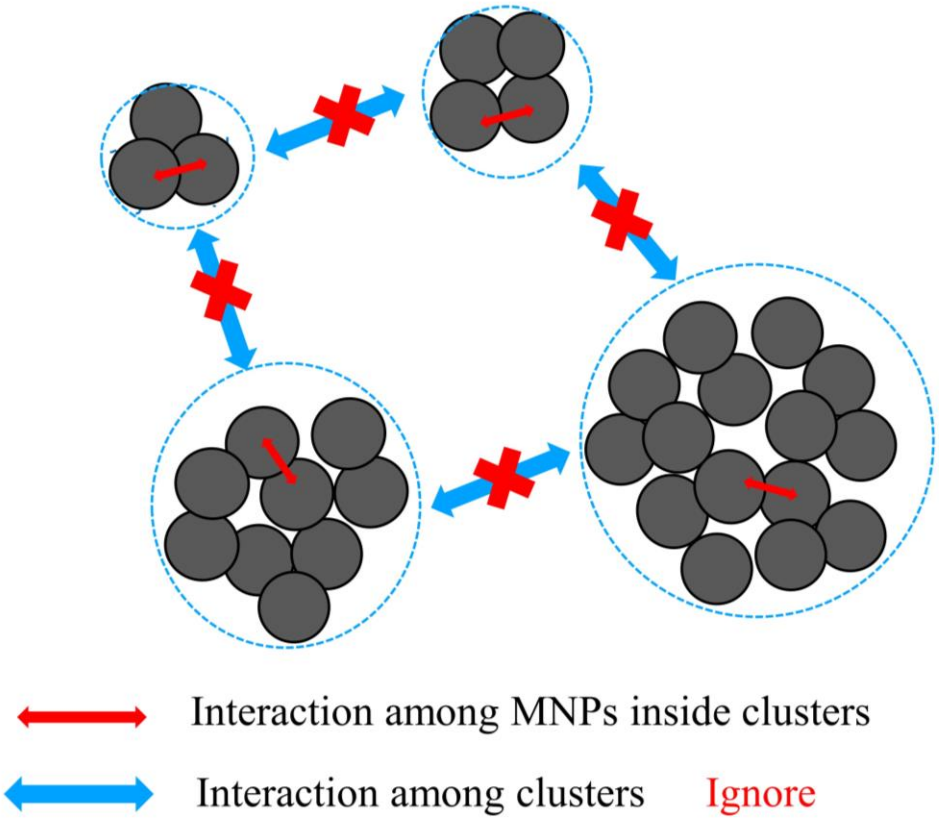

FIG. 2-1. Assumption of interactions used in the experimental model.

2.4 Summary

The method for estimating the distribution of MNP clusters from AC magnetization spectra was proposed, when MNPs follow the Debye relaxation model. In addition, the method for estimating the mass concentration of MNPs was proposed. Because it is necessary to consider the dipole-dipole interaction among MNPs in some practical situations, especially when MNPs aggregate via biomolecules. We discussed the alternative method to form the matrix equation when the interaction among MNPs inside the clusters cannot be negligible rather than using the Debye relaxation model.

2.5 Reference

[1] P C Fannin, S W Charles, On the calculation of the Neel relaxation time in uniaxial single-domain ferromagnetic particles, J. Phys. Appl. Phys. 27 (1994) 185–185. https://doi.org/10.1088/0022-3727/27/2/001.

[2] J. Dieckhoff, D. Eberbeck, M. Schilling, F. Ludwig, Magnetic-field dependence of Brownian and Néel relaxation times, J. Appl. Phys. 119 (2016) 043903–043903. https://doi.org/10.1063/1.4940724.

[3] S. Ota, Y. Takemura, Characterization of Néel and Brownian Relaxations Isolated from Complex Dynamics Influenced by Dipole Interactions in Magnetic Nanoparticles, J. Phys. Chem. C. 123 (2019) 28859–28866. https://doi.org/10.1021/acs.jpcc.9b06790.

[4] K. Enpuku, T. Tanaka, Y. Tamai, F. Dang, N. Enomoto, J. Hojo, H. Kanzaki, N. Usuki, Size Distribution of Magnetic Marker Estimated from AC Susceptibility in Solution for Biosensor Application, Jpn. J. Appl. Phys. 47 (2008) 7859–7859. https://doi.org/10.1143/JJAP.47.7859.

[5] F. Ludwig, C. Balceris, C. Jonasson, C. Johansson, Analysis of AC Susceptibility Spectra for the Characterization of Magnetic Nanoparticles, IEEE Trans. Magn. 53 (2017). https://doi.org/10.1109/TMAG.2017.2693420.

[6] T. Hastie, R. Tibshirani, J.H. Friedman, J.H. Friedman, The elements of statistical learning: data mining, inference, and prediction, Springer, 2009.

[7] Z. Du, Y. Cui, Y. Sun, H. Zhang, S. Bai, T. Yoshida, Empirical Expression of AC Susceptibility of Magnetic Nanoparticles and Potential Application in Biosensing, IEEE Trans. Nanobioscience. 21 (2022) 496–501. https://doi.org/10.1109/TNB.2021.3126905.

3 Analysis of simulation data

Simulation is a power tool for studies of AC magnetization spectra of MNP clusters with given distributions. In this chapter, AC magnetization spectra of MNPs are simulated via numerical calculations based on **Section** 2.2. Then the proposed method is applied onto the simulated AC magnetization spectra to confirm the feasibility of the proposed method. This chapter also compares the results of distributions of MNPs estimated from the whole (both the real and imaginary part) and the imaginary part of AC magnetization spectra. In practice, the mass concentration of MNPs is also an important factor. We also discuss the relationship between estimated results and the mass concentration of MNPs.

3.1 Method of numerical simulations

To numerically simulate the AC magnetization spectra of MNP clusters based on **Section** 2.2, the distributions of MNP clusters is necessary. Generally, the lognormal distribution was used for describing the distribution of MNPs clusters [1], which is given by:

$$f(d_h) = \frac{1}{\sqrt{2\pi} d_h \sigma_h} exp\left[-\frac{(\ln(d_h)-\mu_h)^2}{2{\sigma_h}^2}\right], \qquad (3-1)$$

where d_h , μ_h and σ_h are the hydrodynamic diameter of MNP clusters, the mean hydrodynamic diameter of MNP clusters and the standard deviation of the natural logarithm of the hydrodynamic diameter, respectively. MNP clusters may follow multimodal distributions in practical situations. To obtain multimodal distributions, multi-types of distributions were mixed as follows:

$$f_{multimodal}(d_h) = \sum_{i=1}^{N} a_i f_i(d_h)\,;\ \sum a_i = 1, \qquad (3-2)$$

where a_i and $f_i(d_h)$ are the mixing parameters and the i-th mixing probability distribution with $\mu_{h,i}$ and $\sigma_{h,i}$ using eq (3-1). Distributions of MNP clusters were generated based on eq (3-1) with μ_h ranging from 3.5 to 6 and σ_h ranging 0.2 from 0.6, which means that the generated mean hydrodynamic size of MNPs ranges from 33.78 nm to 482.99 nm calculated by the mean value of lognormal distribution given by exp $(\mu + \frac{\sigma^2}{2})$ [2]. AC magnetization spectra of MNP clusters were calculated based on generated distributions of MNP clusters via eq (2-10) with the static magnetization M_0 = 1. By the above method, AC magnetization spectra are generated. For instance, the generated distribution of MNP clusters as shown in Fig.3-1(a) was generated and used for calculating AC magnetization spectra as shown in Fig. 3-1(b).

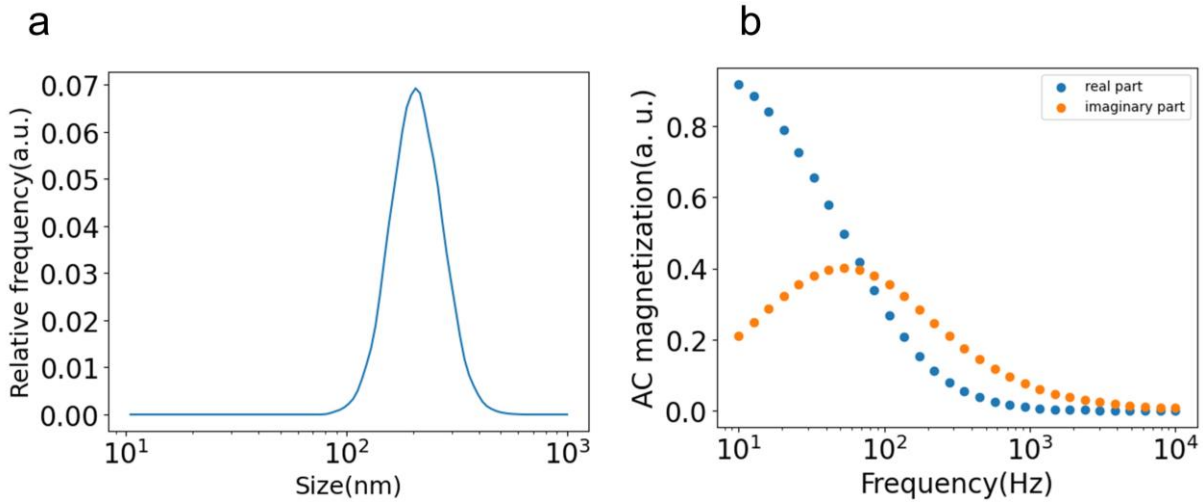

FIG. 3-1. The example of (a) the generated distribution of MNP clusters (monomodal distribution) and (b) generated AC magnetization spectra.

3.2 Results of distributions of MNP clusters from simulation data

To use eq (2-19) and (2-20) to estimate the distributions of MNP clusters from AC magnetization spectra generated via method described in **Section** 3.1, it is necessary to determine a regularization parameter λ. The AC magnetization spectra shown in Fig. 3-1(b) with monomodal distribution of MNP clusters was used to investigate the effect of λ on the R^2 score between the true distribution (used for calculating AC magnetization) and the estimated distribution. The value of λ was varied from 10^{-20} to 2 and the results of the R^2 score are shown in Fig. 3-2(a). From the results, there was no significant change in the R^2 score in a wide range (from 10^{-20} to 10^{-1}) and the value of the R^2 score decreases significantly from about $\lambda>0.1$. Based on Fig. 3-2(a), we selected λ equal to 10^{-4} for further estimation in this section. The distribution of MNP clusters estimated from AC magnetization spectra is shown in Fig. 3-1(b), and the comparison of the estimated distribution and the true distribution is shown in Fig. 3-2(b). From the results, the distribution of MNP clusters was estimated well with a high R^2 score.

In practical biosensing situations, the distribution of MNP clusters is not only monomodal, but could also be bimodal and multimodal [3]. Here, distributions of MNP clusters were generated and used for calculating AC magnetization spectra via eq (2-10) with static magnetization $M_0 = 1$. Then eq (2-19) and eq (2-20) were used to estimate the distribution of MNP clusters. The results of estimation are shown in Fig 3-3. From the results, distributions of MNP clusters were estimated with a high R^2 score even if true distributions are multimodal.

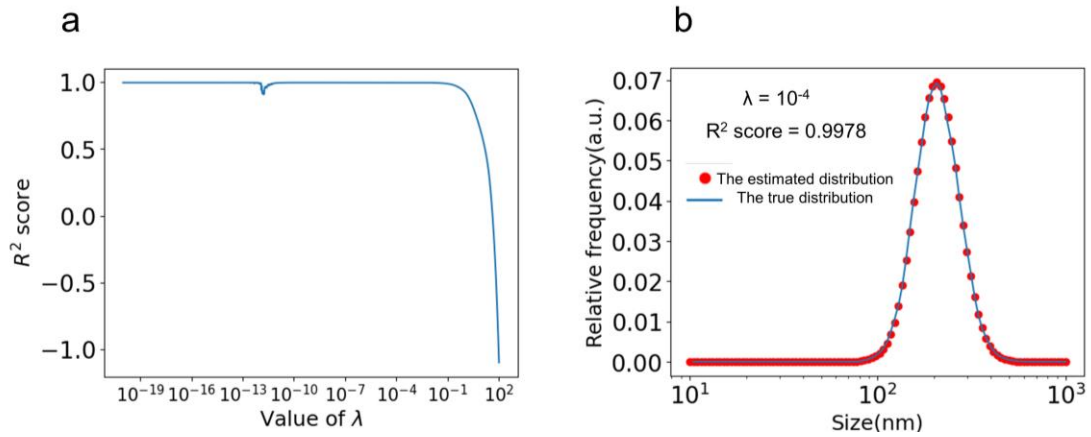

FIG. 3-2. (a) The relationship between the R^2 score and the value of λ. The R^2 score was calculated between the true distribution (used for calculating AC magnetization) and the estimated distribution (the R^2 score reaches the maximum value with λ equal to around 10^{-13}) (b) Comparison between the true distribution and the estimated distribution with λ equal to 10^{-4}.

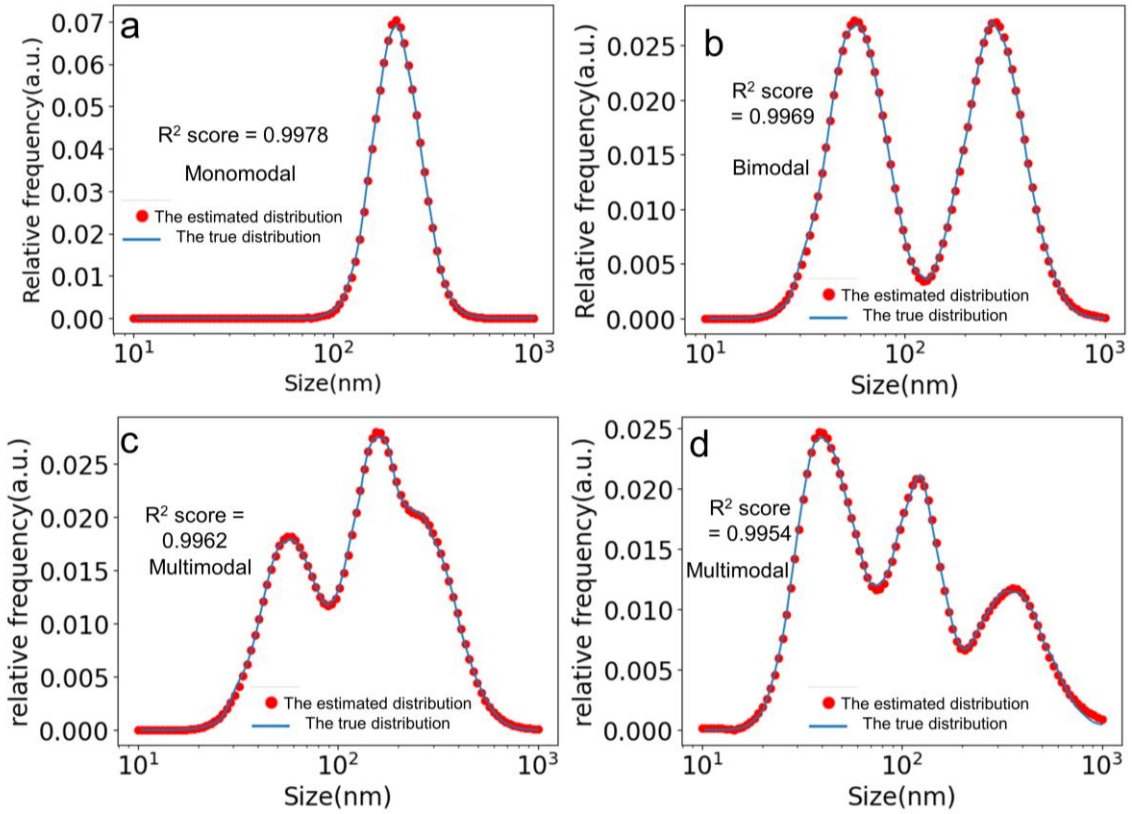

FIG. 3-3. Estimated distributions (λ is equal to 10^{-4}) of MNP clusters from AC magnetization spectra calculated from MNP clusters with (a) monomodal distribution (b) Bimodal distribution λ = 1 (c) and (d) Multimodal distributions.

3.3 Results of mass concentrations of MNP clusters from simulation data

To confirm the feasibility of the proposed method for estimating the mass concentrations of MNP clusters, we used the generated distribution of MNPs shown in Fig 3-4(a) with various values of the static magnetization M_0. For example, the real parts and imaginary parts shown in Fig. 3-4 (b) and (c) were calculated with M_0 equal to 1.0, 0.5 and 0.25 (1.0x concentration, 0.5x concentration and 0.25x concentration represent M_0 equal to 1.0, 0.5 and 0.25, respectively).

At first, eq (2-19) with λ equal to 10^{-4} and eq (2-20) were applied onto calculated AC magnetization spectra to estimate the distributions of MNP clusters, and the results are shown in Fig. 3-5(a). The distributions of MNP clusters estimated from AC magnetization spectra with various concentrations overlapped with each other, indicate the estimated distribution consists with each other well. As mentioned in **Section** 2.2, estimated vector $\hat{\boldsymbol{x}}$ in eq (2-19) has a coefficient M_0 corresponding to the mass concentration of MNP clusters. Here, we assumed that the sum of the absolute value of element in estimated vector $\hat{\boldsymbol{x}}$ proportional to the relative mass concentration of MNP clusters. To confirm our assumption, we plot the relative mass concentration to the sum of the absolute value of element in estimated vector $\hat{\boldsymbol{x}}$ in Fig. 3-5(b). From the results, the sum of the absolute value of element in estimated vector $\hat{\boldsymbol{x}}$ highly corresponds to the relative mass concentration, indicating our assumption is correct.

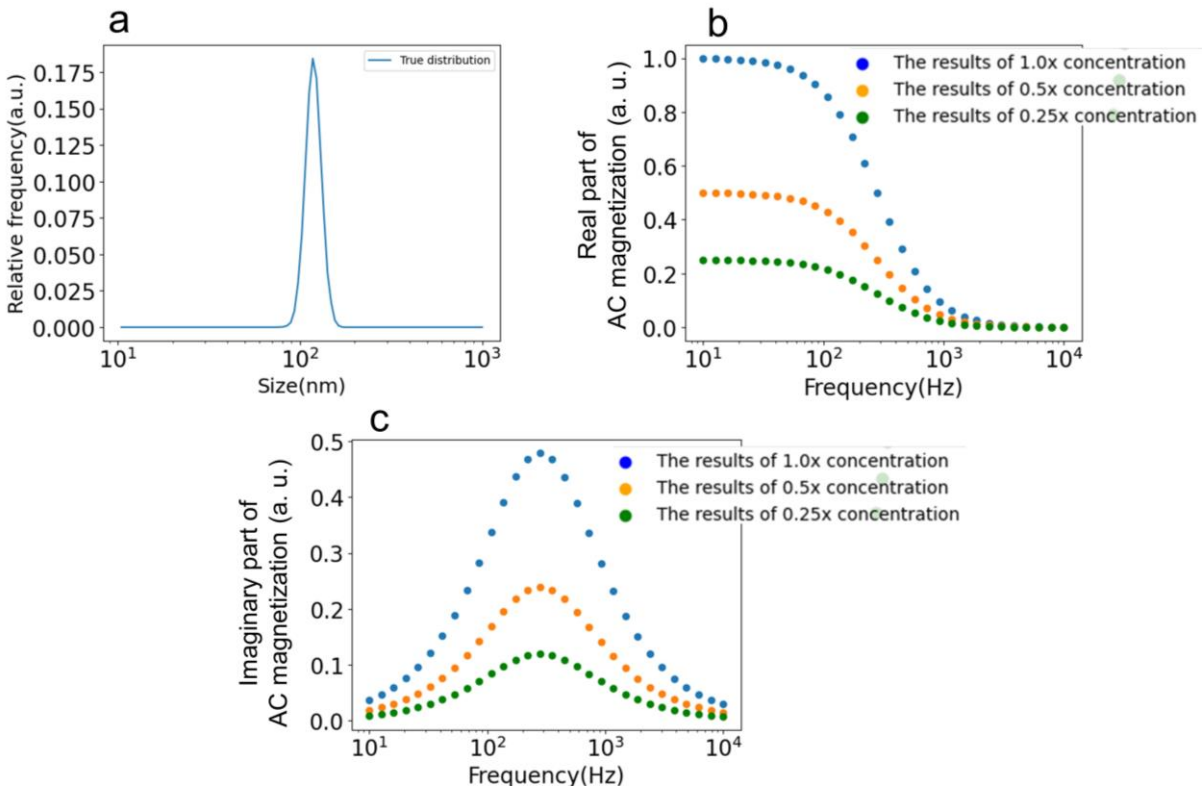

FIG. 3-4. (a) The generated distribution of MNP clusters, real parts (b) and imaginary parts (c) of calculated AC magnetization spectra via the generated distribution of MNP clusters.

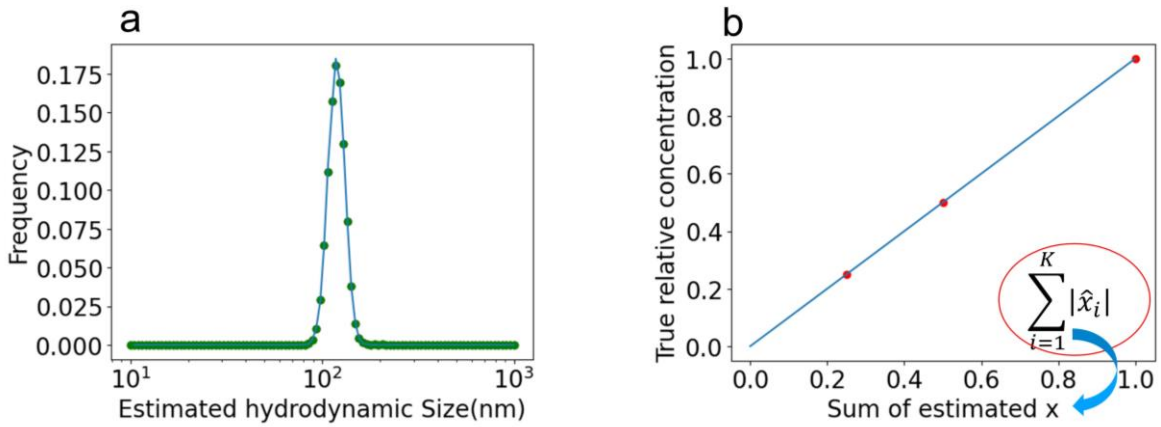

FIG. 3-5. (a) Estimated distributions of MNP clusters from AC magnetization spectra calculated from MNP clusters (b) the relationship between the true relative mass

concentration and the sum the sum of the absolute value of element in estimated vector $\hat{x}$ via eq (2-19) with λ equal to 10^{-4}.

In practical situations, AC magnetization spectra are derived from MNP clusters with both different distributions and concentrations. To confirm the feasibility of the proposed method for estimating mass concentrations of such AC magnetization spectra, we generated 30 different types of distributions of MNP clusters as shown in Fig 3-6(a) and used them to calculate AC magnetization spectra with different mass concentration of MNPs by using eq (2-10) with various M_0 ranging from 0.1 to 1. The real parts and imaginary parts of some examples of the calculated AC magnetization spectra are shown in Fig 3-6(b) and (c). Then eq (2-19) with λ equal to 10^{-4} was used to estimate vector $\hat{\boldsymbol{x}}$ and the sums of the absolute value of estimated vectors are calculated. The sums and the true relative mass concentration of MNP clusters are plotted in Fig 3-6 (d) to confirm their relationship. From the results, the sums and the true relative mass concentration of MNP clusters highly corresponded to each other, indicating the potential of the proposed method for estimating mass concentration of MNP clusters that follow Debye relaxation model.

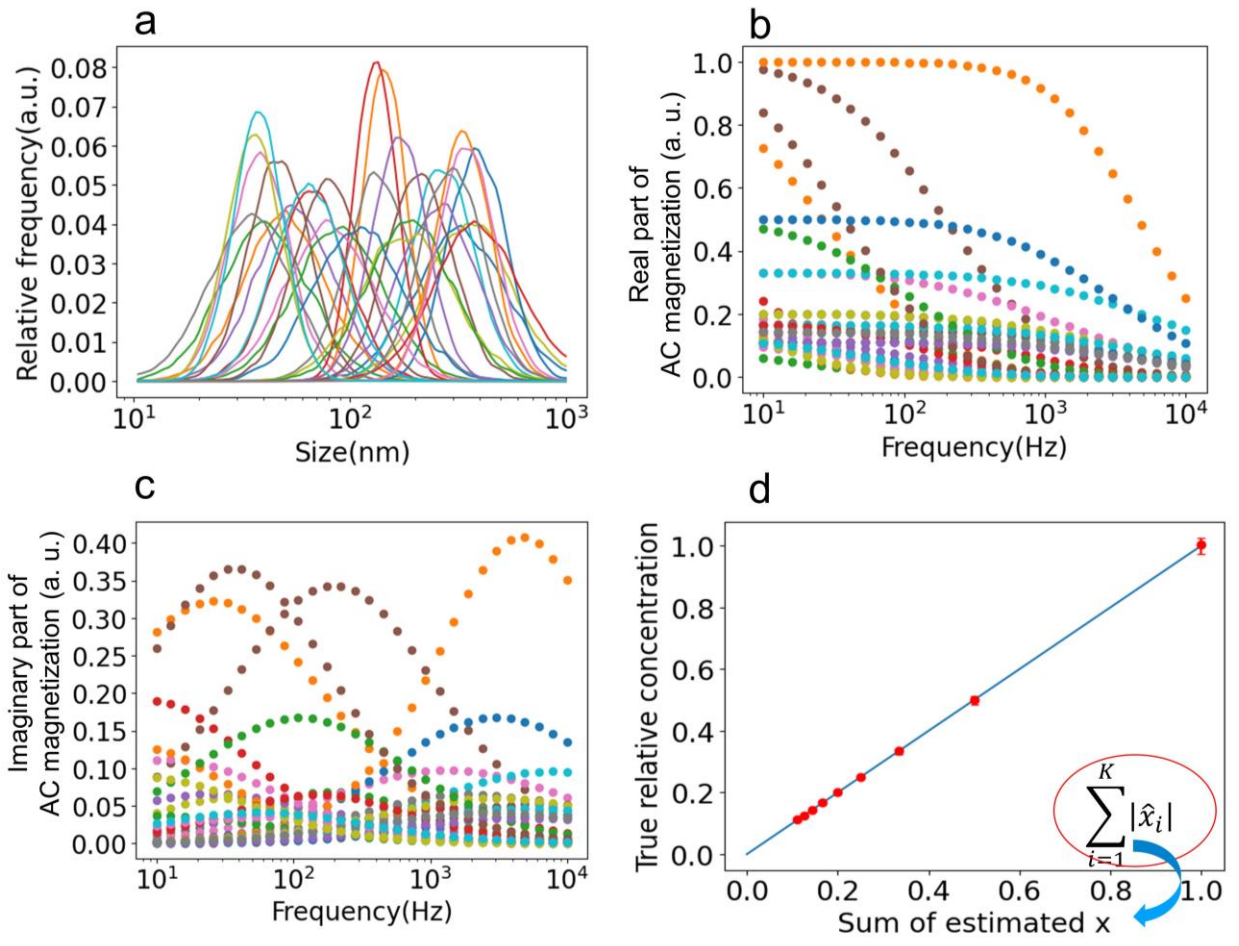

FIG. 3-6. (a) Generated distributions of MNP clusters, examples of real parts (b) and imaginary parts (c) of calculated AC magnetization spectra via the generated distribution of MNP clusters, and (d) the relationship between the true relative mass concentration and the sum the sum of the absolute value of element in estimated vector $\hat{\boldsymbol{x}}$ via eq (2-19) with λ equal to 10^{-4}.

3.4 Results estimated from imaginary part of simulation data

Results of the distributions of MNPs are estimated from the imaginary part of AC magnetization by using eq (20), (21) and (22). Fig. 3-7(a) shows the results of the R^2 score

between the true distribution (the same distribution used in Fig. 3-2) and the estimated distribution. The results as shown in Fig. 3-7(a) show a similar tendency with those as shown in Fig. 3-2(a), indicating that the distribution estimated from the imaginary part is also reliable comparing to that estimate from both the real and imaginary part. Fig. 3-7 (b) shows that the estimated distribution is highly consistent with the true distribution. In addition, the estimated results of MNPs with bimodal and multimodal distributions are also highly consistent with the true distributions as shown in Fig. 3-8. From the above results, we can say that there is almost no difference between the distributions estimated from the imaginary part and those estimated from the real and imaginary part.

In addition, the mass concentrations of MNPs are also estimated from the imaginary part (the same spectra those used in Fig. 3-6) and the results are shown in Fig. 3-9. By comparing Figs. 3-6 and 3-9, it was found that the error bar of the results estimated from the imaginary part is larger than that estimated from the real part and the imaginary part. However, the estimated results were also consistent with the relative mass concentration of MNPs. Above results indicate that the there is no significant difference between the results estimated from the imaginary part and those estimated from the real part and the imaginary part.

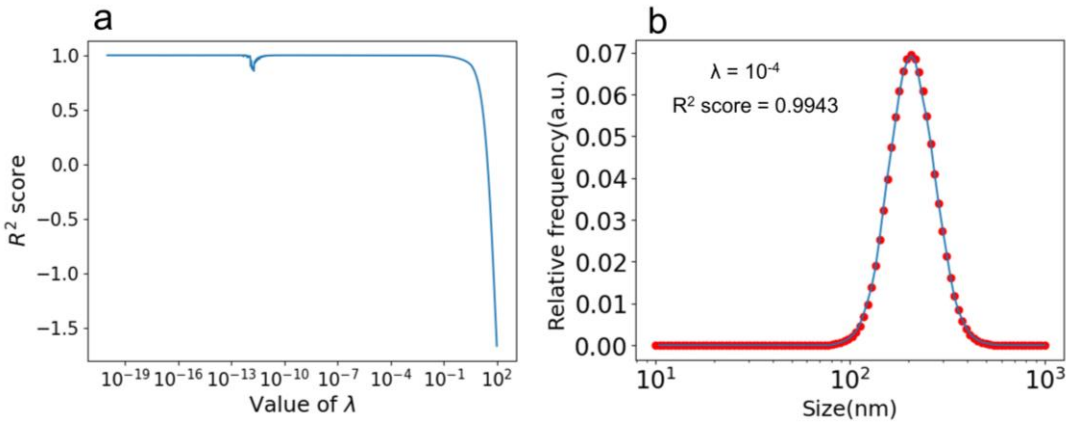

FIG. 3-7. (a) The relationship between the R^2 score and the value of λ. The R^2 score between the true distribution (used for calculating AC magnetization) and the estimated distribution (the R^2 score reaches the maximum value with λ equal to around 10^{-13}) (b) Comparison between the true distribution and the estimated distribution with λ equal to 10^{-4}. (The distribution is the same as that used in Fig. 3-2)

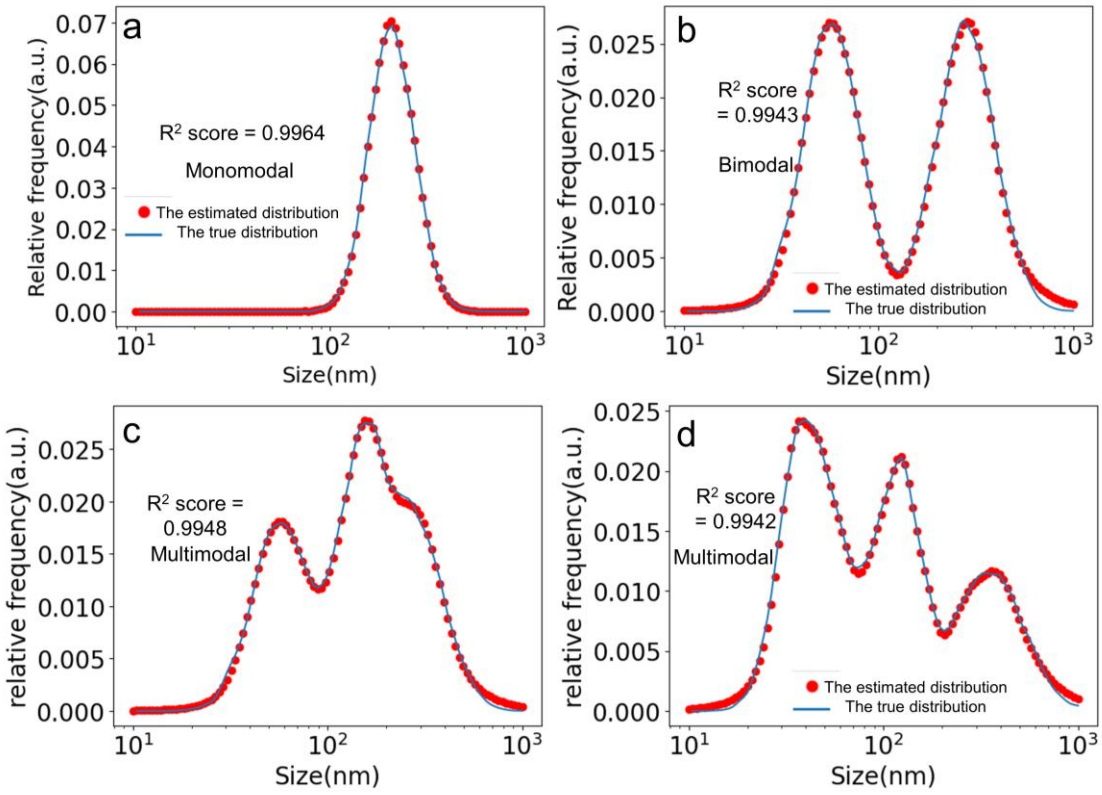

FIG. 3-8. Estimated distributions (λ is equal to 10^{-4}) of MNP clusters from the imaginary part of AC magnetization spectra calculated from MNP clusters with (a) monomodal distribution (b) Bimodal distribution λ = 1 (c) and (d) Multimodal distributions. (Distributions are the same as those used in Fig. 3-3)

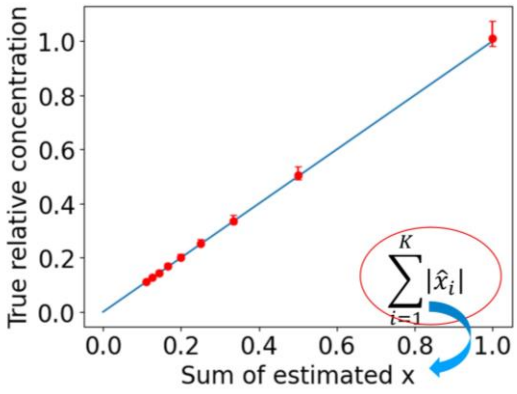

FIG. 3-9. The relationship between the true relative mass concentration and the sum the sum of the absolute value of element in estimated vector $\hat{\boldsymbol{x}}$ via eq (2-19) from the imaginary part with λ equal to 10^{-4}. (AC magnetization spectra are the same as those used in Fig. 3-6)

3.5 Summary

The feasibility of the proposed method on the simulation data for estimating the hydrodynamic size distribution and the mass concentration of MNPs was confirmed. For estimation of the distribution of MNPs, the distribution of MNPs was successfully estimated even if the distribution were bimodal and multimodal. For estimation of the mass concentration of MNPs, we observed a strong linear correlation between the sum of the absolute values of the estimated x and the mass concentration of the nanoparticles, even when the distributions of MNPs were various. Furthermore, we compared the results obtained from the imaginary part with those obtained from both the real and imaginary parts. From the results, it appeared that there is almost no difference in the estimated information including the distribution and the mass concentration of MNPs whether the imaginary part was used or both the real and imaginary parts were used.

3.6 Reference

[1] R.S. DiPietro, H.G. Johnson, S.P. Bennett, T.J. Nummy, L.H. Lewis, D. Heiman, Determining magnetic nanoparticle size distributions from thermomagnetic measurements, Appl. Phys. Lett. 96 (2010) 222506–222506. https://doi.org/10.1063/1.3441411.
[2] E.L. Crow, K. Shimizu, Lognormal distributions, Marcel Dekker New York, 1987.
[3] F. Ahrentorp, J. Blomgren, C. Jonasson, A. Sarwe, S. Sepehri, E. Eriksson, A. Kalaboukhov, A. Jesorka, D. Winkler, J.F. Schneiderman, M. Nilsson, J. Albert, T.Z.G. de la Torre, M. Strømme, C. Johansson, Sensitive magnetic biodetection using magnetic multi-core nanoparticles and RCA coils, J. Magn. Magn. Mater. 427 (2017) 14–18. https://doi.org/10.1016/j.jmmm.2016.10.041.

4 Analysis of AC magnetization spectra of pH-sensitive ferrogel

In chapter 3, the feasibility of the proposed method in **Section** 2.2 is confirmed by simulation data. To confirm the feasibility of the proposed method on experimental data, we apply the proposed method onto AC magnetization spectra of a synthesized pH-sensitive magnetic hydrogel (ferrogel). At first, this chapter discusses the motivation for using ferrogel and introduce the sensing mechanism by using ferrogel. Then the synthesis procedure and characterization methods of pH-sensitive ferrogel is described. The properties of synthesized ferrogel are investigated. Finally, this chapter also discusses the proof of concept of ammonia gas detection using the synthesized ferrogel and the proposed method.

4.1 Motivation for using ferrogel

Generally, magnetic nanoparticles are dispersed in solvents such as water or PBS buffer before being utilized for biosensing applications. However, in practical situations, the suspension medium often contains various substances, such as ions and biomolecules, which may lead to particle instability, aggregation, and then precipitation [1]. These issues significantly reduce the practicality of magnetic nanoparticles. To address this challenge, the utilization of magnetic gels has emerged as a potential solution. A ferrogel is a rheological magnetic material, which is a gel with magnetic particles dispersed in it, as shown in Fig. 4-1(a), and is one of the functional soft materials. As shown in Fig. 4-1(a), MNPs are separated by the polymer network of ferrogel, thus the issue of aggregation and precipitation can be overcome. In addition, since MNPs are separated by polymer network, it is reasonable to consider that the dipole-dipole interaction between MNPs is negligible. Thus, it is proper to

use the proposed method in **Section** 2.2. Although, this chapter only discusses the pH-sensitive ferrogel, by changing the stimuli type of hydrogel matrix, it is possible to use the sensing mechanism and the proposed method for various situations.

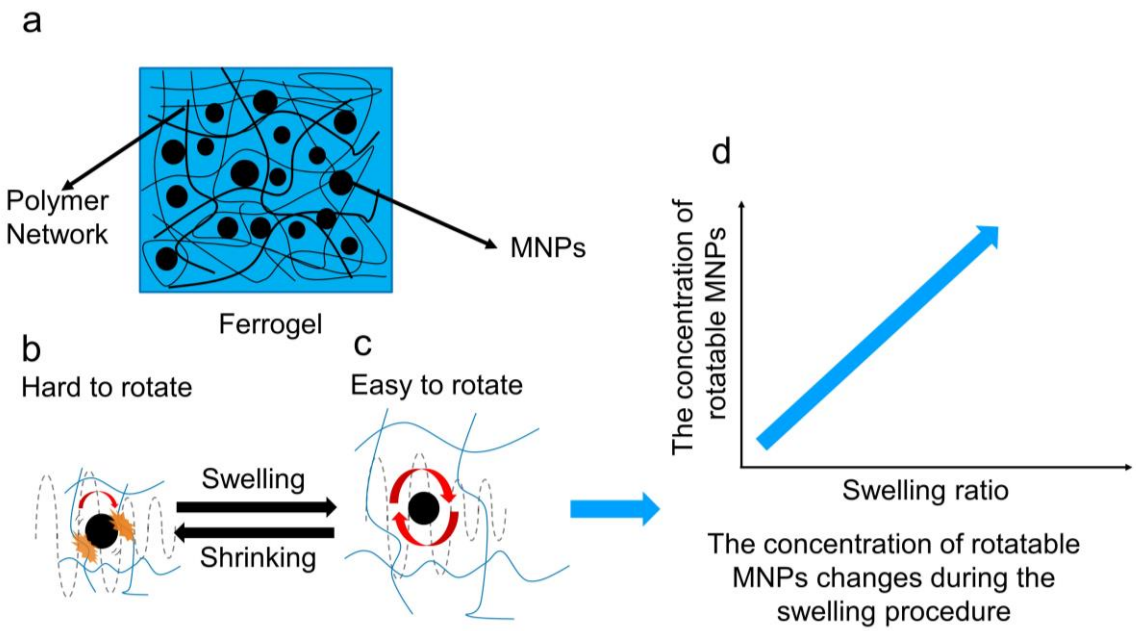

FIG. 4-1. Schematic illustration of ferrogel and hydrodynamic behavior of magnetic nanoparticles in the polymer network of the ferrogel.

4.2 Introduction of sensing mechanism of ferrogel

The applications of ferrogels are dependent on the interaction between the MNPs and gel matrix. In magnetic actuators [2] that use ferrogels, for instance, the displacement of the MNPs in response to the magnetic field induces the macroscopic deformation of the polymer gel due to the intense interaction between the MNPs and polymer matrix in the gel. For other applications, such as magnetically guided DDS ferrogel carriers [3], the polymer gel

containing the drug must interact powerfully with the MNPs, the source of the magnetic delivery.

In contrast, the magnetically induced deformation and movement do not occur efficiently in a system with weak interactions between the MNPs and the polymer matrix in the gel. This is due to the ineffective transmittance of the magnetic force induced in the MNPs to the deformation and movement of the gel matrix. Considering the ferrogels with the weak interaction between the MNPs and the polymer network of the hydrogel, the dispersed MNPs are able to rotate physically as their movement is not strongly restricted by the polymer network of the gel. In other words, although ferrogels appear as a solid at a macroscopic level, MNPs can be regarded as dispersed in a rheological environment, such as water. As mentioned in **Section** 2.1, when focusing on low frequency range (10~10kHz) that is the measurement frequency range in this chapter, only the Brownian relaxation will be discussed in the following of this chapter.

As shown in eq (2-2), there are two main factors influencing the Brownian relaxation time, which are the hydrodynamic size of MNPs and the viscosity of the medium. For MNPs encapsulated in ferrogel, the hydrodynamic size is considered as a constant. Thus, we focus on the viscosity. Since the viscosity of the medium in ferrogel is complicated, we call it the effective viscosity to simply analyze it. The effective viscosity of the media surrounding MNPs in the hydrogel depends on the interactions between water, the polymer gel matrix, and the MNPs. These interactions should be influenced by the polymer network structure in the ferrogel. For example, when the water content and the pore size of the network structure in the gel change depending on the swelling state, it is presumed that the effective viscosity of the environment around the MNPs changes. The changes in the pore size within the

polymer network owing to swelling or shrinking determine the degree of freedom of the physical rotation of the MNPs, thereby leading to changes in their hydrodynamic behavior, as depicted in Fig. 4-1(b) and (c). When the pore size of the hydrogel network becomes larger owing to the swelling of the hydrogel, the degree of rotation of the MNPs within the pores increases, leading to an increase in the concentration of rotatable MNPs (AC magnetization values) and relaxation frequency as shown in Fig. 4-1(d). In contrast, the concentration of rotatable MNPs and the relaxation frequency decrease with hydrogel shrinkage.

4.3 Synthesis procedure and characterization methods of pH-sensitive ferrogel

4.3.1 Synthesis and characterization of iron oxide MNPs

Iron oxide MNPs were synthesized using a solvothermal method [4]. First, 2 mmol of acetylacetone iron (III) (14024-18-1, Sigma-Aldrich; USA) was dissolved in 20 mL of tetraethylene glycol (112-60-7, Sigma-Aldrich; USA) at 343 K. The solution was subsequently sealed into two 10mL stainless pressure vessel and maintained at 523K for 15h inside electric furnace. After the completion of the reaction, the synthesized MNPs were washed with acetone, collected by centrifugation, and washed again several times with a mixture of DI water and ethanol. After being washed, the synthesized MNPs were dispersed in an aqueous solution of 2 g trisodium citrate (197-06025, Wako Chemicals; Japan) in 120 mL of DI water using a homogenizer at 343 K for surface modification with citric acid molecules. After the completion of the surface modification process, the MNPs were washed several times with a mixture of DI water and ethanol and subsequently dispersed in DI water. The primary and hydrodynamic sizes of the synthesized MNPs were determined by transmission electron microscopy (TEM, H-8100, Hitachi High-Tech Corporation; Japan)

and dynamic light scattering measurements (DLS, SZ-100V2, HORIBA; Japan), respectively. The crystallographic properties of the MNPs were investigated by X-ray diffraction (XRD, Rint2100; Rigaku, Japan).

4.3.2 Synthesis of pH-sensitive hydrogel and ferrogel

The pH-responsive sulfamethazine (SMZ)-based polymer hydrogels were synthesized using the Schotten–Baumann reaction [5]. The SMZ-based monomer was synthesized by binding an amino group of SMZ and a carbonyl group of methacryloyl chloride. First, 129 mmol of SMZ (57-68-1, TCI; Japan) was dissolved in a solvent mixture comprising 260 mL of DI water, 260 mL of acetone, and 129 mmol of sodium hydroxide (1310-73-2, Wako Chemicals; Japan). Thereafter, 129 mmol of methacryloyl chloride (920-46-7, TCI; Japan) was added dropwise to the SMZ solution, and the mixture was stirred overnight. The product was collected by filtration and washed thrice with pure water under ultrasonic stirring (USC-200Z38S-23, Ultrasonic Engineering Co., Ltd.; Japan). Finally, the product was dried under vacuum, which yielded a white powder. The synthesized SMZ-based monomer was characterized by Fourier transform infrared spectroscopy (FT-IR, FT/IR-460Plus, JASCO Corporation; Japan) and proton nuclear magnetic resonance spectroscopy (^{1}H NMR, JM-ECP, JEOL; Japan).

The SMZ-based polymer hydrogels were synthesized by the radical polymerization of the synthesized SMZ-based monomer using 2,2′-azobis (isobutyronitrile) (AIBN) as the initiator and subsequent gelation using *N*,*N*′-methylenebisacrylamide (MBAAm) as the cross-linker. A mixture of the SMZ-based monomer, AIBN (78-67-1, TCI; Japan), and MBAAm (110-26-9, Wako Chemicals; Japan) was prepared using 500 μL of dimethyl sulfoxide (DMSO)

(67-68-5, Wako Chemicals; Japan) as the solvent. The amount of the SMZ-based monomer used was varied over the range of 0.05–0.2 g. The AIBN-to-monomer and MBAAm-to-monomer molar ratios were set to 1 mol.% and 5–25 mol.%, respectively. Thereafter, the solution was maintained at 333 K in a water bath for 20 h. After the completion of the reaction, the formed hydrogel was washed with an aqueous NaOH solution (pH = 12) for 24 h.

The ferrogel was synthesized using the same process that gave the hydrogel, except that the ferrofluid containing the MNPs was also added. First, the solvent used for the MNP suspension was changed from DI water to DMSO. Thereafter, a 500 μL of DMSO solution containing the SMZ-based monomer, MBAAm, AIBN, and MNPs was prepared and subjected to mixing through vortexing and ultrasonication. The amounts of chemicals used for the synthesis of the hydrogels were the same as those used for preparing the SMZ-based polymer hydrogel. The MNP concentration in the solution was set at 10 mg/mL. The solution was maintained at 333 K in a tap water bath for 20 h. It was subsequently washed using an aqueous NaOH solution (pH = 12) for 24 h. During the washing process, the aqueous NaOH solution remained colorless and transparent, thereby indicating that MNPs did not diffuse out from the ferrogel. Therefore, it was assumed that the concentration of the MNPs in all the ferrogel specimens remained the same, i.e., 10 mg/mL.

4.3.3 Synthesis of pH-sensitive hydrogel and ferrogel

The swelling ratio, *SR*, can be evaluated considering the amount of water absorbed by the hydrogel. The underlying relation can be expressed as [6]

$$SR = \frac{W_s - W_d}{\mathrm{W}_d}, \qquad (4-1)$$

where W_s is the weight of the swollen specimen after being submerged in a solution and W_d is its weight in the dry state.

The same specimen was dipped in solutions with different pH values (7–12) for 24h prior to the *SR* measurements. Therefore, a single hydrogel specimen was repeatedly used to evaluate the pH dependence of the *SR*.

The synthesized ferrogel was placed in a solution with a known pH value for 24 h and subsequently subjected to AC magnetization measurements. By repeating this process using a single ferrogel specimen, the pH dependence of the AC magnetization characteristics of the ferrogel in question could be analyzed over the pH range of 7–12. The frequency dependence of the AC magnetization in the range of 10–10,000 Hz was analyzed using a physical property measurement system (PPMS, Quantum Design Corp.; USA) at a magnetic field amplitude of 0.8 kA/m at 300 K. In this chapter, we define and discuss the AC magnetization as the AC response of the magnetic moments per the mass of MNPs encapsulated in the ferrogel.

4.3.4 Demonstration of ammonia gas detection

An ammonia solution (1 mL, 25%) was placed in a round-bottom flask, and the ferrogel to be evaluated was placed in another round-bottom flask containing 5 mL DI water. The two flasks were subsequently connected via a stopcock and a plastic tube. The stopcock was opened to introduce the ammonia gas into the flask with the ferrogel to investigate the ammonia detection characteristics of the ferrogel. The exposure time was varied over 1–64 s by opening/closing the stopcock. After waiting for 4 h at each exposure time, the pH of the

DI water containing the ferrogel was measured using a pH meter, and the frequency dependence of the AC magnetization of the ferrogel was analyzed using the PPMS.

4.4 Properties of the synthesized MNPs

The XRD pattern of the synthesized iron oxide MNPs indicates a spinel structure. The primary particle size of the MNPs was determined via TEM (Fig. 4-2(a)), and their hydrodynamic size in water was evaluated by DLS measurements (Fig. 4-2(b)). The distribution of the primary particle size as determined from the TEM images was compared with the hydrodynamic size distribution obtained from the DLS measurements; the mean sizes are 19.77 ± 4.32 and 27±5.6nm, respectively. The hydrodynamic size of the MNPs was approximately 30% larger than the primary particle size. The zeta potential of the synthesized MNPs was −86 mV owing to their modification by citric acid molecules. These results indicate that the synthesized iron oxide MNPs were well dispersed in water, close to the monodisperse state.

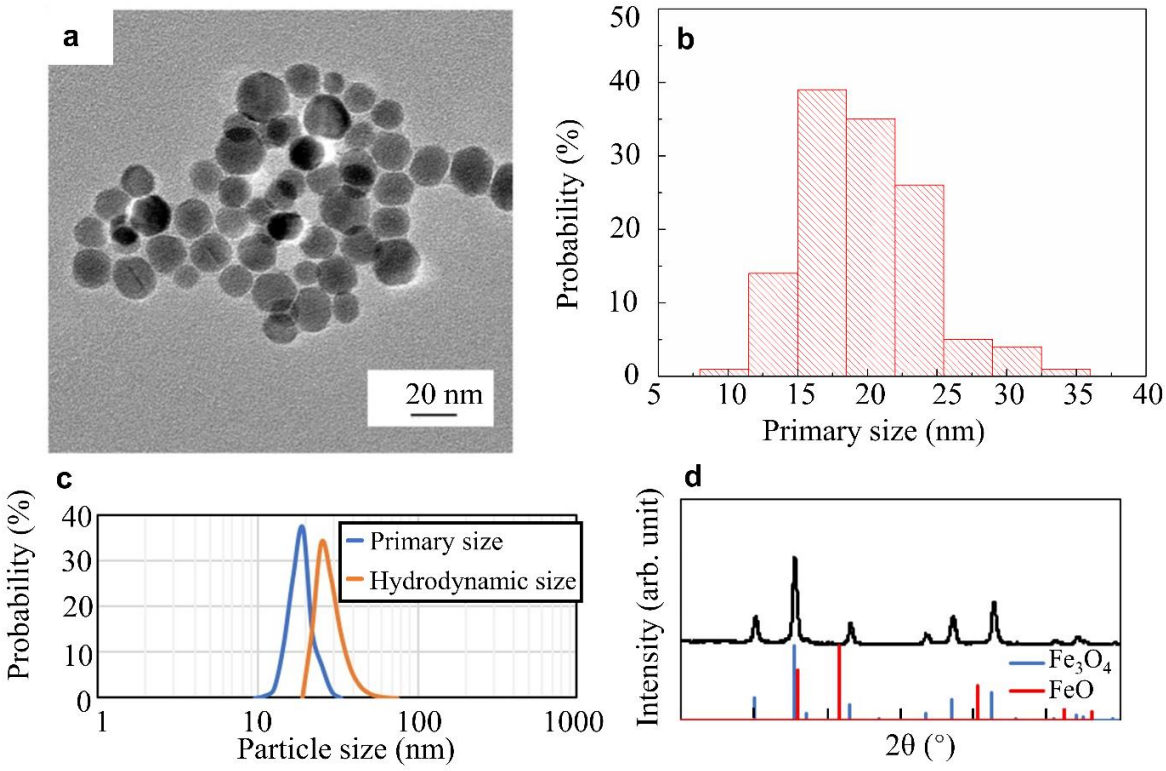

FIG. 4-2. (a) TEM image of synthesized MNPs along with (b) histogram of primary-size counted by TEM images (c) their primary-size distributions and hydrodynamic size, as determined via TEM and DLS measurements, respectively (d) XRD spectrum of synthesized MNPs.

4.5 Characterization of SMZ-based polymer hydrogels

To confirm that the synthesized monomer is SMZ-based, the FT-IR spectra of SMZ and the synthesized monomer were compared, as shown in Fig. 4-3(a). The stretching vibration bands at 3239, 3341, and 3440 cm^{-1} in the spectrum of SMZ as the raw material indicate that SMZ is a primary amine. Furthermore, there is only one band, at 3440 cm^{-1}, in the IR spectrum of the synthesized monomer, which is characterized to be a secondary amine formed by the reaction between the amino group of SMZ and acyl chloride. The bands at

1344 and 1303 cm^{-1} in both spectra indicate the presence of a sulfonyl group. The results of 1H NMR spectroscopy (Fig. 4-3(b)) indicate that the synthesized monomer contains all protons except those that belong to secondary amine. As the FT-IR results confirm the presence of a secondary amine, it is reasonable to assume that the synthesized monomer is SMZ-based. This monomer was subsequently used for hydrogel synthesis, as described below.

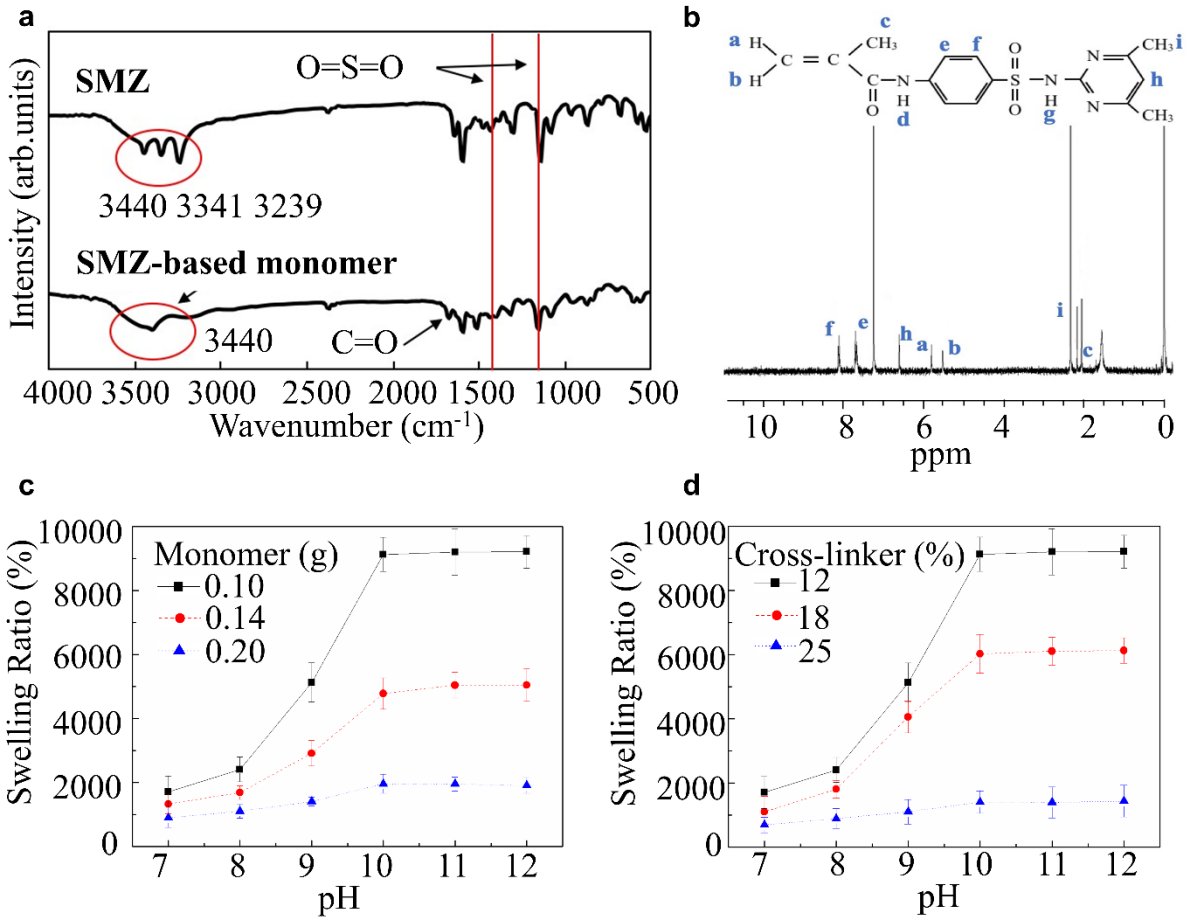

FIG. 4-3. (a) FT-IR spectra of SMZ and SMZ-based monomer and (b) 1H NMR profile of SMZ-based monomer. The alphabet a, b, c... in the spectrum represent the chemical shifts caused by the specific proton as shown in the structural formula of SMZ-based monomer.

The pH dependence of SR of SMZ-based polymer hydrogels synthesized using (c) different SMZ-based monomer concentrations and (d) different cross-linker-to-monomer ratio

To evaluate the effects of the monomer and cross-linker on the swelling behavior of the synthesized hydrogels, their *SR* values were plotted as a function of the pH (Fig. 4-3(c) and 4-3(d)), considering different monomer concentrations and cross-linker-to-monomer molar ratios. The use of small amounts of the monomer or a low cross-linker-to-monomer molar ratio results in substantial changes in the *SR* with an increase in the pH. According to a previous investigation of the relationship between *SR* and cross-linking density, the use of small amounts of the monomer or a low cross-linker-to-monomer molar ratio decreases the cross-linking density [7]. Hence, the *SR* increases as the cross-linking density of the hydrogel decreases [8]. Therefore, the above-described results are acceptable. Moreover, the pH range over which the *SR* changed significantly was 8–10 for all specimens, which corresponds to the sensitive pH range of the hydrogels reported in the previous study [5].

4.6 Swelling properties of ferrogels

As shown in Fig. 4-4(a) and 4-4(b), the ferrogels appeared brown in color owing to the presence of MNPs in the SMZ-based polymer hydrogels. Fig. 4-4 (c) and 4-4 (d) depict the dependence of the *SR* on the amount of the SMZ-based monomer used and the cross-linker-to-monomer molar ratio for ferrogels. A significant change in the *SR* of all the ferrogels is observable over the pH range of 8–10; The pH dependence of the *SR* of the hydrogels without the presence of MNPs exhibits a similar trend, as can be observed from Fig. 4-3(c) and 4-3(d). By comparing the results of the experiments using the same amounts of the monomer

and cross-linker (Fig. 4-3(c) and 4-4(d); monomer = 0.2 g, cross-linker-to-monomer ratio = 12%), it is observed that the *SR* of the ferrogels was smaller than that of the hydrogel, thereby indicating that the presence of the MNPs slightly decreases the *SR*. The findings indicate that a portion of the MNPs in the ferrogel function as a cross-linker. The effect of varying the amount of the monomer used (0.07–0.2 g) is shown in Fig. 4-4(c); the cross-linker-to-monomer molar ratio was kept at 25%. A significant change is observed in the *SR* for small amounts of the monomer used. Due to the high degree of chemical cross-linking, however, the high cross-linker-to-monomer ratio (25%) produces brittle ferrogels [9]. Note that a low monomer concentration produced fragile and difficult-to-manipulate ferrogels; therefore, a high monomer concentration is preferred. For further experiments, the concentration of monomer was therefore set at 0.2 g. As depicted in Fig. 4-4(d), the effect of the cross-linker-to-monomer molar ratio was evaluated over the range 5–25%. With a decrease in the cross-linker-to-monomer molar ratio, the change in SR over the pH 8–10 range is more pronounced.

To confirm the reusability of the synthesized ferrogels, a reversible swelling experiment was done, and the results are shown in Fig. 4-5. From the results, the reusability of the synthesized ferrogels was confirmed. Focusing on the maximum values on the SR, the maximum value of SR decreased during experiments, when the amount of monomer and ratio of cross-linker are 0.2g and 5% as shown in Fig. 4-5 (a), while the maximum value of SR increased in other samples as shown in Fig. 4-5 (b) and (c). Theoretically, there is possibility that the formation of the iron-ammonia complex will influence the reusability of the synthesized ferrogels. However, in this study, there is no strong evidence to support the existence of such influence.

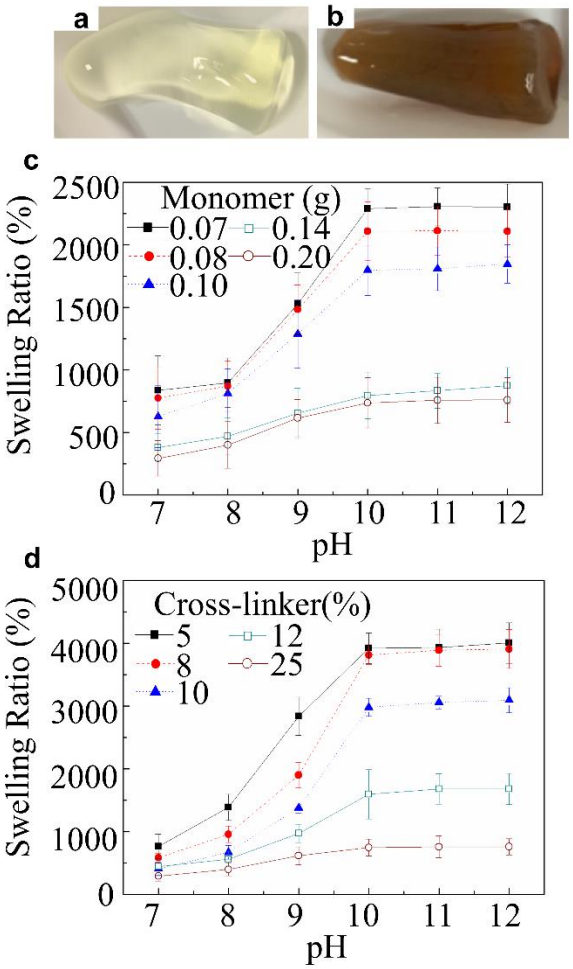

FIG. 4-4. (a) Photograph of SMZ-based hydrogel without MNPs and (b) photograph of ferrogel containing MNPs. The pH dependence of SR of ferrogels synthesized using (c) different SMZ-based monomer concentrations and cross-linker-to-monomer ratio of 25% and (d) different cross-linker-to-monomer ratios and 0.2 g of monomer.

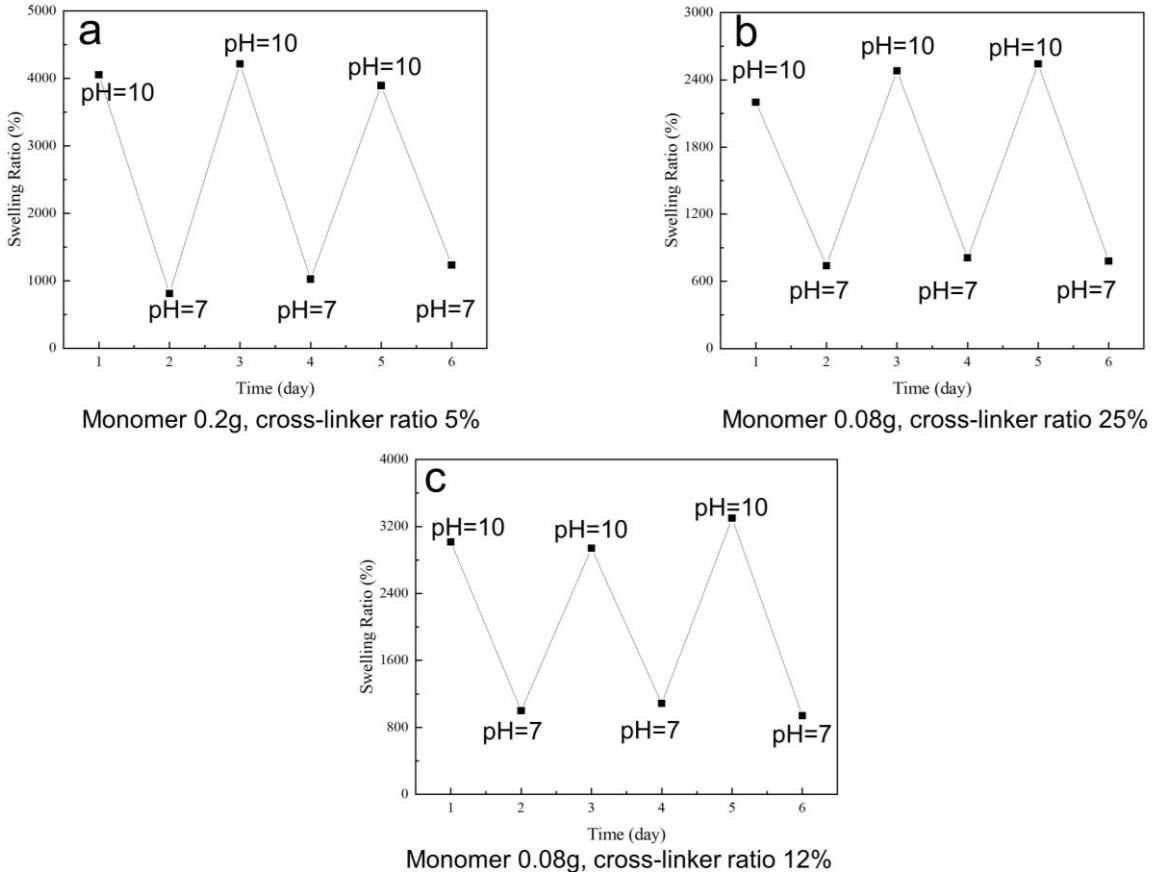

FIG. 4-5. Reversible swelling of hydrogels as a function of time under repeated changes in pH with the different amount of monomer and ratio of cross-linker (a) monomer 0.2g, cross-linker 5%, (b) monomer 0.08g, cross-linker 25%, (c) monomer 0.08g, cross-linker 12%.

4.7 AC magnetization of ferrogels

Based on the results discussed in **Section** 4.5, 0.2 g of the SMZ-based monomer was used, and the dependence of the AC magnetization on the cross-linker-to-monomer molar ratio was examined at ratios of 5 and 12%. This was done to investigate the relationship between the *SR* and the AC magnetization properties of the ferrogels and their pH dependence. The *SR* of the synthesized ferrogel with 5% cross-linker-to-monomer molar ratio (4,000% maximum)

was much higher than that with 12% cross-linker-to-monomer molar ratio (1,500%), as shown in Fig. 4-3(d). Furthermore, the frequency dependence of the AC magnetization for the ferrogels synthesized using 0.2 g of SMZ-based monomer and cross-linker-to-monomer molar ratios of 5% (Fig. 4-5(a) and 5(b)) and 12% (Fig. 4-5(c) and 4-5(d)) was evaluated. Fig. 4-4(a) and 4-4(c) depict the real part of AC magnetization while Fig. 4-5(b) and 4-5(d) depict the imaginary part.

At pH = 7, the real and imaginary values of the AC magnetization of the ferrogel synthesized using a cross-linker-to-monomer molar ratio of 5% were similar to those of 12%. As the two ferrogels shrank at pH = 7, their degrees of freedom for particle rotation were limited, resulting in the lowest AC magnetization values. Although the AC magnetization value increased with pH for the two ferrogels owing to swelling, the rate of increase for the ferrogel synthesized using a ratio of 5% was much higher than that for the ferrogel synthesized using a ratio of 12%; this correlates with the pH dependence of the *SR*, as illustrated in Fig. 4-4(d). Ferrogels with larger *SR*s exhibit significant Brownian relaxation and large AC magnetization values at the swelling state; the effective viscosity around the MNPs is reduced owing to the expansion of the pores in the polymer network because of the swelling.

As shown in Fig. 4-4(c) and 4-4(d), a significant increase in the real and imaginary values is observed from pH 8 to 10; in addition, a drastic increase in the *SR* is observed over the same pH range, as seen in Fig. 4-3 and 4-4. In particular, the significant change in response between pH 8.0 and 8.5 is considered because of the vast expansion of ferrogel in this pH range. According to our discussion above, the magnetization of the ferrogel is dependent on the Brownian relaxation of the MNPs

encapsulated within. The Brownian relaxation of the MNPs is determined by their rotation. As shown in Fig. 4-4, the swelling ratio of ferrogel changes significantly between pH 8.0 and 8.5, resulting in an increase in cell size due to the presence of additional water. The increase in cell size causes MNPs to be able to rotate more freely, leading to the significant change in the AC magnetization. Although the *SR* plateaus at pH higher than 10, a slight increase in the real and imaginary values of the AC magnetization is observed, in addition to the increase in the peak frequency of the imaginary part with the increase in the pH from 10 to 12. The changes observed in the pH range of 10–12 can be ascribed to electrostatic repulsion. When the pH was increased, the electrostatic repulsion between the MNPs, which were modified with citric acid molecules, was enhanced [10]. Therefore, their dispersion and hydrodynamic states in the ferrogel improved; the effective hydrodynamic size of the MNPs and the effective viscosity around them were reduced.

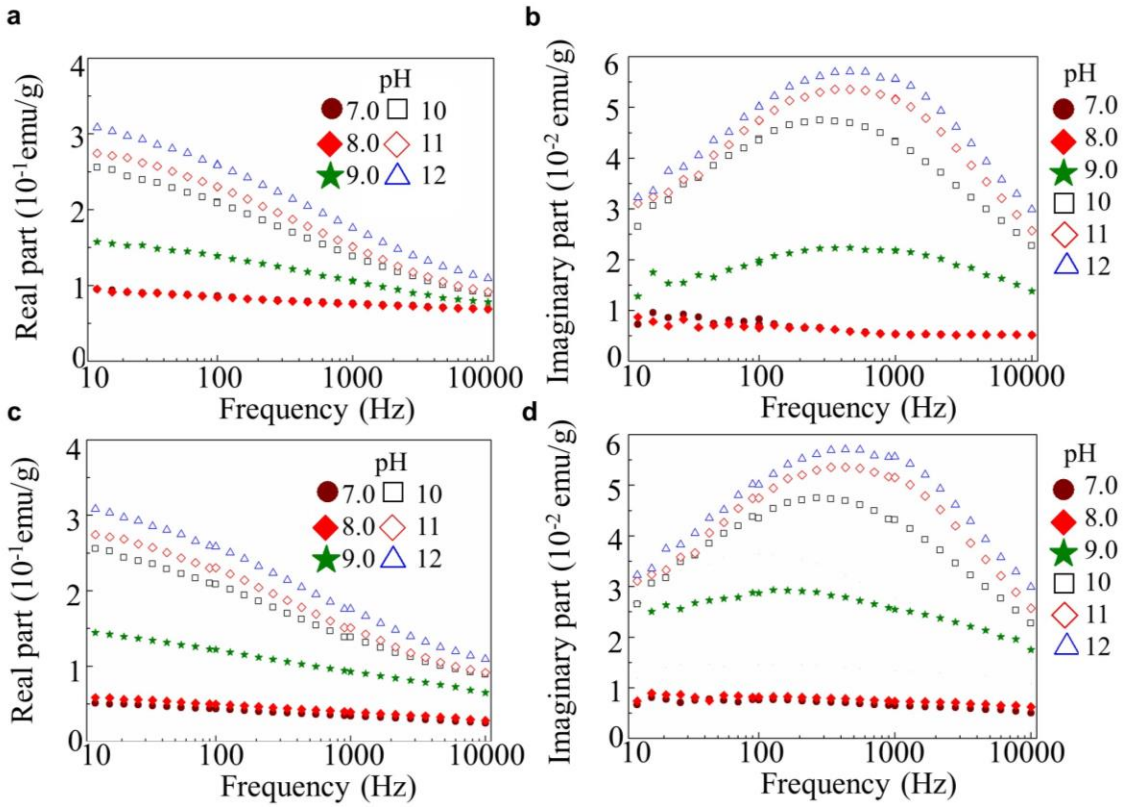

FIG. 4-6. Frequency dependence of AC magnetization of MNPs encapsulated inside ferrogels evaluated by varying pH values in the 7–12 range. Ferrogels synthesized using 0.2 g of SMZ-based monomer and cross-linker-to-monomer ratio of (a, b) 12% and (c, d) 5%. Curves in (a, c) show the real part of AC magnetization while those in (b, d) show the imaginary part.

These results suggest that the pH dependence of the AC magnetization of the synthesized ferrogels makes them suitable for use in pH-sensing devices operating in the alkaline-pH region. In particular, the notable changes observed over the pH range of 8–10 inspired us to develop a device using the ferrogel as a sensing label to detect trace amounts of ammonia gas, which commonly emanates from human skin [11], because ammonia gas readily dissolves in water.

4.8 Demonstration of ammonia gas detection

Using the setup shown in Fig. 4-6(a), ferrogel synthesized with 0.2g monomer and 5% cross-linker is used to detect ammonia gas. The ammonia gas released from the aqueous ammonia solution is introduced through the connecting tube into the vial containing the ferrogel and 5 mL of DI water upon opening the stopcock. The opening time, or the duration of exposure to ammonia gas, determined the concentration of ammonia absorbed by ferrogel from DI water. The concentration of ammonia absorbed by the DI water surrounding the ferrogel has been determined using Fick's law. To simplify the calculations, steady-state diffusion conditions were postulated so that Fick's first law can be applied. [12]. In addition, we assumed the temperature stayed constant at 298.15 K and the diffusion coefficient was 2.3×10^{-5} m^2/s [13]. The concentration gradient was calculated from the concentration of ammonia gas in the source flask and the length of the tube. The concentration in the source flask was calculated by assuming an ideal gas and a vapor gas pressure of 6.8×10^3 Pa [14]. All above data were substituted into the equation of Fick's first law in order to compute the ammonia gas diffusion flux. The amount of ammonia absorbed in the DI water containing the ferrogel was calculated by multiplying the diffusion flux with the measured cross-sectional area of the tube and the exposure time. Note that sufficient time was allowed for the absorption of the ammonia gas, and it was assumed that all the evaporated ammonia is absorbed by the DI water with the ferrogel. To verify the accuracy of the calculations, the corresponding pH value of the absorbed ammonia was calculated using dissociation constant value of ammonia, which is subsequently compared to the pH value measured using a pH meter (Fig. 4-6(b)). A high R^2 score equal to 0.996 between the calculated and measured pH

values indicates that the calculated concentration of ammonia absorbed can be used to estimate the concentration of ammonia gas sensing by the prepared ferrogel.

As depicted in Fig. 4-6(c), the real part of the AC magnetization spectra increased as the opening time of the stopcock increased, which corresponds to an increase in pH value due to an increase in ammonia concentration. This behavior resembles the pH dependence of the AC magnetization depicted in Fig. 4-5(c). In addition, the change in the imaginary part as a function of frequency for various exposure times, as shown in Fig. 4-6(d), is comparable to that observed for different pH values (Fig. 4-5(d)). Due to the expansion of the pores in the polymer network, which occurred as a result of the swelling of the ferrogel with increasing pH after ammonia absorption, the MNPs were able to rotate easily in the ferrogel.

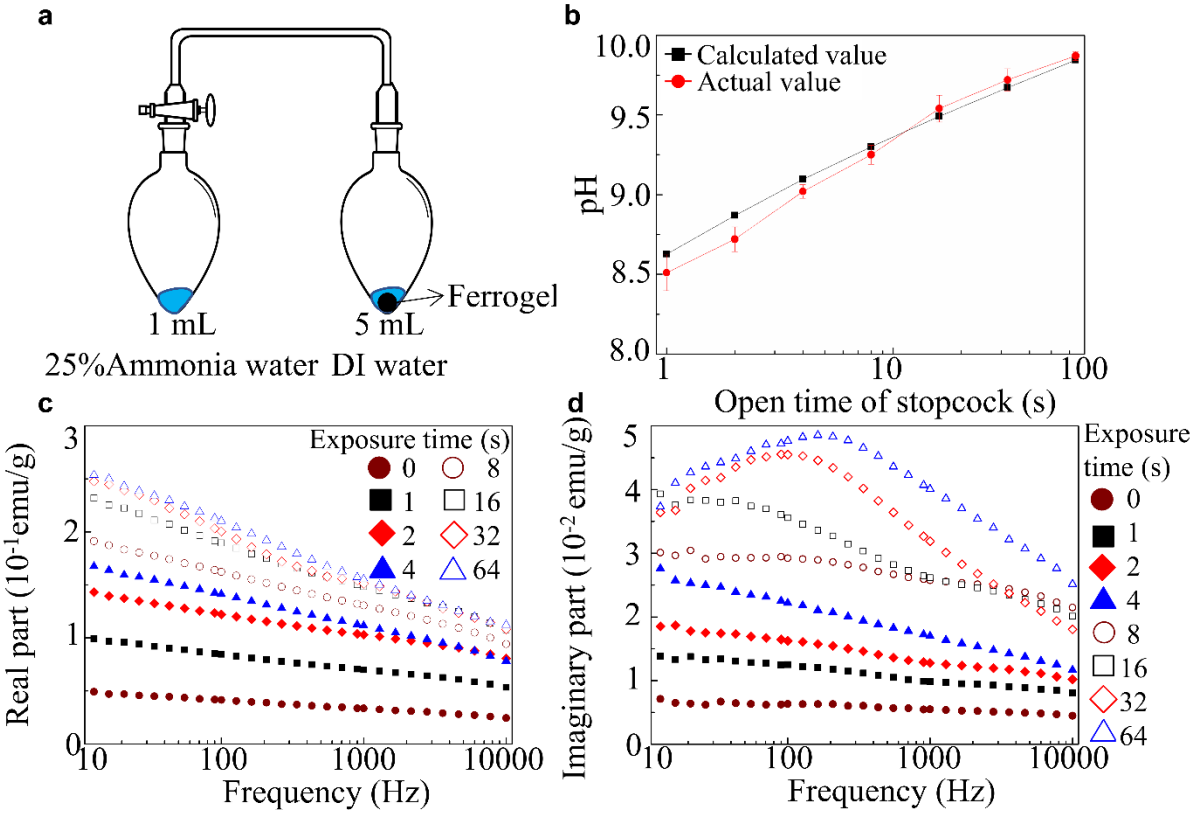

FIG. 4-7. Ammonia-gas detection using SMZ-based polymer ferrogel: (a) experimental setup, (b) pH changes as a function of ammonia-exposure time (calculated using Fick's first law and measured using a pH meter), (c) real and (d) imaginary parts of AC magnetization of MNPs encapsulated inside ferrogel exposed to ammonia gas as a function of frequency for various ammonia exposure times, and (e) the relationship between the real part of AC magnetization at a frequency of 100 Hz and the calculated concentration of ammonia absorbed by ferrogel.

As depicted in Fig. 4-1, the concentration of rotatable MNP encapsulated inside ferrogel increased with the increase in swelling ratio of ferrogel by absorption of ammonia gas. Thus, it is possible to the concentration of rotatable MNP encapsulated inside ferrogel to detect the concentration of absorbed ammonia gas. Two methods (Method A and Method B) were used to realize it, which were (A) usage the value of the real part of AC magnetization spectra (because the value of the real part of AC magnetization spectra corresponds to the number of), and (B) the proposed method as mentioned in **Section** 2.2 and confirmed in **Section** 3.3 via the sum of the absolute value of the element of estimated $\hat{\boldsymbol{x}}$ obtained by eq (2-19). To use Method A, it was necessary to select a frequency point to represent the value of the AC magnetization spectrum, here we selected 100Hz. To use Method B, we selected 0.1 as the value of the regularization parameter λ in eq (2-19). Results obtained via two methods are shown in Fig 4-7. From Fig. 4-7(a) and (b), the results obtained via Method B show a higher R^2 score than that obtained via the Method A. The possible reason is considered as the usage of information in AC magnetization spectra. For Method A, only the values at a fixed frequency point were used, resulting in that both the real part and the imaginary part of AC

magnetization spectra were not fully used. Comparing to Method A, Method B focused on each data point of both the real and imaginary part of AC magnetization spectra, resulting in that the fully usage of the spectra. Note that we don't show results of distributions of MNPs encapsulated inside ferrogel. The reason is in the structure of ferrogel. Encapsulated MNPs are separated by the polymer network of ferrogel and fixed in pores of ferrogel, resulting in that the distributions of MNP encapsulated inside ferrogel don't change during swelling procedures.

We also investigated the effect of regularization parameter λ in eq (2-19) compare the results of concentrations of rotatable MNPs estimated from the whole (both the real and imaginary part) and the imaginary part of AC magnetization spectra. For both results, the R^2 score with large λ was higher than that with smaller λ. We consider it was caused by the noise in the AC magnetization spectra. When λ was small, eq (2-19) is sensitive to the noise, resulting in an inaccurate estimation of the mass concentration of encapsulated MNPs. In contrast, when λ was relatively large, the magnitude of estimated $\hat{\boldsymbol{x}}$ is restricted to a small value, then the influence of noise is lower. In addition, the R^2 score as shown in Fig. 4-8(b) is higher than that in Fig. 4-8(a), indicating that only using the imaginary part of AC magnetization spectra is prefer for these measured spectra. The possible reason is that there are more overlapping parts in the real part, which influences the estimation.

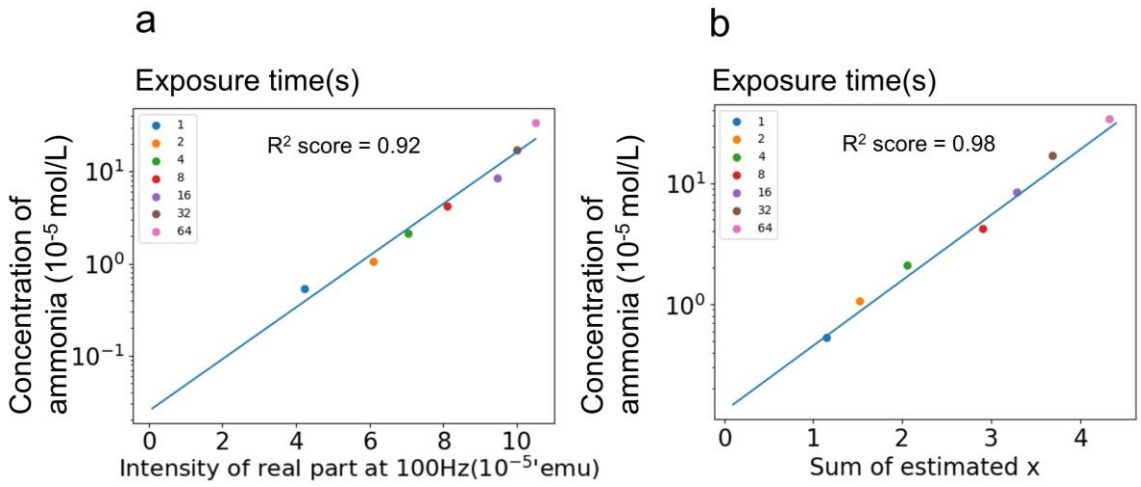

FIG. 4-8. (a) The relationship between the real part of AC magnetization at a frequency of 100 Hz and the calculated concentration of ammonia absorbed by ferrogel (where the blue line is the linear regression between the intensity of real part at 100Hz and the concentration of ammonia gas), (b) the relationship between the sum of the absolute value of element in estimated vector $\hat{\boldsymbol{x}}$ via eq (2-19) with λ equal to 0.1 and the calculated concentration of ammonia absorbed by ferrogel (where the blue line is the linear regression between the sum of the absolute value of element in estimated vector $\hat{\boldsymbol{x}}$ and the concentration of ammonia gas).

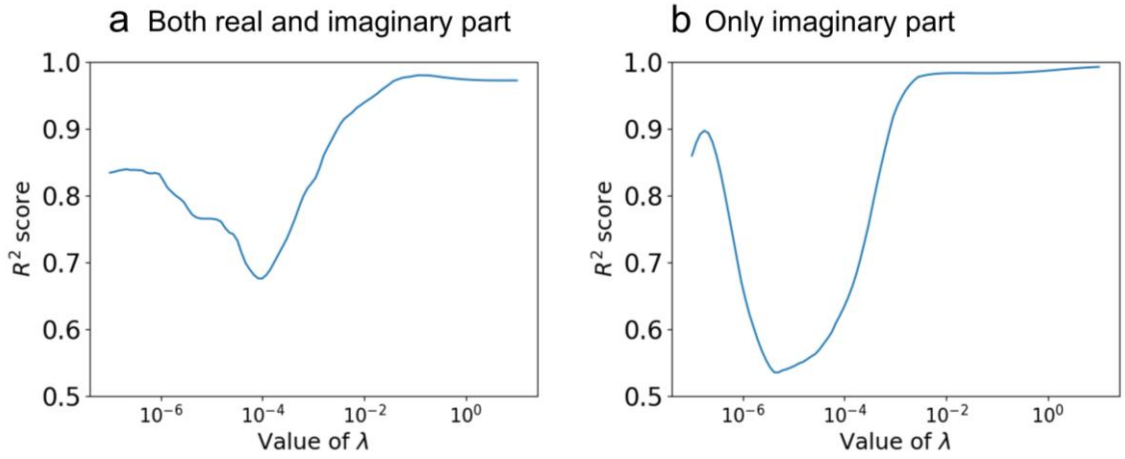

FIG. 4-9. Results of the relationship between the R^2 score (which is the R^2 score of linear regression between the sum of the absolute value of element in estimated vector $\hat{x}$ and the

concentration of ammonia gas as shown in Fig 4-8) and the value of λ: (a) both the real and the imaginary part are used for estimating the estimated vector $\hat{\boldsymbol{x}}$, (b) only the imaginary part are used for estimating the estimated vector $\hat{\boldsymbol{x}}$.

The concentration after exposure to ammonia for 1 s was only 5.3×10^{-6} mol/L, which is one-tenth of that of the solution obtained by dissolving the ammonia gas emitted from a 4-cm^2 area on the neck of a human subject for 4 h in 5 mL water [15]. Therefore, the synthesized ferrogel can be used to detect the ammonia gas emitted from the human body to monitor human health. Fig. 4-9 shows a schematic illustration of a wearable ammonia-gas sensing device combining the ferrogel as a label and a separate AC magnetic sensor. The wearable component containing the ferrogel is used to collect ammonia gas emitted from the human body for a period of time, and then the ammonia gas is detected by measuring the magnetization of the ferrogel contained within the wearable part using the AC magnetic sensor. The period ammonia data collected can be used for health monitoring as shown in Fig. 4-10, because of the important role of ammonia in metabolism as shown in Fig. 4-11 according to previous studies [16-18].

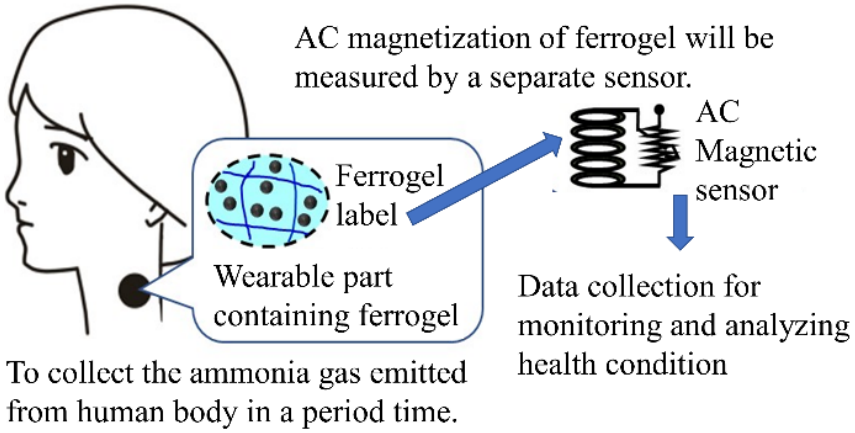

FIG. 4-10. Schematic illustration of a wearable ammonia-gas sensing device using the ferrogel label and AC magnetic sensor.

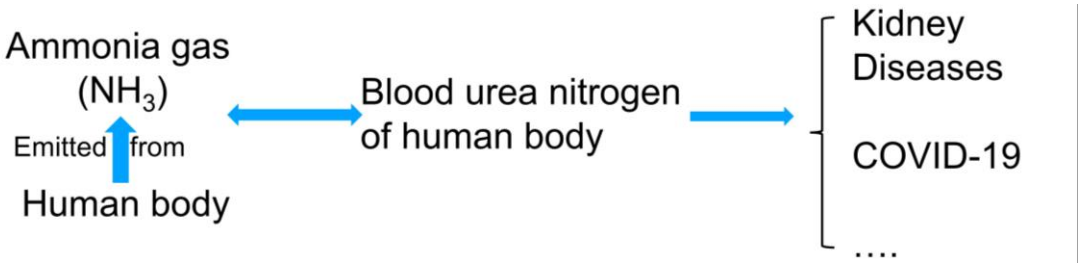

FIG. 4-11. Relationship between emitted ammonia gas and human health.

4.9 Summary

A pH-sensitive ferrogel was successfully synthesized. The synthesized ferrogels swelled in the alkaline-pH region, and their SR increase with an increase in the pH. The AC magnetization behavior of the incorporated MNPs is modulated by the swelling of the hydrogel in response to changes in pH over the range of 7-12. In addition, the ferrogels with larger swelling ratios exhibited enhanced Brownian relaxation during AC magnetization. Based on the pH response of the AC magnetization, the detection of ammonia gas was investigated using the ferrogel as a sensing label. The concentration of absorbed ammonia gas was estimated by the mass concentration of rotatable MNPs estimated vis the proposed method with a high R^2 score. Based on the above results, the synthesized ferrogel showed the potential for use as a sensing label in applications such as the sensing of ammonia emitted from human skin for health monitoring.

4.10 Reference

[1] B.I. Kharisov, H.V.R. Dias, O.V. Kharissova, A. Vázquez, Y. Peña, I. Gómez, Solubilization, dispersion and stabilization of magnetic nanoparticles in water and non-Aqueous solvents: Recent trends, RSC Adv. 4 (2014) 45354–45381. https://doi.org/10.1039/c4ra06902a.

[2] L.E. Faidley, Y. Han, K. Tucker, S. Timmons, W. Hong, Axial strain of ferrogels under cyclic magnetic fields, Smart Mater. Struct. 19 (2010) 75001–75001. https://doi.org/10.1088/0964-1726/19/7/075001.

[3] G. Giani, S. Fedi, R. Barbucci, Hybrid Magnetic Hydrogel: A Potential System for Controlled Drug Delivery by Means of Alternating Magnetic Fields, Polymers. 4 (2012) 1157–1169. https://doi.org/10.3390/polym4021157.

[4] D. Mishra, R. Arora, S. Lahiri, S.S. Amritphale, N. Chandra, Synthesis and characterization of iron oxide nanoparticles by solvothermal method, Prot. Met. Phys. Chem. Surf. 50 (2014) 628–631. https://doi.org/10.1134/S2070205114050128.

[5] S.Y. Park, Y.H. Bae, Novel pH-sensitive polymers containing sulfonamide groups, Macromol. Rapid Commun. 20 (1999) 269–273. https://doi.org/10.1002/(SICI)1521-3927(19990501)20:5<269::AID-MARC269>3.0.CO;2-3.

[6] S.J. Kim, S.J. Park, S.I. Kim, Swelling behavior of interpenetrating polymer network hydrogels composed of poly(vinyl alcohol) and chitosan, React. Funct. Polym. 55 (2003) 53–59. https://doi.org/10.1016/S1381-5148(02)00214-6.

[7] S. Ilić-Stojanović Snežana, L. Nikolić, V. Nikolić, M. Stanković, J. Stamenković, I. Mladenović-Ranisavljević, S. Petrović, Influence of monomer and crosslinker molar ratio on the swelling behaviour of thermosensitive hydrogels, Chem. Ind. Chem. Eng. Q. 18 (2012). https://doi.org/10.2298/CICEQ110711040I.

[8] A. Erdem, F.A. Ngwabebhoh, U. Yildiz, Synthesis, characterization and swelling investigations of novel polyetheramine-based hydrogels, Polym. Bull. 74 (2017) 873–893. https://doi.org/10.1007/s00289-016-1751-y.

[9] C. Norioka, Y. Inamoto, C. Hajime, A. Kawamura, T. Miyata, A universal method to easily design tough and stretchable hydrogels, NPG Asia Mater. 13 (2021) 34–34. https://doi.org/10.1038/s41427-021-00302-2.

[10] L. Vékás, D. Bica, M.V. Avdeev, Magnetic nanoparticles and concentrated magnetic nanofluids: Synthesis, properties and some applications, China Particuology. 5 (2007) 43–49. https://doi.org/10.1016/j.cpart.2007.01.015.

[11] F.M. Schmidt, O. Vaittinen, M. Metsälä, M. Lehto, C. Forsblom, P.-H. Groop, L. Halonen, Ammonia in breath and emitted from skin, J. Breath Res. 7 (2013) 17109–17109. https://doi.org/10.1088/1752-7155/7/1/017109.

[12] A. Fick, Ueber diffusion, Ann. Phys. 170 (1855) 59–86.

[13] Spiller LL, Determination of ammonia/air diffusion coefficient using nafion lined tube, Anal. Lett. 22 (1989) 2561–2573.

[14] Perry JH, Chemical engineers' handbook, McGraw-Hill Companies, 1973.

[15] S. Furukawa, Y. Sekine, K. Kimura, K. Umezawa, S. Asai, H. Miyachi, Simultaneous and multi-point measurement of ammonia emanating from human skin surface for the estimation of whole body dermal emission rate, J. Chromatogr. B. 1053 (2017) 60–64. https://doi.org/10.1016/j.jchromb.2017.03.034.

[16] P. P. Ricci, O. J. Gregory, Sensors for the detection of ammonia as a potential biomarker for health screening, Sci. Rep. 11(1) (2021) 7185. https://doi.org/10.1038/s41598-021-86686-1.
[17] N. T. Brannelly, , J. P. Hamilton-Shield, and A. J. Killard. "The measurement of ammonia in human breath and its potential in clinical diagnostics." Crit. Rev. Anal. Chem. 46(6) (2016) 490-501. https://doi.org/10.1080/10408347.2016.1153949
[18] M. Li, C. J. Weschler, G. Beko, P. Wargocki, G. Lucic, J. Williams, Human ammonia emission rates under various indoor environmental conditions. Environ. Sci. Technol. 54(9) (2020) 5419-5428. https://doi.org/10.1021/acs.est.0c00094.

5 Analysis of AC magnetization spectra of biomolecule detection

In chapter 4, we confirmed the feasibility of the proposed method in **Section** 2.2 by experimental data obtained by pH-sensitive ferrogel for ammonia gas detection. The assumption of the proposed method in **Section** 2.2 is that the dipole-dipole interaction between MNPs is negligible. However, when detecting biomolecules in liquid phase by magnetic susceptometry, MNPs aggregate via target biomolecules, resulting in the dipole-dipole interaction between MNPs cannot be negligible. Then Debye relaxation model cannot be used to explain the behavior of MNP clusters accurately. To overcome this issue, we proposed the experimental method as described in **Section** 2.3. This chapter discusses the feasibility of the experimental model on experimental data of the detection of streptavidin (SA). At first, we discuss how to form the matrix equation as described in **Section** 2.3. Then the estimated hydrodynamic size distribution of MNP clusters is evaluated with the DLS results. Note that the estimated hydrodynamic size distribution of MNP clusters is described by the number distribution of different MNP clusters. The estimated distribution of MNP clusters is used to establish a linear model to detect the concentration of SA.

5.1 Synthesis and characterization method

The method for synthesizing citric acid modified MNPs was as same as **Section** 4.3.1. MNPs were separated with the different cluster size by adjusting the rotation speed of centrifugation. MNPs were separated to four different clusters, which are MNP cluster type 0, 1, 2 and 3 in ascending order of hydrodynamic size. The MNP cluster type 0 was used for further biotin modification. After modification, we call the obtained four clusters as C_0', C_1',

C_2' and C_3' as shown in Fig. 5-1. The involvement of biomolecules such as SA and biotin in cluster formation was assumed to be negligible. By the above assumption, we considered it is possible to use the number distribution of MNP clusters (C_0', C_1', C_2' and C_3') to approximate the number distribution of MNP–SA clusters (C_0, C_1, C_2 and C_3). The hydrodynamic size of separated MNP clusters is measured by DLS. The frequency dependence of the AC magnetization spectra in the range of 10-10,000 Hz was analyzed using a PPMS at a magnetic field strength amplitude of 0.8 kA/m at 300 K. Note that the AC magnetization in chapter represents the AC magnetic response of the moment per the mass of MNPs suspended in the suspension.

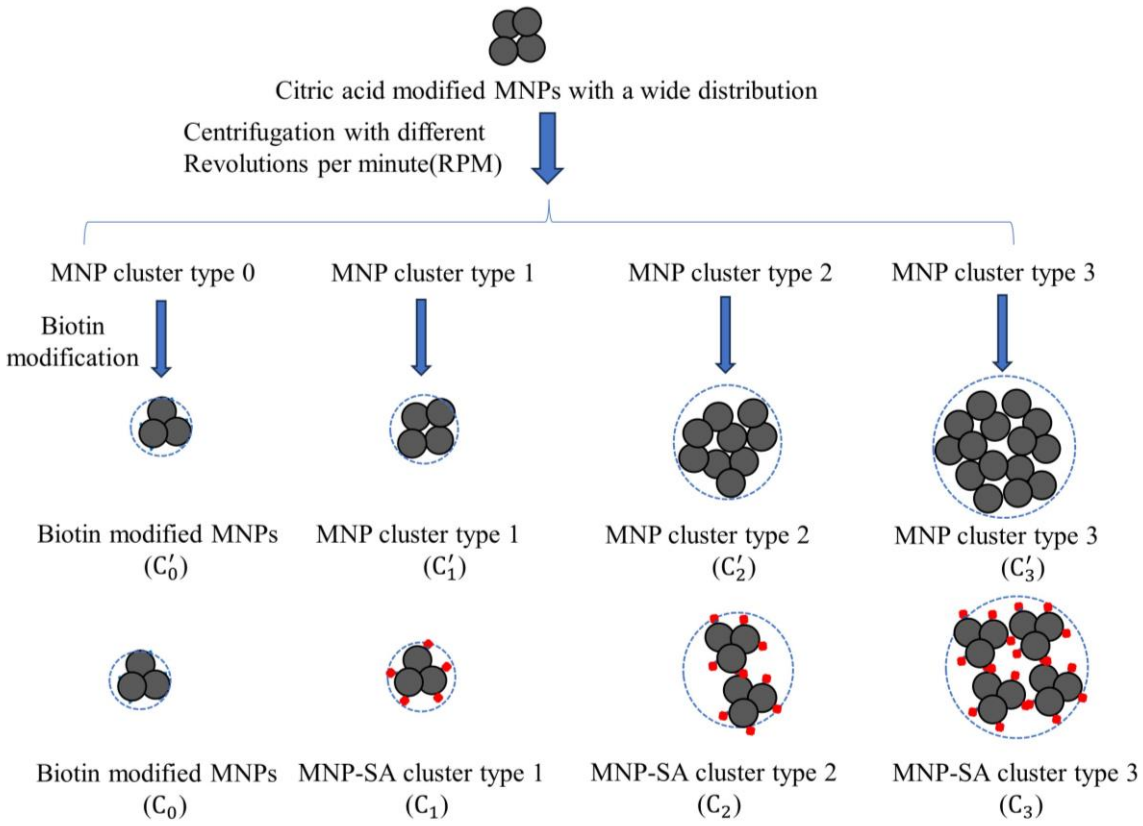

FIG. 5-1. Flowchart for separating MNP clusters used for the experimental model.

In order to interact with SA, a biotin modification was performed. A suspension of 400μL 5 mg/ml of citric acid-modified iron oxide nanoparticles was mixed with 400μL DI water. NHS (106627-54-7, TCI; Japan) and EDC (25952-53-8, TCI; Japan) were dissolved into the mixture with the mass up to 43.4 mg and 38.3mg and put the mixed suspension onto the shaker for reaction for 2 hours. After shaking, NHS-esterified iron oxide nanoparticles were washed several times by DI water and then dispersed in 800 μL of DI water. The obtained suspension of NHS esterified iron oxide nanoparticles is mixed with Amine-PEG2-Biotin (138529-46-1, TCI; Japan) and triethylamine (121-44-8, TCI; Japan) with concentration up to 0.2 mM and 1 mM, respectively, and shaken for 1 hour. After shaking, biotin-modified iron oxide nanoparticles were washed by DI water via centrifugation and redispersed into 800 μL DI water. The particle suspension was mixed with 2-aminoethanol (141-43-5, TCI; Japan) with concentration up to 1M and shaken for 1 hour for quenching process. After shaking, the particles are washed DI water via centrifugation. Finally, modified MNPs were mixed with different amounts of SA (194-17863, Wako Chemicals; Japan). The concentration of SA varied from 0.19 μM to 3.38 μM. The frequency dependence of the AC magnetization spectra in the range of 10-10,000 Hz was analyzed using PPMS at a magnetic field strength amplitude of 0.8 kA/m at 300 K.

5.2 Properties of major MNP clusters and method to form coefficient matrix

Figs. 5-2(a) and (b) depict the AC magnetization spectra and hydrodynamic size distribution of C_0', C_1', C_2' and C_3' used to construct the coefficient matrix Eq. (2-23). Table. 5-1 shows the peak size, standard deviation, and coefficient of variation (CV) of the hydrodynamic size of MNP clusters. As the hydrodynamic size of the MNP cluster increased,

the imaginary part's peak frequency shifted to a lower frequency. The cluster size was determined based on the cluster morphology between biotinylated MNPs and SA, as depicted in Fig. 5-2. C_1 represents, as shown in Fig. 5-2, a layer of SA that was absorbed onto biotinmodified MNPs. It was determined that the increase in hydrodynamic size between C_1 and C_0 is 10 nm, which is twice the size of SA [1]. Thus, the cluster with 49.7 nm was chosen to represent C_1 as C_1'. As for C_2, the hydrodynamic dimension of a cluster formed by two aggregates of MNP–SA is 85 nm along its long axis. Therefore, the MNP cluster with 89.5 nm was chosen to represent C_3 as C_2'. As C_3 is composed of four aggregates of MNP–SA, resulting in a hydrodynamic size of approximately 120 nm, we chose the cluster with a hydrodynamic size of 122.9 nm to represent C_3. Due to the difficulty in measuring the actual hydrodynamic size of MNP clusters, the cluster sizes chosen for this study represent various aggregation status. As shown in Fig. 5-3, there are areas of overlap between C_0', C_1', C_2' and C_3'. In addition, each MNP cluster utilized in the formulation of the experimental model had a similar distribution width with a CV value of 20%, resulting in the inclusion of an additional MNP–SA cluster type (such as that formed by three biotinylated MNPs) in our experimental model. Exactly, larger clusters will be formed by the aggregation of SA and MNPs. To reduce the impact of larger clusters on the analysis, the concentration of SA was restricted to values such that the maximal size of the MNP–SA cluster was less than 100 nm. Consequently, we believed that C_0', C_1', C_2' and C_3' in the experimental model could be used to analyze the AC magnetization spectra of the MNP–SA clusters with peak sizes ranging from 40 nm to 100 nm. As described in **Section** 2.3, the four types of AC magnetization spectra data at different MNPs concentrations (5 mg/mL, 2.5 mg/mL) were used as column vector to form the

coefficient matrix in eq (2-25). For example, the procedure for forming $\boldsymbol{A_{exprimental,i}}$ is shown in Fig. 5-4.

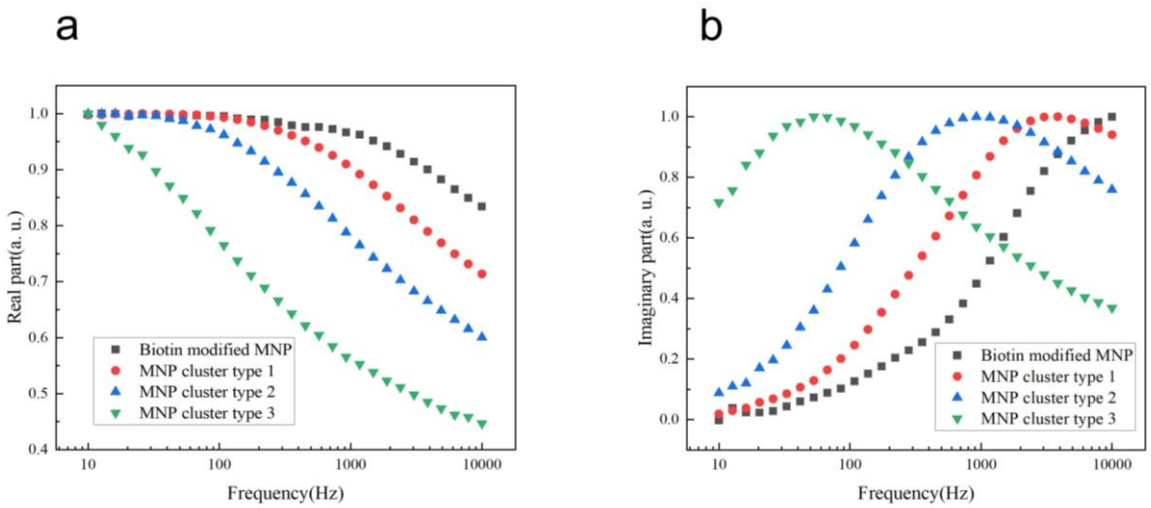

FIG. 5-2. (a) Real part and (b) imaginary part of AC magnetization spectra of MNP clusters used to form coefficient matrix for the experimental model.

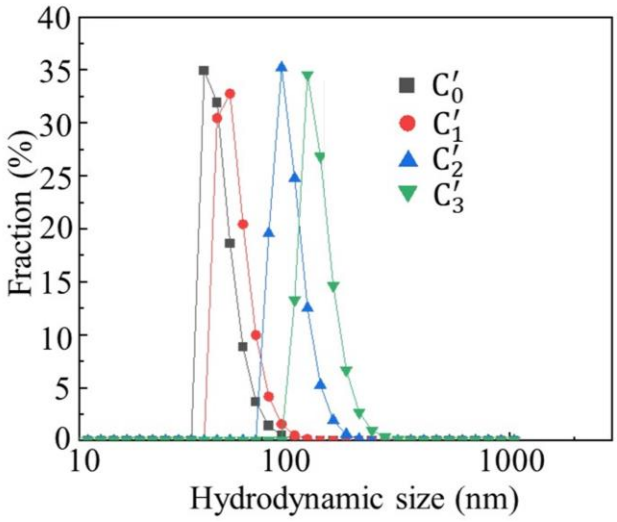

FIG. 5-3. DLS results of MNP clusters used to form coefficient matrix for the experimental model.

Table 5-1. Hydrodynamic size of MNP clusters from DLS measurements.

	Biotin modified MNPs	MNPs cluster type 1	MNPs cluster type 2	MNPs cluster type 3
Hydrodynamic size (nm)	39.5±8.8	49.7±9.5	89.5±16.3	122.9±24.6

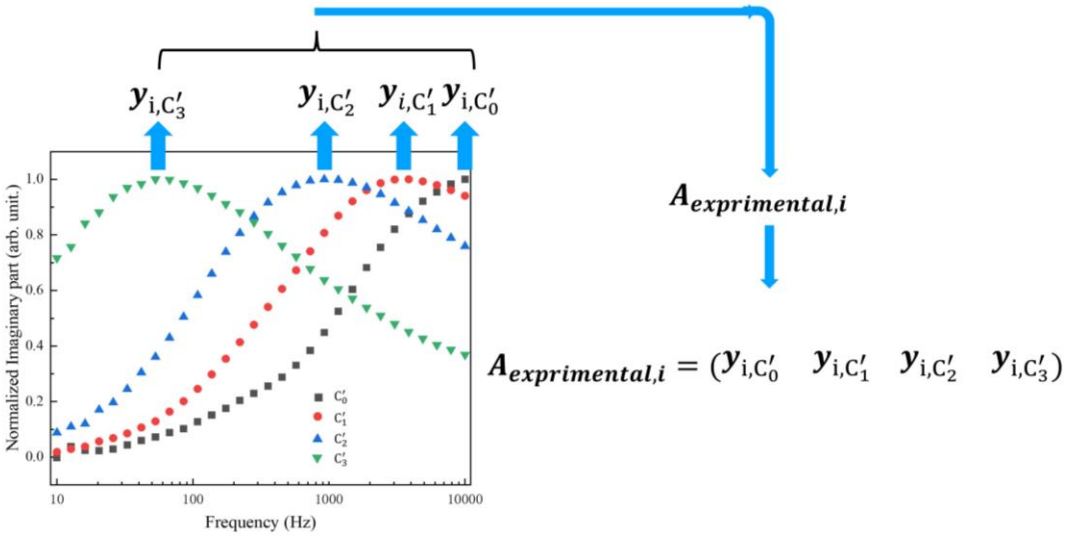

FIG. 5-4. Schematic illustration of the formulation of the coefficient matrix in (2-19) (the imaginary part is used for example).

5.3 Estimation of distribution of MNPs cluster from AC magnetization spectra

After obtaining the coefficient matrix for the experimental model, the estimation of the number distribution of MNP clusters was conducted using the eq (2-19) and (2-27), employing different concentrations of MNPs and SA. The Tikhonov regularization parameter λ for experimental model was optimized by a grid search. At first, 200 values of λ were generated with λ ranging from 10^{-15} to 10^{-1} and evenly spaced logarithmically. Then each

value of λ was used to calculate the $\hat{\boldsymbol{x}}_{\mathbf{exp}}$ on the given data for optimizing λ and then $\boldsymbol{A}_{\mathbf{exp}}$ and $\hat{\boldsymbol{x}}_{\mathbf{exp}}$ are substituted into Eq (2) to reconstruct the AC magnetization spectra. The R^2 score between the reconstructed spectra and the measured spectra was calculated. The λ with the highest average R^2 score on the given data is selected as the optimal value of λ. The results of AC magnetization spectra are shown in Fig. 5-5. For real parts of AC magnetization spectra of the high concentration of MNPs (5mg/mL) as shown in Fig. 5-5(a), the increase in the value with higher concentration of SA (especially when the concentration of SA is equal to 1.88 μM) can be explained by the increase in the dipole-dipole interaction among MNPs caused by the higher aggregation degree among MNPs. Meanwhile, at the low concentration of MNPs (2.5mg/mL), we observed that the real part of AC magnetization spectra exhibits a monotonically decreasing trend when the concentration of SA reaches to 1.88 μM as shown in Fig. 5-5(b). This observation indicates occurrence of Brownian relaxation at lower frequency range with the concentration of SA equal to 1.88 μM, comparing to other concentrations. The results of the imaginary part of AC magnetization spectra are shown in Fig. 5-5 (c) and (d). Both sets of results exhibited a shift in peak frequency from high to low, indicating an increase in Brownian relaxation time. This shift is attributed to the higher proportion of larger MNP-SA clusters formed by the aggregation among MNPs and SA [2]. This observation can be explained by considering the number ratio of MNP clusters to SA [3]. As the concentration of SA increases, the tendency for MNPs to form larger clusters becomes more prominent [4], resulting in larger clusters being formed at the same concentration of SA in the case of the low MNPs concentration.

Fig. 5-6 depicts the results of the estimated distribution of MNP clusters obtained from the experimental model. A comparison of the estimated cluster distribution between different

MNP concentrations is presented in Figure 5 (a) and (b). Notably, the cluster size observed in the suspension with the low MNP concentration was larger than that in the suspension with the high MNP concentration, consistent with the mean hydrodynamic size measured by DLS, as shown in Fig. 5-7. The estimated results of the high MNP concentration exhibited no presence of C_3' in the suspension, even when the concentration of SA reached to 1.88 μM. In contrast, the estimated results for the low concentration of MNPs show the different tendency. The total number-weighted frequency of C_2' and C_3' reached up to about 40% when the concentration of SA reached to 1.88 μM. This observation provides a possible explanation for the significant peak shift depicted in Fig. 5-5(d) and corresponds to the substantial change in mean hydrodynamic size observed between the concentrations of SA of 0.94 μM and 1.88 μM, as illustrated in Fig. 5-7(b). These findings demonstrate that the estimated distributions of MNP clusters are qualitatively consistent with the AC magnetization spectra and the DLS results of the mean hydrodynamic size. Based on the estimated number distribution of clusters $\widehat{\boldsymbol{x}}_{\mathbf{exp}}$and the matrix $\boldsymbol{A}_{\mathbf{exp}}$, we calculated the imaginary parts of the AC magnetization spectra by calculating $\boldsymbol{A}_{\mathbf{exp}}\widehat{\boldsymbol{x}}_{\mathbf{exp}}$, and the results are shown as curves in Fig. 5-5. The calculated imaginary parts were consistent with the experimental data, indicating accurate estimation.

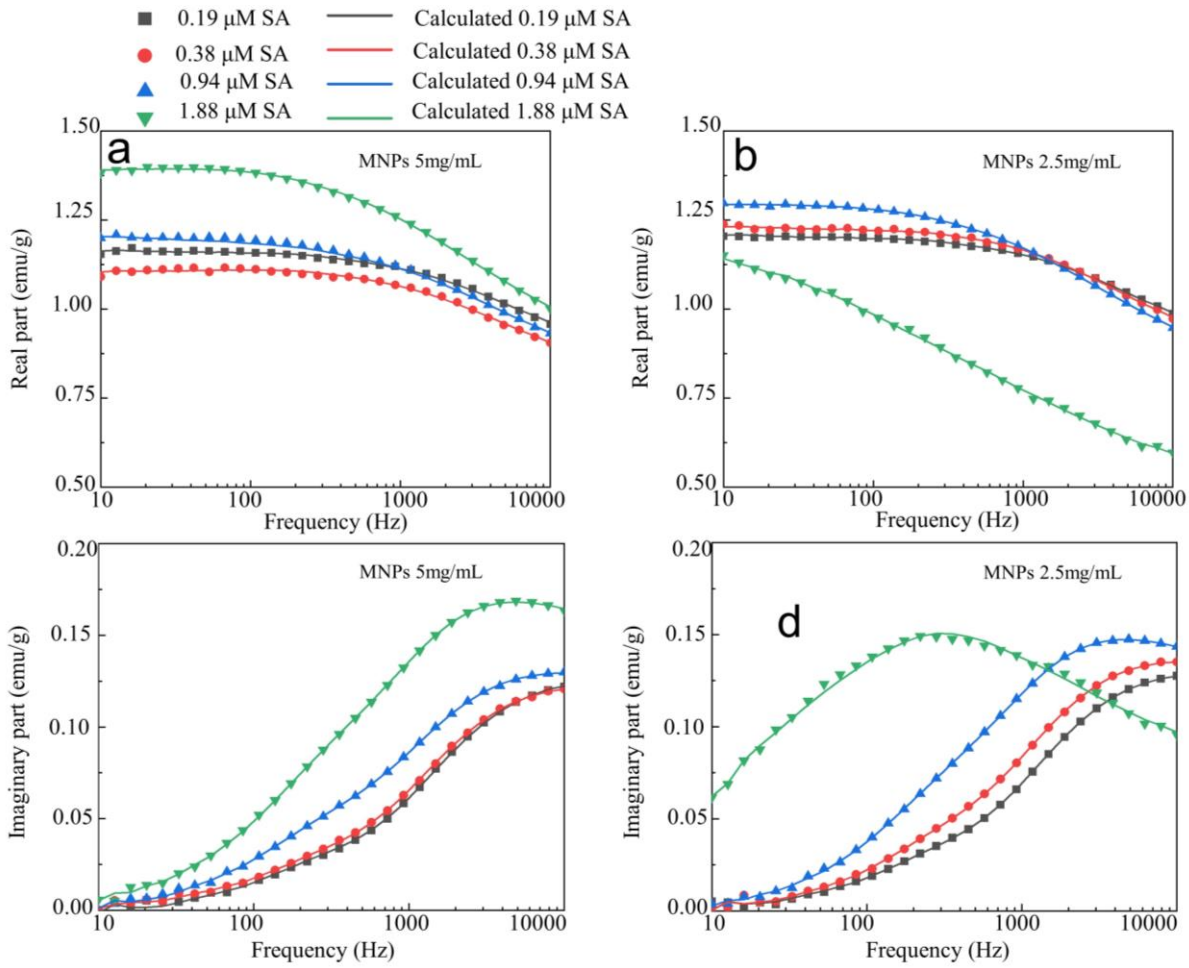

FIG. 5-5. Real parts of AC magnetization spectra with different SA concentrations at biotin modified MNPs concentration of (a) 5mg/mL (b) 2.5mg/mL. Imaginary parts of AC magnetization spectra with different SA concentrations at biotin modified MNPs concentration of (c) 5mg/mL (d) 2.5mg/mL. The scatters represent the measured experimental spectra, and the lines represent the calculated spectra based on the estimated number distribution of clusters $\widehat{\boldsymbol{x}}_{\mathbf{exp}}$ and the matrix $\boldsymbol{A}_{\mathbf{exp}}$.

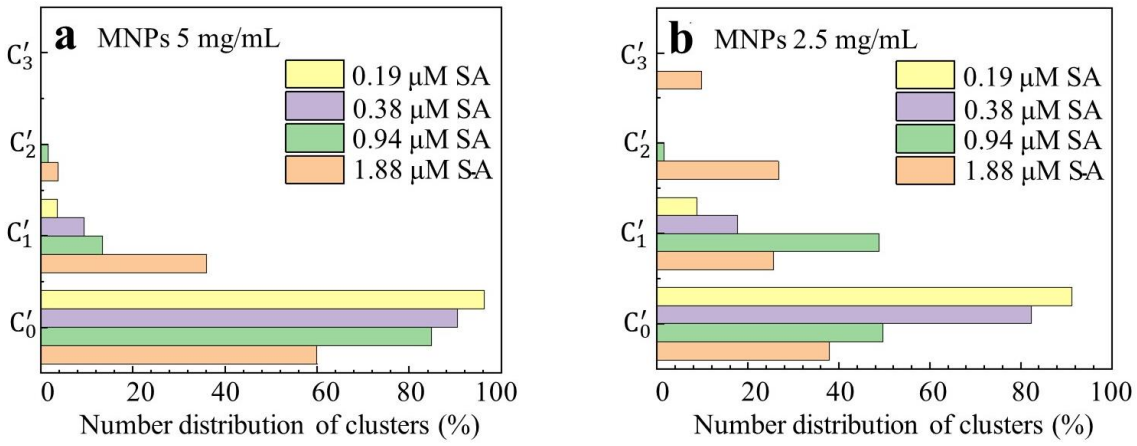

FIG. 5-6. Estimated hydrodynamic size from experimental model with different SA concentrations at biotin modified MNPs concentration of (a) 5 mg/mL (b) 2.5 mg/mL.

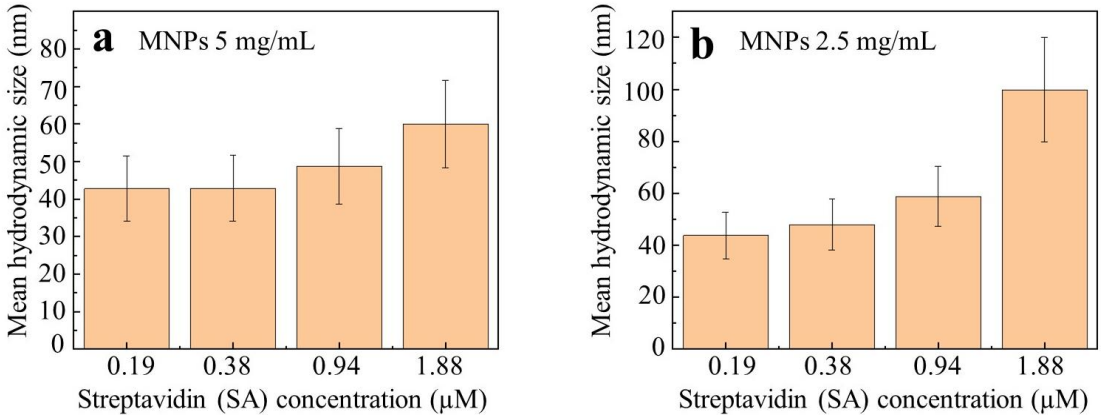

FIG. 5-7. Mean hydrodynamic size measured by DLS with different SA concentrations at biotin modified MNPs concentration of (a) 5 mg/mL (b) 2.5 mg/mL.

5.4 Demonstration of streptavidin detection

In **Section** 5-3, the qualitative analysis was done. In this section, we discuss the demonstration of the quantitative detection of SA. In the previous research [2], Zhong et al. showed that with the increase in biomolecules, more MNPs were cross-linked to each other

to form larger clusters as shown in Fig. 5-8. Based on their results, we assumed that the number of MNP clusters with different hydrodynamic sizes corresponded to the amount of SA bound to MNP clusters. Thus, we established a linear model to quantitively detect the concentration of SA as follows:

$$n_{SA} = \sum_{i=1}^{K} a_{d_{h,i}} n_{d_{h,i}}, \qquad (5-1)$$

where n_{SA} is the number of SA in the suspension, $a_{d_{h,i}}$ is the number of SA bound to MNP clusters with size $d_{h,i}$, and $n_{d_{h,i}}$ is the number of MNP clusters with hydrodynamic size $d_{h,i}$.

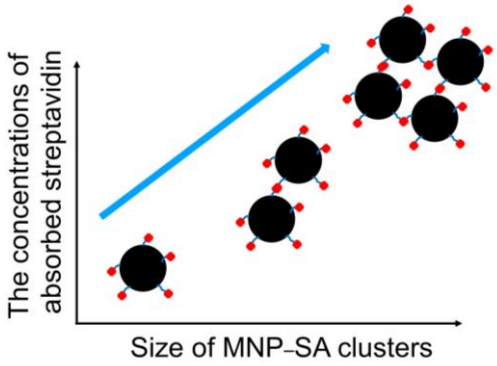

FIG. 5-8. Schematic illustration of the relationship between the concentrations of absorbed SA and the size of MNP–SA clusters.

We utilized the estimated number of MNP clusters $n_{d_{h,i}}$ analyzed from AC magnetization spectra, along with the calculated number of SA molecules derived from the concentration range of 0.19 μM to 3.38 μM. These values were employed to train a linear regression model with positive coefficients and no intercept. The training and test dataset were split randomly from the whole dataset of $n_{d_{h,i}}$ and n_{SA} including all the experimental data. After obtaining

$a_{d_{h,i}}$, the estimated concentration of SA was calculated using Eq (5-1) for both training and test dataset. Then the R^2 score between the true concentration of SA and the estimated concentration of SA, and the results are shown in the Fig. 5-9. Remarkably, the trained model exhibits excellent predictive capability for the concentration of SA, as evidenced by a high R^2 score of 0.962 for the test data. Thus, the results indicate the potential application of the estimated distribution of MNP clusters in detecting the concentration of SA. Furthermore, the average R^2 score between the estimated values and true values of the concentration of SA, along with the corresponding standard deviation, are calculated for MNPs at different concentrations for a series of SA concentrations (0.19 μM, 0.235 μM, 0.38 μM, 0.94 μM), as presented in Table 5-2. Notably, the low concentration of MNPs (2.5 mg/mL) exhibits a higher R^2 score with a lower standard deviation, suggesting that the concentration of MNPs plays a crucial role in the proposed biosensing method. These findings indicate that a lower concentration of MNPs can lead to enhanced sensitivity in the lower SA range.

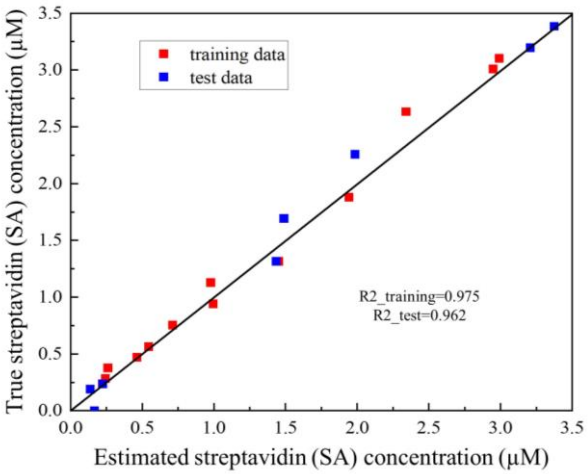

FIG. 5-9. The relationship between true SA concentration and estimated SA concentration using the proposed method.

Table 5-2. The average R^2 score for MNPs at different SA concentrations (0.19 μM, 0.235 μM, 0.38 μM, 0.94 μM).

	Concentration of MNPs at 5mg/mL	Concentration of MNPs at 2.5mg/mL
Average R^2 score	0.887	0.920
Standard deviation of R^2 score	0.007	0.009

5.5 Effect of MNP clusters

In the previous section, we demonstrated the feasibility of the proposed method for detecting SA. However, an issue remained unresolved regarding the freedom of the selection of MNP cluster for forming the coefficient matrix in eq (2-25). In this section, we will discuss the selection of MNP clusters. As mentioned in **Section** 5.2, it is crucial to cover the range of the hydrodynamic sizes of MNP-SA clusters when choosing MNP clusters. Therefore, we will reduce the number of MNP clusters to investigate the effect when the range of hydrodynamic sizes cannot be covered.

The distributions of hydrodynamic size of MNP clusters after removing C_2' and C_3' in Figs. 5-10(a) and (b), respectively. In Fig. 5-10(a), it can be observed that if C_3' is removed, the range of MNP-SA clusters with hydrodynamic sizes larger than the peak size beyond approximately 120nm cannot be covered. Similarly, in Fig. 5-10(b), we found that removing C_2' renders the experimental model unable to cover the range of MNP-SA clusters with peak sizes between about 80nm and 120nm.

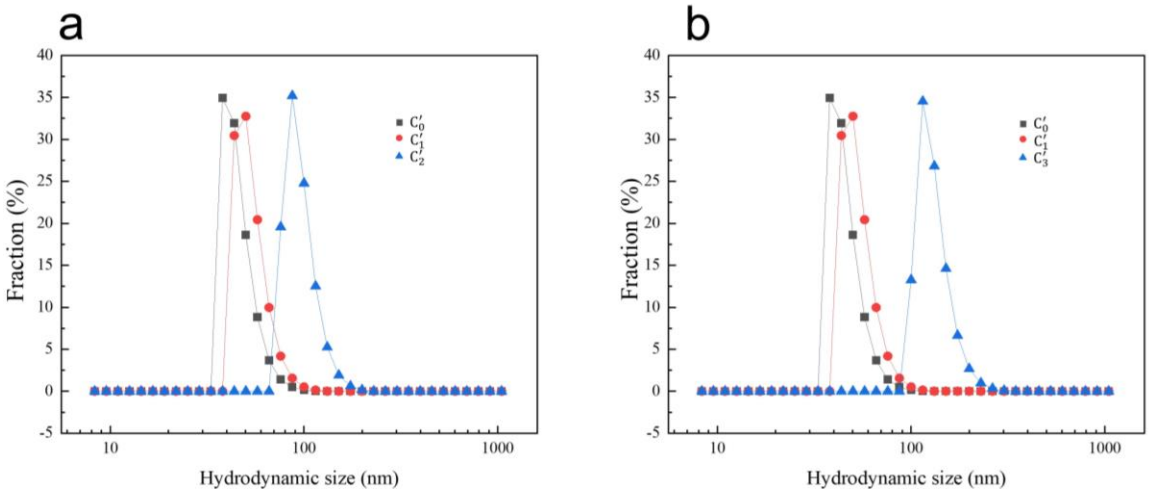

FIG. 5-10. DLS results of MNP clusters used to form coefficient matrix for the experimental model; (a) C_0', C_1' and C_2'; (b) C_0', C_1' and C_3'.

Subsequently, we formed the coefficient matrices of the experimental model by using C_0', C_1', C_2' or C_0', C_1' C_3', and call them as 3-MNP-clusters-no-C_3' and 3-MNP-clusters-no-C_2', respectively. Then the AC magnetization spectra as shown in Fig. 5-5(b) and (d) were analyzed by using the formed coefficient matrices. The estimated results of distributions of MNP clusters with the concentration of MNPs equal to 2.5 mg/mL are shown in the Fig. 5-11. Firstly, when the concentrations of SA are low (0.19 μM, 0.38 μM), as shown in Figs. 5-11(a) and (b), we observed that even when C_3' or C_2' is removed, the estimated results remain almost unchanged. This is because the contributions from C_2' and C_3' in the results as shown in Fig. 5-6(b) are already negligible and, therefore, there was no significant effect. This observation indicates that as long as the proportion of larger MNP-SA clusters (such as C_2 and C_3) in the suspension is low, the absence of larger clusters in the coefficient matrix does not affect the results. In contrast, when the suspension contains components that were

included in the coefficient matrix, as observed in the results in Figs. 5-11(c) and (d), significant difference in the estimated results occurred. As depicted in Fig. 5-11(c), comparing the results of 3-MNP-clusters-no-C_2' and 4-MNP-clusters, a certain degree of difference in the estimation is evident. In Fig. 5-11(d), the difference was even more pronounced. For instance, when comparing the results with 3-MNP-clusters-no-C_3' and 4-MNP-clusters, the absence of C_3' in the results of 3-MNP-clusters-no-C_3' led to higher proportions of C_0' and C_1' compared to the results of 4-MNP-clusters. This shift in the overall distribution of clusters towards smaller hydrodynamic sizes also affected the results of SA detection, as shown in Fig. 5-12. As depicted in Fig. 5-12(a), the absence of C_3' led to larger difference in estimation when the concentration of SA is high. Similarly, as shown in Fig. 5-12(b), the absence of C_2' not only resulted in deviations at higher SA concentrations but also lowered the overall R^2 score. These results demonstrated the necessity of selecting appropriate MNP clusters to cover the range of hydrodynamic sizes of MNP-SA clusters. Moreover, when the suspension does not contain a significant proportion of larger MNP-SA clusters, the absence of corresponding components in the coefficient matrix does not have a significant effect on the results.

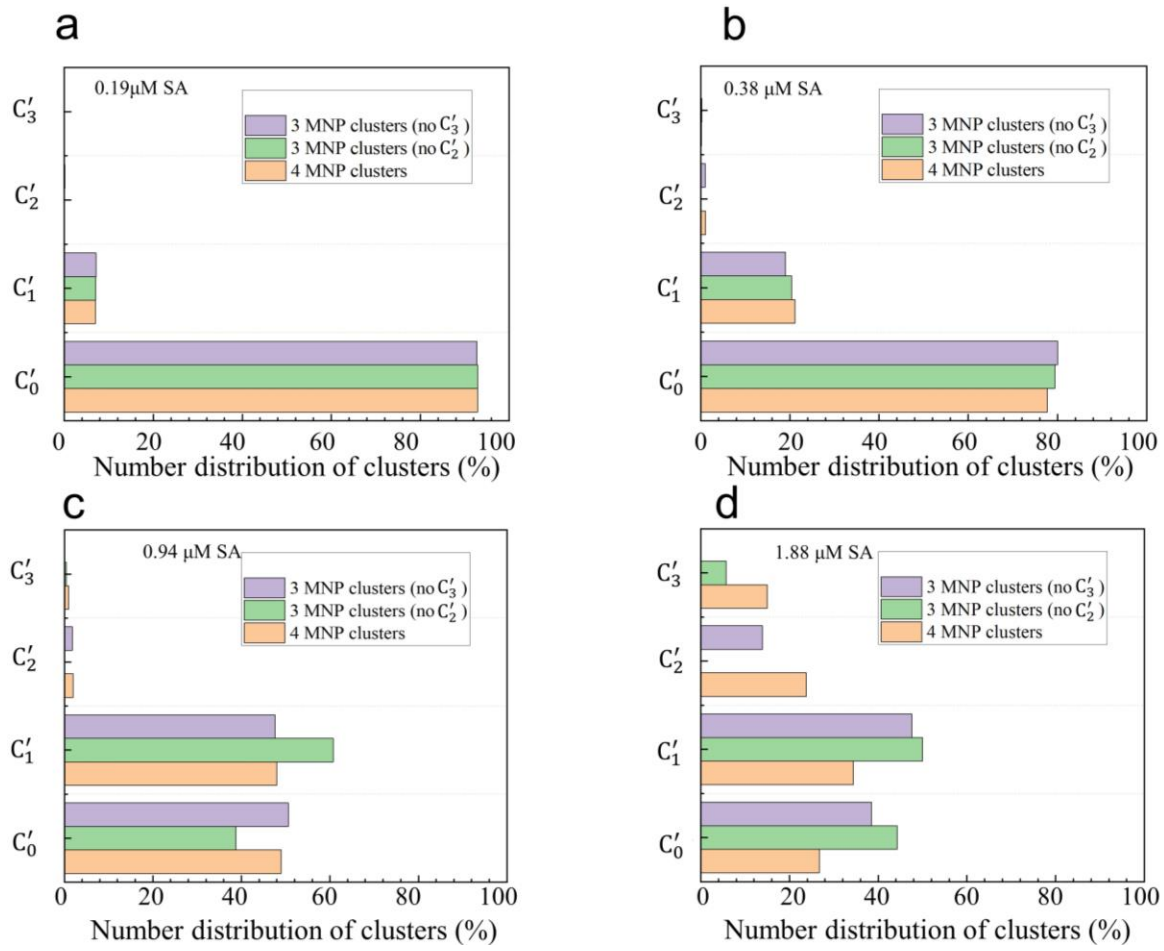

FIG. 5-11. Estimated hydrodynamic size from experimental model with different SA concentrations at (a) 0.19 μM , (b) 0.38 μM (c) 0.94 μM and (d) 1.88 μM with the concentration of MNPs equal to 2.5mg/mL.

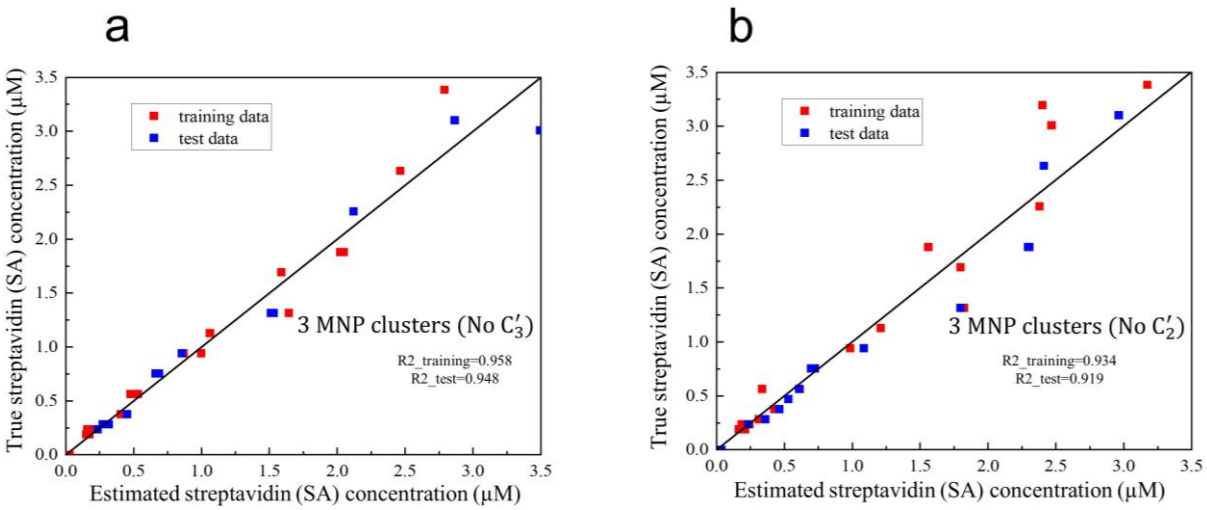

FIG. 5-12. The relationship between true SA concentration and estimated SA concentration using the proposed method with (a) 3 MNP clusters (no C_3') and (b) 3 MNP clusters (no C_2').

5.6 Comparison with estimation results from imaginary part

Due to the more intuitive representation of relaxation frequencies provided by the imaginary part, the imaginary part results have been more widely utilized in previous studies for the detection of biomolecules. In this section, the distributions of MNP clusters obtained from the imaginary part of AC magnetization spectra as shown in Fig. 5-5(d) are depicted in Fig. 5-13(b) and compared with the results obtained from the whole AC magnetization spectra as shown in Fig. 5-13(a). Note that Fig. 5-13(a) shows the same results that are shown in Fig. 5-6(b). As shown in Figure 5-13, we found that the two estimated results exhibit a similar tendency consistent with the DLS results as shown in Fig. 5-7, indicating that it is also possible to analyze the AC magnetization spectra by only using the imaginary part for estimating the distributions of MNP clusters. This observation aligned with the findings in

Section 3.4, indicating that the real part does not provide additional information about the distributions of MNP clusters beyond what the imaginary part offers.

Next, following the method described in **Section** 5.4, we trained a linear regression model using the obtained distributions of MNP clusters and the true concentration of SA to estimate the concentration of SA in the suspension. The relationship between the true concentration and the estimated concentration of SA is shown in Fig. 5-14. As depicted in Fig. 5-14, the estimated concentration closely aligned with the true concentration and exhibits a high R^2 score. Moreover, when compared to the results presented in Fig. 5-9, estimated results obtained by only using the imaginary part yielded a higher R^2 score. Similarly, Table. 5-3 demonstrates similar findings, where employing only the imaginary part for estimation results in the improved R^2 score for both low and high concentrations of MNPs, compared to Table 5-2. According to the discussion in the **Section** 3.4, there is no significant difference in the estimated distribution whether the real part of AC magnetization spectra is used or not. After analyzing the AC magnetization spectra as shown in Fig. 5-5, we found that there are some noises in the lower frequency range (10-80Hz) in the real part caused by the sensitivity of PPMS at lower frequency range, which might influence the estimated distributions of MNP clusters. To lower the influence of the noises, the noisy sampling points in the lower frequency range (10-80Hz) were removed, then the estimation was performed. The new results after removing the noisy sampling points are shown in the Table 5-4. From the results, we found that there is no significant difference between the R^2 score of results obtained from both the real and imaginary part and that from the imaginary part.

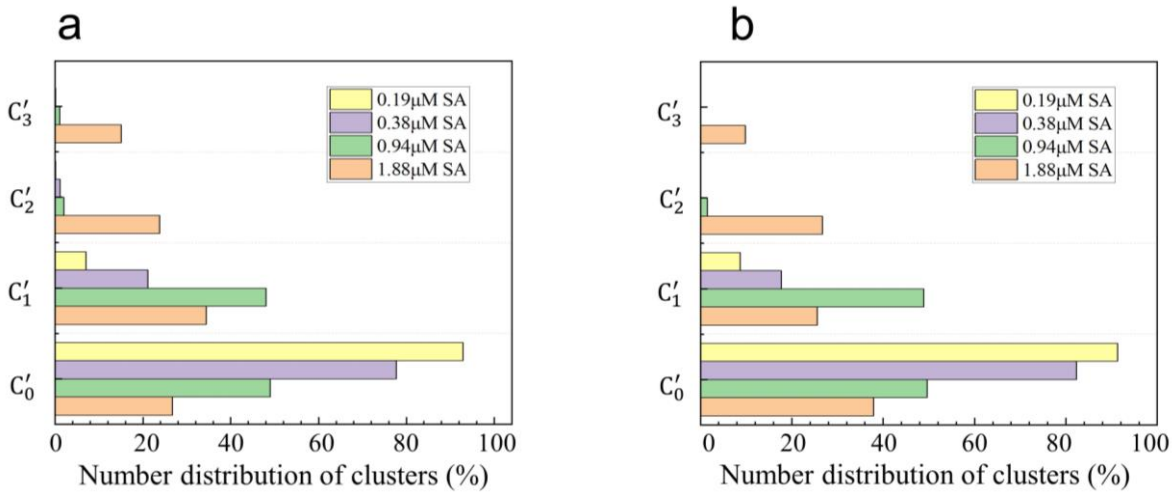

FIG. 5-13. Estimated hydrodynamic size from experimental model with different SA concentrations at biotin modified MNPs concentration of 2.5 mg/mL from (a) the real part and the imaginary part ,and (b) the imaginary part of AC magnetization spectra.

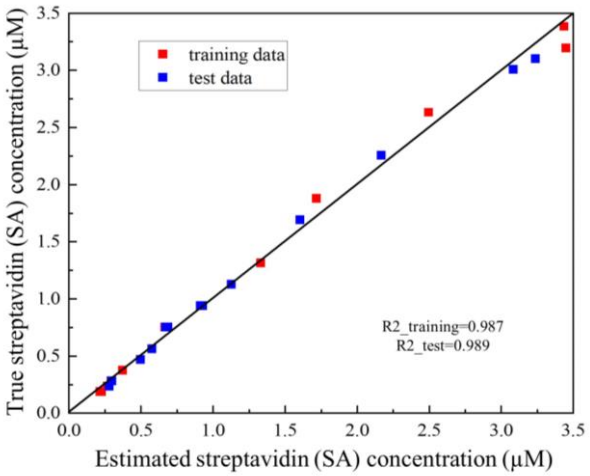

FIG. 5-14. The relationship between true SA concentration and estimated SA concentration from the imaginary part of AC magnetization spectra by using the proposed method.

Table 5-3. The average R^2 score for MNPs at different concentrations using the imaginary part of AC magnetization spectra.

	Concentration of MNPs at 5mg/mL	Concentration of MNPs at 2.5mg/mL
Average R^2 score	0.967	0.990
Standard deviation of R^2 score	0.006	0.002

Table 5-4. The comparison of R^2 score of results before and after removing the sampling points at low frequency range (10Hz to 80 Hz) of the real part of AC magnetization spectra.

	Concentration of MNPs at 5mg/mL	Concentration of MNPs at 2.5mg/mL
Before removing	0.962	0.989
After removing	0.979	0.984

5.7 Results of streptavidin detection using relaxation frequency based method

In this section, we will compare the proposed method with the relaxation frequency based method in terms of the detection of SA. For the relaxation frequency-based method, we first extracted the relaxation frequency from the imaginary part. Since the relaxation frequencies of some of the data in this experiment do not fall within the range of 10-10000 Hz, we only selected the data where the relaxation frequency is identifiable. We then calculated the relaxation time based on the obtained relaxation frequency by $\tau = \frac{1}{2\pi f_{relaxation}}$ and plot it against the SA concentration, as shown in Figure 5-15(a). It is important to note that we only show the results with the concentration of MNPs equal to 5 mg/mL. From this experimental data, we observed that at relatively lower concentrations of SA (1.32 μM ~ 2.25 μM), the

relaxation time increases gradually. As the concentration of SA is higher than 2.25 μM, the relaxation time shows a rapid increase, consistent with the finding of previous research [4].

In the previous study, researchers used the so-called logistic function [5,6] to describe the relationship between the relaxation time and SA concentration. The logistic function is given by,

$$Relaxation\ time = \frac{A' - B'}{1 + \left(\frac{m}{m_0}\right)^p} + B' \qquad (5-2)$$

where A', B', m_0, p are fitting parameters, and m is the true concentration of SA. Here, we employed the logistic function to fit the data in Fig.5-15(a), and the fitted curve is represented by the red curve in Fig. 5-15(a). We found that the logistic function can reasonably capture the trend in the latter half (the concentration of SA > 2.25 μM) but does not adequately explain the relatively unchanged trend in the first half. Subsequently, using the fitted data, we plotted Fig. 5-15(b). From Fig. 5-15(b), we observed a reduction in the number of data points comparing to Fig. 5-15(a). This is because, for relaxation times below a certain threshold, the corresponding SA concentration values cannot be found on the fitted curve. Similar to Fig. 5-15(a), Fig. 5-15(b) demonstrated good estimation for higher concentrations of SA. However, for lower concentrations, it was difficult to estimate. This is the limitation of the relaxation frequency based method, as it struggles to accurately estimate at lower concentrations of SA. In contrast, our proposed method overcame this limitation. In Fig. 5-16, we show the results for the same SA concentration range and the concentration of MNP equal to 5 mg/mL. We observed that our proposed method performs well in estimating concentrations of SA not only in the higher concentration range but also in the lower concentration range.

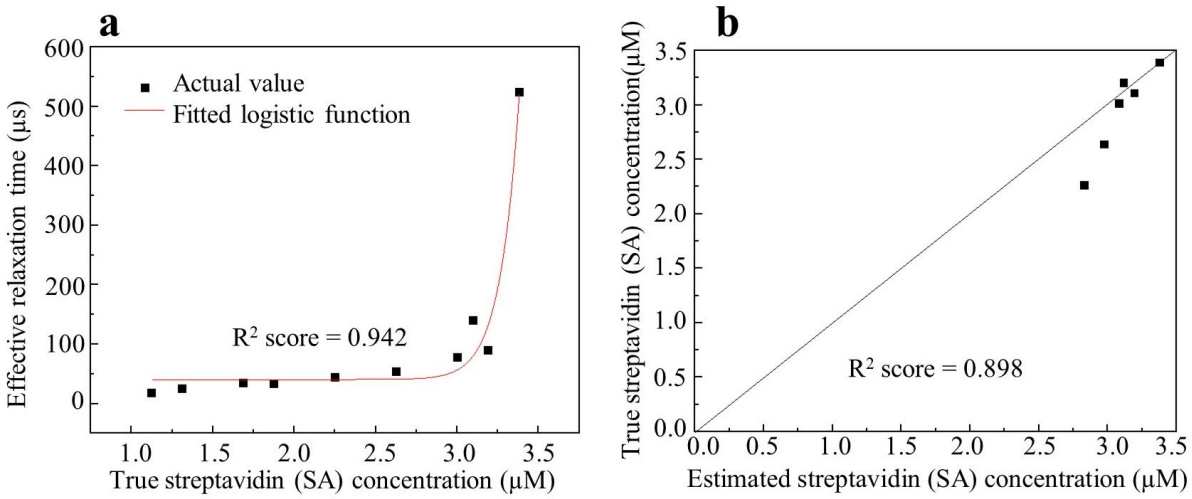

FIG. 5-15. (a) The relationship between the effective relaxation time of MNP clusters and the concentration of SA from effective relaxation frequency, (b) the relationship between the true concentration of SA and estimated SA concentration using the relationship in Fig. 5-15(a) (the concentration of MNPs is 5mg/mL).

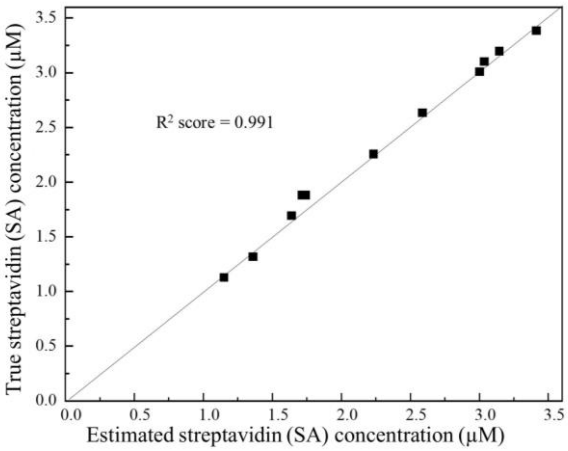

FIG. 5-16. The relationship between the true concentration of SA and estimated SA concentration using the proposed method (the concentration of MNPs is 5mg/mL and the data of true concentration of SA lower than 1.3 μM is not included).

Table 5-5. Summary of fitting parameters used in Fig. 5-15(a)

A'	B'	m_0	p
40.22	1346887.91	4.47	28.50

5.8 Discussion of magnetic interactions

As described in **Section** 2.3, we assumed that interaction among MNPs inside clusters should be considered, but interaction among clusters is negligible. To support our assumption, some experiments have been done.

We used Debye relaxation model as described in **Sections** 2.1 and 2.2 to estimate the distribution of MNP clusters, and the estimated distribution was used to estimate the amount of SA by method as described in **Section** 5.4. The estimated results of SA are shown in Fig. 5-17. Comparing to the results obtained by the proposed method as shown in Fig. 5-9, R^2 score of the estimated concentration of SA by the proposed method on both training and test data was higher than that by the Debye relaxation model, indicating that it is reasonable to consider the interaction between MNPs inside clusters.

To experimentally prove that the interaction among MNP clusters can be negligible, three types of MNP clusters A, B and C with AC magnetization spectra as shown in Fig. 5-18 (a) were used. We mixed the clusters A, B and C with different ratios and their AC magnetization spectra of mixed suspension were measured as shown in Fig. 5-18 (b). Then, the proposed method as described in **Sections** 5.2 and 5.3 by using AC magnetization spectra as shown in Fig. 5-18 (a) to form coefficient matrix was used to estimate the ratio of the clusters A, B and C. The estimated results are shown in Table 5.5. If the interaction among the clusters is strong, aggregation among the clusters should occur, leading to inaccurate estimation. However,

from the results, the estimated ratios correspond to the true ratios well, indicating that the interaction among the clusters is negligible. In summary, our assumption is reasonable according to the results of experiments.

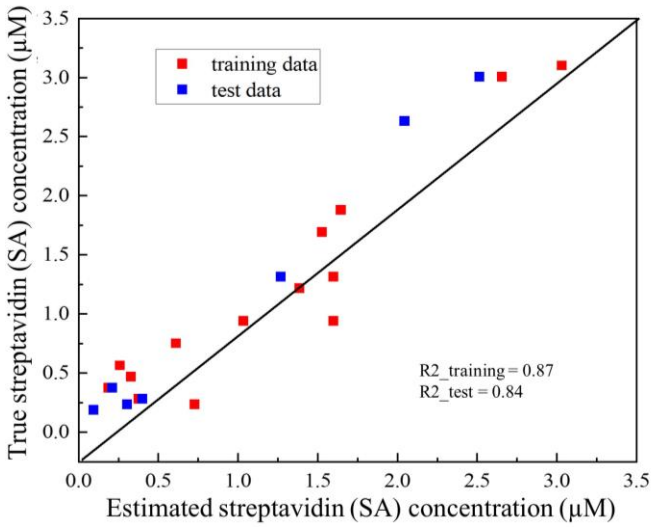

FIG. 5-17. The relationship between true SA concentration and estimated SA concentration from the imaginary part of AC magnetization spectra by Debye relaxation model.

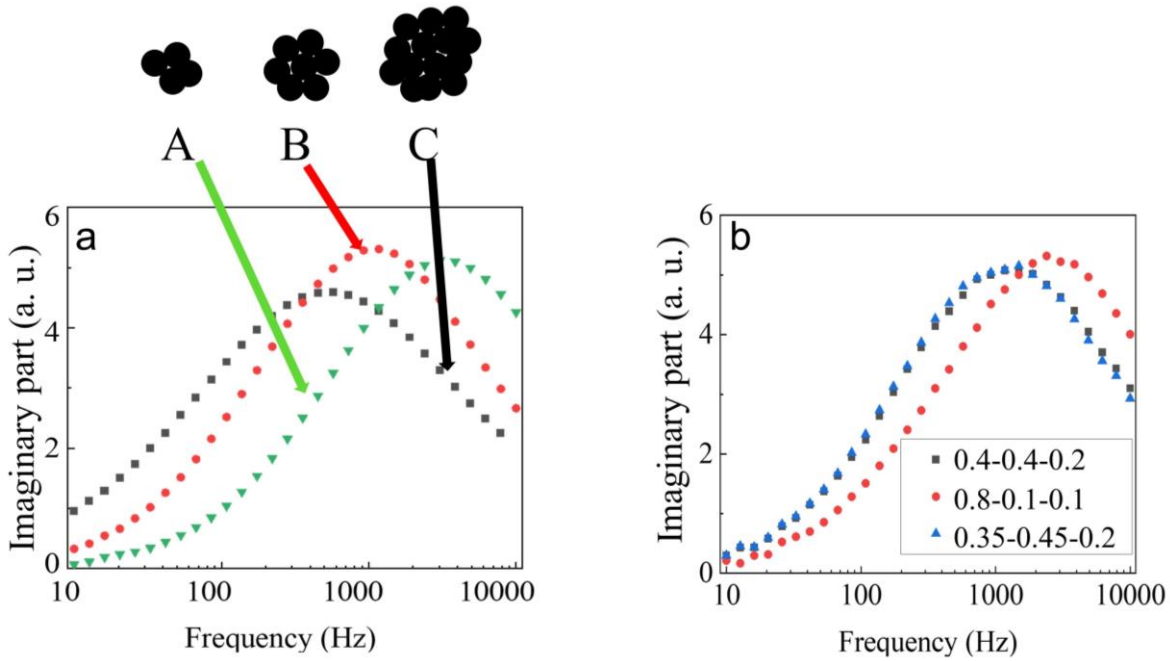

FIG. 5-18. (a) AC magnetization spectra of MNP clusters A, B and C (Hydrodynamic size: 57.7±7.4, 79.7±8.7, 109.5±14.3 nm), (b) AC magnetization spectra of mixed MNP clusters with different ratios.

Table 5-6. True ratio and Estimated ratio of mixed MNP clusters suspension.

True ratio	Estimated ratio
0.2-0.4-0.4	0.21-0.40-0.39
0.2-0.45-0.35	0.20-0.44-0.36
0.1-0.1-0.8	0.11-0.08-0.81

5.9 Summary

An experimental model was established by the AC magnetization spectra of MNP clusters. The selected MNP clusters were used for presenting the aggregation status of the clusters formed by MNPs and SA. The experimental model was used for estimating the hydrodynamic size distribution of MNP clusters from AC magnetization spectra of mixture

of biotinylated MNPs and SA. The estimated distributions were consistent with the hydrodynamic results measured by DLS measurements. The estimated distributions and the true concentration of SA were used for establishing a linear model. The estimated the concentration of SA by the established linear model was highly consistent with the true concentration of SA by using the R^2 score. In addition, we confirmed the low concentration (2.5mg/mL) showed a higher R^2 score with lower standard deviation. Moreover, the effect of MNP clusters used for establishing the experimental model was investigated. From the results, we confirmed the necessity of selecting appropriate MNP clusters to cover the range of hydrodynamic sizes of MNP-SA clusters. Finally, the results of the proposed method were compared with the results of the relaxation frequency based method. From the comparison, the proposed method showed both wider detection range and the high R^2 score than the relaxation frequency based method.

5.10 Reference

[1] R.A. Sperling, W.J. Parak, Surface modification, functionalization and bioconjugation of colloidal Inorganic nanoparticles, Philos. Trans. R. Soc. Math. Phys. Eng. Sci. 368 (2010) 1333–1383. https://doi.org/10.1098/rsta.2009.0273.

[2] J. Zhong, M. Schilling, F. Ludwig, Magnetic nanoparticle-based biomolecule imaging with a scanning magnetic particle spectrometer, Nanotechnology. 31 (2020). https://doi.org/10.1088/1361-6528/ab776a.

[3] J. Dieckhoff, A. Lak, M. Schilling, F. Ludwig, Protein detection with magnetic nanoparticles in a rotating magnetic field, J. Appl. Phys. 115 (2014) 024701. https://doi.org/10.1063/1.4861032.

[4] C.C. Yang, S.Y. Yang, H.H. Chen, W.L. Weng, H.E. Horng, J.J. Chieh, C.Y. Hong, H.C. Yang, Effect of molecule-particle binding on the reduction in the mixed-frequency alternating current magnetic susceptibility of magnetic bio-reagents, J. Appl. Phys. 112 (2012). https://doi.org/10.1063/1.4739735.

[5] A. Tsoularis, J. Wallace, Analysis of logistic growth models, n.d. www.elsevier.com/locate/mbs.

[6] M. Uchymiak, E. Lyster, J. Glater, Y. Cohen, Kinetics of gypsum crystal growth on a reverse osmosis membrane, J. Membr. Sci. 314 (2008) 163–172. https://doi.org/10.1016/j.memsci.2008.01.041.

6 Analysis of AC magnetization spectra with fewer frequency points

In the relaxation frequency based method, it is necessary to measure a sufficient number of points from the AC magnetization spectra to identify the relaxation frequency [1,2]. This requirement leads to longer measurement times and lower time efficiency of detection. To address this issue, a straightforward solution is to reduce the number of frequency points needed in the measurement. In this section, we investigate the possibility of using our proposed method to analyze AC magnetization spectra with fewer frequency points (reduced AC magnetization spectra). We begin by investigating the proposed method with simulation data and then discuss its feasibility with experimental data.

6.1 Analysis of simulation data with fewer frequency points

In order to generate simulation data, we followed the same approach as described in **Section** 3.1. Here, we used four different values of μ (3.8, 4.2, 4.8, and 5.5) to represent four different sizes of MNPs, while keeping σ fixed at 0.2. By substituting these μ and σ values into Eq (3-1), we obtained different distributions. Then, based on the obtained distributions, we calculated the AC magnetization spectra using the Debye relaxation model. The resulting spectra are shown in Fig. 6-1. From Fig. 6-1(b), it can be observed that as the μ value increases (indicating larger particle sizes), the peak of the imaginary part shifts towards the lower frequency range.

After generating the AC magnetization spectra, we employed two strategies to reduce the number of frequency points. The first strategy involved selecting one point out of every few points and discarding the rest. For example, if the original frequency sequence is

(1,2,3,4,5,6,7,8,9,10), selecting one point out of every three points would result in (1,4,7,10). This strategy is illustrated in Fig. 6-2(a). Fig. 6-2(b) and (c) show how the spectra in Fig. 6-1(a) and 6-1(b) would look like under the "select one point out of every three" strategy. The advantage of this strategy is that the overall shape of the spectra is preserved, to some extent. However, the higher noise level in of coil-based measurements might influence the results especially in the lower frequency range because of the measurement is based on the Faraday's law.

The second strategy involved selecting a specific range of frequencies and keeping only a subset of points within that range. For example, as shown in Fig. 6-3, we selected 10 points within the range of 100-1000 Hz. The advantage of this strategy is that it allows us to choose a segment with the highest instrument sensitivity for measurement, thereby reducing errors. However, the downside is that the shape of the spectra becomes incomplete, which may have an impact on subsequent estimation processes.

After applying the proposed method to the spectra generated using these two strategies with fewer frequency points, we calculated the R^2 score between the estimated distributions and the original true distribution.

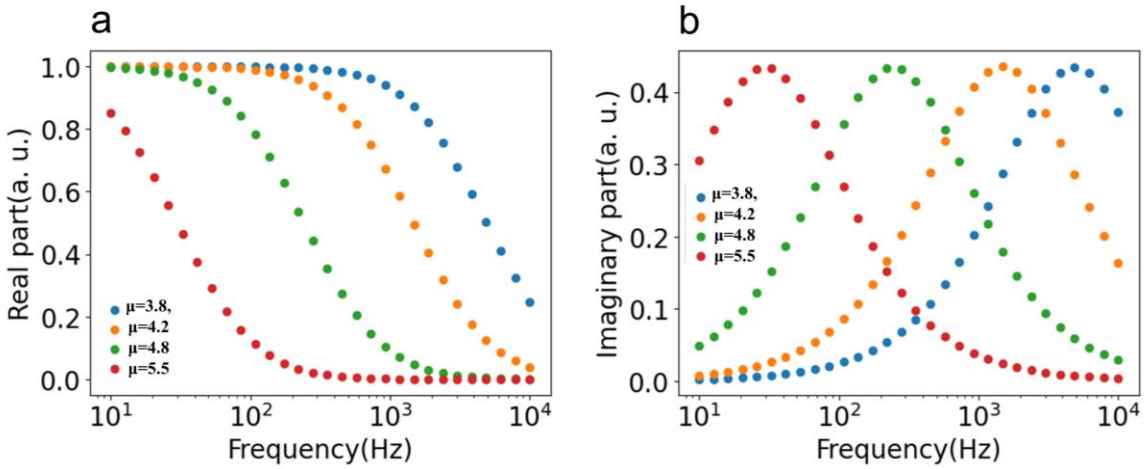

FIG. 6-1. (a) Real part and (b) imaginary part of AC magnetization spectra calculated from MNPs following the lognormal distribution with various μ (3.8, 4.2, 4.8 and 5.5) and the fixed σ equal to 0.2.

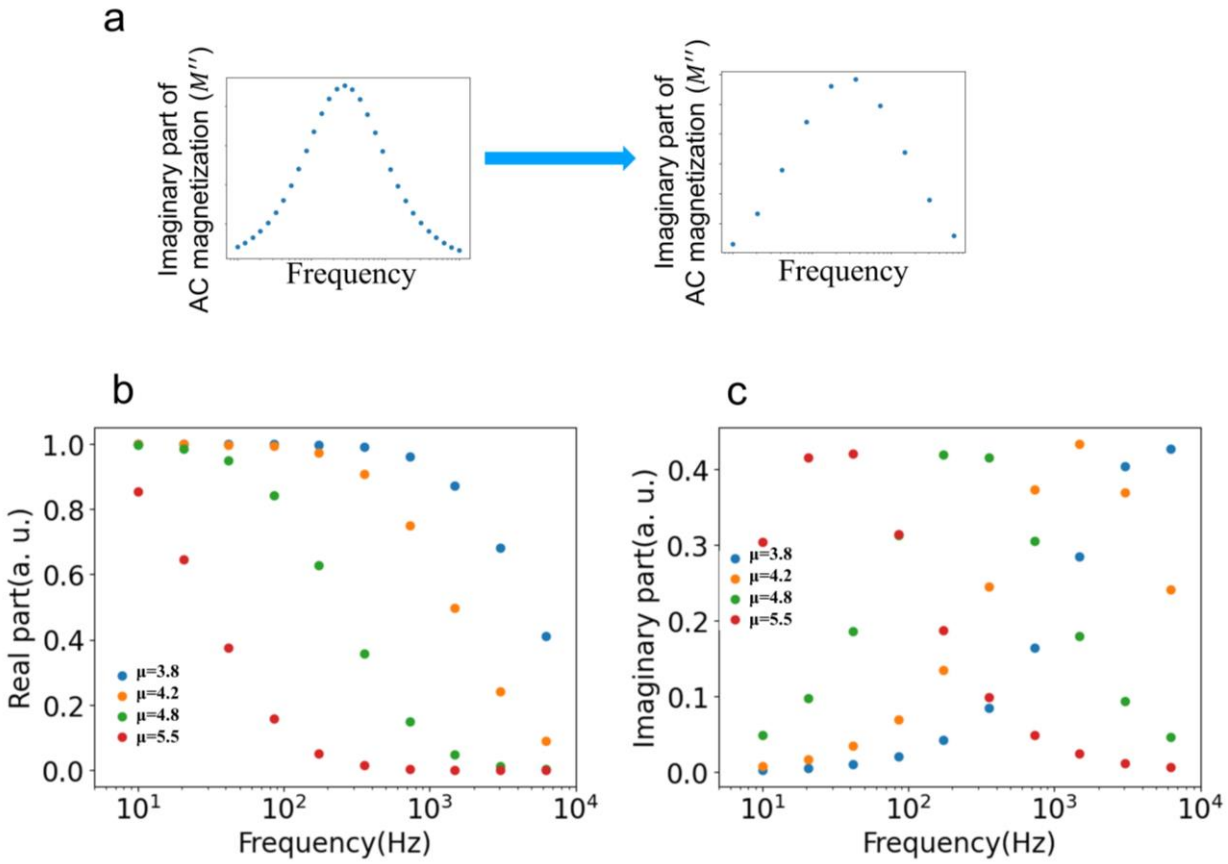

FIG. 6-2. Reduced (a) real part and (b) imaginary part of AC magnetization spectra as shown in Fig. 6-1 by the first strategy.

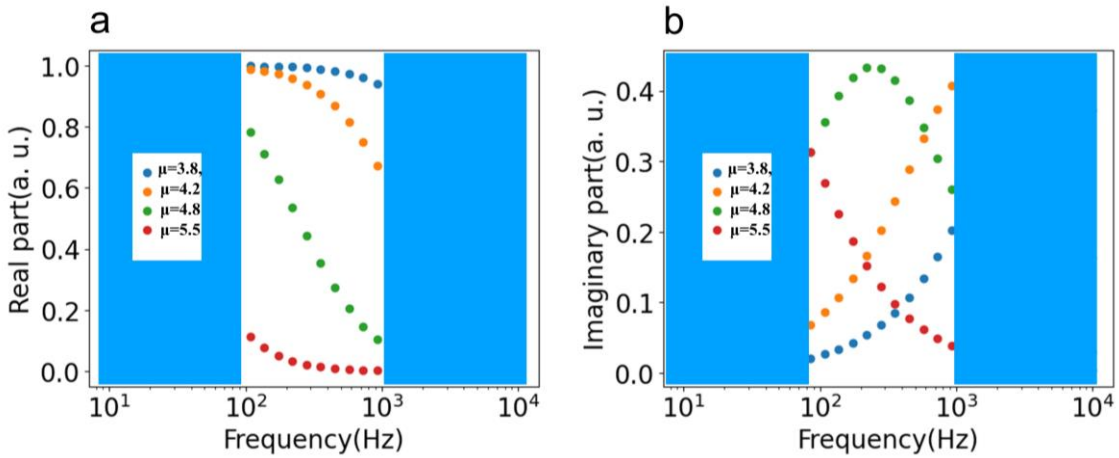

FIG. 6-3. Reduced (a) real part and (b) imaginary part of AC magnetization spectra as shown in Fig. 6-1 by the second strategy.

We first applied our proposed method to the reduced spectra generated using the first strategy, for example, the spectra as shown in Figs. 6-2(b) and (c), and the results are plotted in Fig. 6-4. Each subplot in Fig. 6-4 represents the relationship between the R^2 score and the number of frequency points for each μ(MNP size). The R^2 score between the estimated distribution and the true distribution of MNPs was used. Overall, the R^2 score remained high when the number of frequency points was around 10 or more. However, a significant drop in the R^2 score was observed when the number of points was reduced to five or fewer. This decline in the R^2 score can be attributed to the fact that the reduced spectra with a small number of points do not contain enough information to accurately reconstruct the original spectra, resulting in a larger discrepancy between the estimated and true distributions.

Next, we applied the proposed method to the reduced spectra generated using the second strategy, as depicted in Fig. 6-3, and summarized the results in Table 6-1. From the obtained results in Table 6-1, it can be observed that regardless of the selected frequency range, there

are at least two distributions that could not be accurately estimated. As mentioned earlier, this strategy leads to an incomplete representation of the spectra, making it challenging to achieve accurate estimation if there is insufficient information available within that specific frequency range.

Considering practical applications, particularly in biomolecule detection based on Brownian relaxation, the relaxation frequency undergoes significant variations with changes in the distributions of MNP clusters. Hence, it is difficult to find a narrow frequency range that can capture the entire spectrum's variability. Therefore, in the subsequent analysis of experimental data, we will adopt the first strategy to generate reduced spectra.

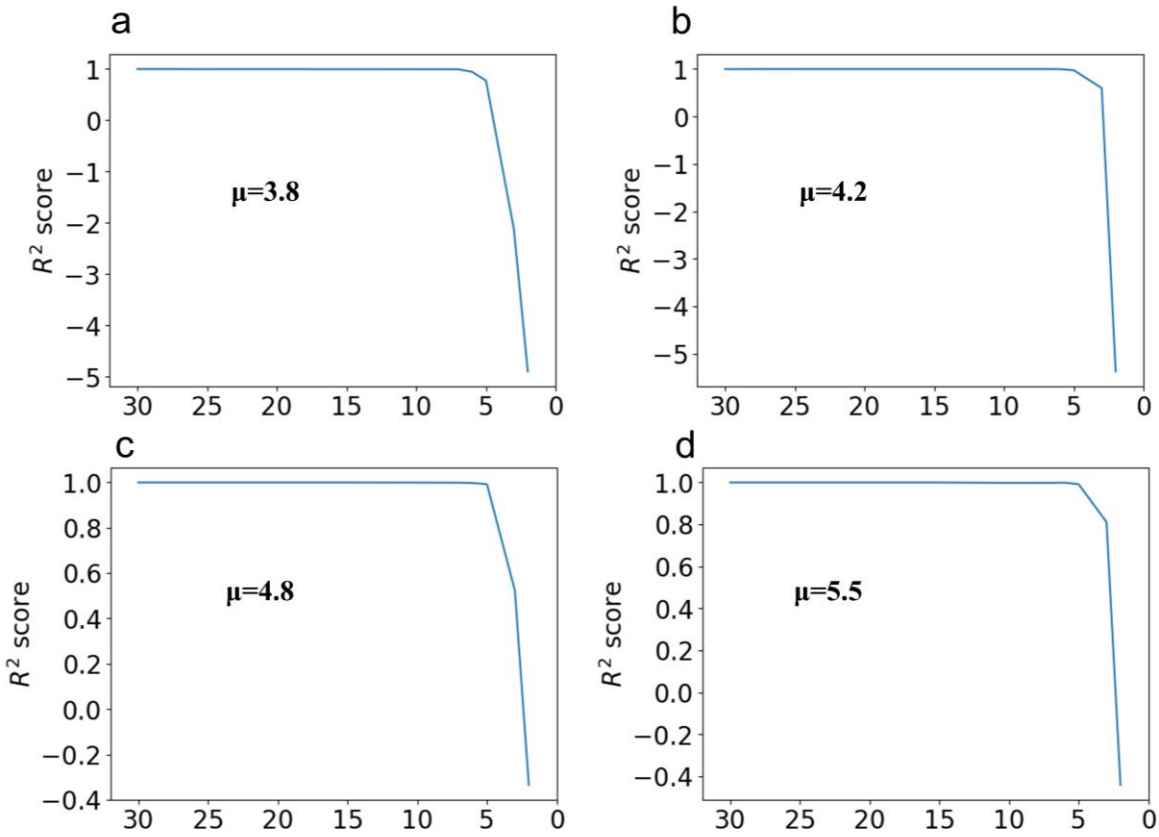

FIG. 6-4. The relationship between the R^2 score and the number of frequency points for different μ, which are (a) 3.8, (b) 4.2, (c) 4.8 and (d) 5.5. The R^2 score between the estimated distribution and the true distribution of MNPs was used.

Table 6-1. Summary of the R^2 score between the distributions estimated from reduced frequency spectra by using the second strategy. The R^2 score between the estimated distribution and the true distribution of MNPs was used.

Frequency range (10 points)	R^2 score of μ=3.8	R^2 score of μ=4.2	R^2 score of $\mu = 4.8$	R^2 score of $\mu = 5.5$
10-100 Hz	-4.77	-3.44	0.75	0.99
100-1000 Hz	0.71	0.97	0.99	0.72
1000-10000 Hz	0.99	0.99	0.66	-2.70

6.2 Analysis of reduced AC magnetization spectra of pH-sensitive ferrogel

In this section, we applied the first strategy mentioned in the previous section to generate reduced spectra by using spectra in Fig. 4-5. Subsequently, we used the method described in **Section** 4.7 to establish the relationship between the sum of estimated x and the concentration of ammonia and calculated the corresponding the R^2 score. Then, we plotted the R^2 score against the number of frequency points (ranging from 30 points to 2 points) in Fig. 6-5. From the results, it was observed that even with only 3 frequency points, the proposed method still achieved a high R^2 score. This finding suggests that our method has the potential to provide accurate estimation with a shorter time interval, indicating its suitability for health monitoring applications that require rapid detection and analysis.

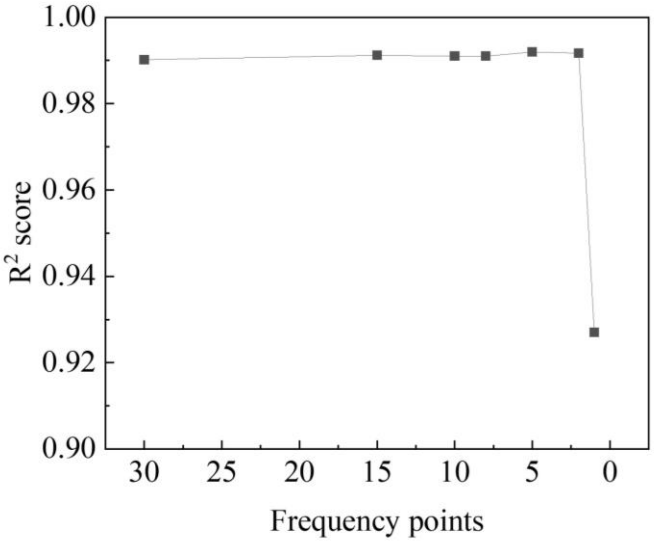

FIG. 6-5. The relationship between the R^2 score and frequency points. The R^2 score between the sum of estimated x and the concentration of ammonia was used.

6.3 Analysis of reduced AC magnetization spectra of biomolecule detection

In this section, we applied the first strategy mentioned in section 6.1 to generate reduced spectra for spectra such as the one shown in Fig. 5-5. Then, we used the methods described in **Section**s 5.2, 5.3, and 5.4 to establish the relationship between the true concentration of SA and the estimated concentration of SA. We calculated the corresponding R^2 score to evaluate the accuracy of the estimation. Finally, we plot the R^2 score against the number of frequency points (ranging from 30 points to 2 points) in Fig. 6-6.

From Fig. 6-6, we obtained similar results to those described in **Section** 6.1. When the number of frequency points was approximately 10 or more, we observed a high R^2 score, indicating accurate estimation. However, when the number of points decreased to 5 or below, a significant decrease in the R^2 score was observed. This decline is reasonable because our

proposed method relies on analyzing the spectra. Therefore, when the number of frequency points is limited, meaning that the information contained in the spectra is insufficient, it is expected that the overall estimation will be compromised.

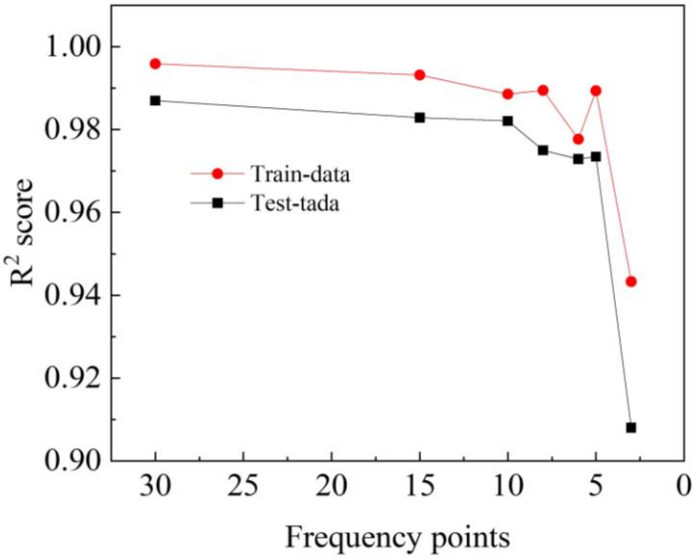

FIG. 6-6. The relationship between the R^2 score and frequency points. The R^2 score between the true concentration of SA and the estimated concentration of SA.

To show the significance of the proposed method on reduced magnetization spectra, we compared our proposed method with a fitting method. Generally, when the number of sampling points is small, usage of a function to fit the sampling points is a possible way. Here an extended Debye relaxation model [3] that was used to fit the AC magnetization spectrum (raw data) as shown in Fig. 6-7. The extended Debye relaxation model is given by

$$M'' = Im\left(\frac{M_0}{[1+(i\omega\tau)^{\alpha}]^{\beta}}\right), \qquad (6-1)$$

where M_0, τ are the fitting parameters representing static magnetization, effective relaxation time, and α, β are the fitting parameters representing the distribution of MNPs. The fitted

results on raw data by Eq. (6-1) are shown in Fig. 6-7. Comparing to the results as shown in Fig. 5-5, the fitted results by the fitting method is obviously inaccurate, which leads to the inaccurate estimation of SA. The reason for the inaccurate fitted results is caused by the extended Debye relaxation model. Although there are fitting parameters in the extended Debye relaxation model existing to represent the distribution of MNPs, the interaction among MNPs inside the clusters is not counted. To count the interaction of MNPs, it is necessary to use some complicated differential equations or to use the proposed method. However, there are still a lot of unclear parts to introduce the interaction term into the differential equations and it might be difficult to solve them. Alternatively, it is possible to use other fitting function such as Gaussian kernel, which leads to the lack of physical meaning, however. Thus, it is better to use our proposed method, which has been proved as correct and physically makes sense.

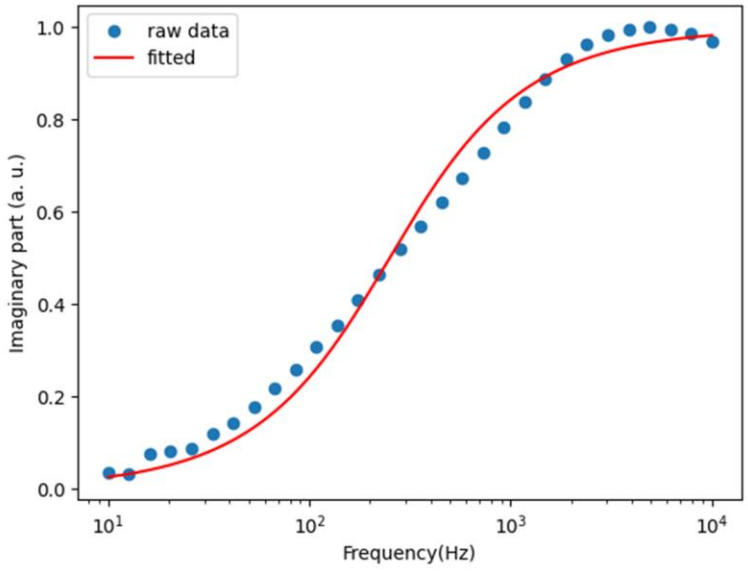

FIG. 6-7. Fitting results of the AC magnetization spectrum when the concentration of SA was 0.94 μM at 2.5 mg/mL biotin modified MNPs as shown in **Section** 5.3.

6.4 Summary

Firstly, we examined the feasibility using simulation data. We used two strategies to reduce the number of frequency points in spectra. After reducing the number of frequency points in the AC magnetization spectra with each of two strategies, we applied our proposed method to the reduced spectra to estimate the distributions of MNPs. From the results, we confirmed the feasibility of the proposed method on the reduced spectra generated by the strategy involving selecting one point out of every few points and discarding the rest as described in **Section** 6.1. Subsequently, we discussed the feasibility of the proposed method to experimental data. We demonstrated the potential of using the proposed method for analyzing the reduced spectra in both ferrogel and liquid biomolecule detection situations. Overall, by exploring the use of our proposed method with reduced frequency points in both simulation and experimental data, we demonstrated its viability as a solution for improving time efficiency of the detection without compromising accuracy.

6.5 Reference

[1] M.E. Villamin, Y. Kitamoto, Effect of Ionic Concentration on Dynamic Magnetic Susceptibility of Iron Oxide Nanoparticles Embedded in Chitosan Hydrogel Matrix, Trans. Magn. Soc. Jpn. Spec. Issues. 3 (2019) 113–119. https://doi.org/10.20819/msjtmsj.19TR322.

[2] S. Bogren, A. Fornara, F. Ludwig, M. del P. Morales, U. Steinhoff, M.F. Hansen, O. Kazakova, C. Johansson, Classification of magnetic nanoparticle systems—synthesis, standardization and analysis methods in the nanomag project, Int. J. Mol. Sci. 16 (2015) 20308–20325. https://doi.org/10.3390/ijms160920308.

[3] C. V. Topping, S. J. Blundell. AC susceptibility as a probe of low-frequency magnetic dynamics, Journal of Physics: Condensed Matter 31.1 (2018) 013001. https://doi.org/10.1088/1361-648X/aaed96

7 General conclusions

In this thesis, A method to analyze the AC magnetization spectra for estimating the information including the hydrodynamic size and the mass concentration of MNPs by solving an inverse problem has been proposed. To analyze the AC magnetization spectra where the interaction among MNPs is not negligible, we proposed an experimental model rather than Debye relaxation model. The feasibility of the proposed method was investigated on simulation data. Then, the proposed method was applied onto experimental data and the relationship between the estimated information of MNPs and target molecules was established for demonstrating the detection of ammonia gas (where the interaction of MNPs was negligible) and streptavidin (where the interaction of MNPs was not negligible). The main conclusions of this works can be summarized in the following points.

1. The feasibility of the proposed method on the simulation data for estimating the hydrodynamic size distribution and the mass concentration of MNPs was confirmed, even if the distribution of MNPs was multimodal and the mass concentration of MNPs was various. In addition, we confirmed that there is almost no difference between the results estimated from the imaginary part and those from the real and imaginary part, in terms of simulation data.
2. pH-sensitive ferrogels with the pH-responsiveness in the alkaline region were successfully synthesized. The ferrogels with larger swelling ratios exhibited enhanced Brownian relaxation during AC magnetization. Based on the pH response of the AC magnetization, the detection of ammonia gas was investigated using the ferrogel as a

sensing label. An assumption was established that the concentration of absorbed ammonia gas corresponds to the mass concentration of rotatable MNPs. By using the above assumption, the concentration of absorbed ammonia gas was successfully detected by the mass concentration of rotatable MNPs estimated via the proposed method with a high R^2 score.

3. An experimental model was established by the AC magnetization spectra of MNP clusters. The experimental model was used for estimating the hydrodynamic size distribution of MNP clusters from AC magnetization spectra of mixture of biotinylated MNPs and streptavidin. The estimated distributions were consistent with the hydrodynamic results obtained by DLS measurements. We assumed that there is a linear relationship between the number of streptavidin molecule and the number of the estimated clusters. The estimated concentration of streptavidin from the MNP cluster distributions was well correlated with the true concentration of streptavidin by using the linear regression. In addition, we confirmed the necessity of selecting appropriate MNP clusters to cover the range of hydrodynamic sizes of MNP-SA clusters. Moreover, the proposed method showed both wider detection range of streptavidin and the high R^2 score than the relaxation frequency based method.
4. The proposed method was applied to the reduced spectra to estimate the information of MNPs. We confirmed the feasibility of the proposed method on the reduced simulation data. Subsequently, we demonstrated the potential of using the proposed method for analyzing the reduced spectra in both ferrogel and liquid biomolecule detection situations for biosensing.

Knowledge obtained from this study will contribute to other works such as ferrogel-based biosensors and magnetic susceptometry based biosensing based biosensing. For ferrogel-based biosensors, as the magnetic response of the synthesized ferrogels is caused by the swelling behavior of the hydrogel and the hydrodynamic phenomena of the MNPs, the combination of MNPs with a stimuli responsive hydrogel should broaden the application range of ferrogel-based biosensors. For magnetic susceptometry based biosensing based biosensing, as our proposed method showed the potential for estimating the distributions of MNP clusters from AC magnetization, it is possible to establish a more precise relationship between MNPs and biomolecules such as the linear model described in **Section** 5.4 instead of only using the relaxation time.

Finally, here are some recommendations for the further research.

1. In this study, because of the complexity of modeling the interaction among MNPs, we used an experimental model based on the measured AC magnetization spectra of MNPs. To more accurately describe the interaction among MNPs with the existence of biomolecules, we believe that the development of a theoretical model and simulation tools for describing such interaction is important.
2. In this study, the involvement of small biomolecules was ignored. Further investigation of the effect of the biomolecule size on the MNP clusters formed by the aggregation of MNPs and biomolecules is needed.
3. In this study, the established model linking the distribution of MNP clusters to the number of target molecules was linear. We believe that further investigation of the relationship between the MNP clusters and the amount of biomolecules will improve the proposed method.

Acknowledgements

I would like to express my sincerest gratitude to my supervisor, Professor Yoshitaka Kitamoto who has been providing me with precise opportunity for studying, valuable guidance and continuous supports for whole of my study. Without his help and advice, I would not be where I am today.

I am deeply grateful to my co-supervisor, Professor Konstantinos Slavakis, without whose able supervision it is impossible to propose the method described in the present study to analyze AC magnetization spectra.

I wish to express gratitude to Assistant Professor Kyohei Okubo for his warm encouragement and valuable supports during toughest time of my doctoral course.

I would like to express my appreciation to my thesis panels: Professor Masato Sone, Associate Professor Tso Fu Mark Chang, Associate Professor Toshinori Fujie, and Associate Professor Tomohiro Hayashi for their constructive comments, sincere suggestions, and honest assessments that helped to improve this dissertation.

I would like to thank all members of Kitamoto laboratory for their help, encouragement, and honest conversations during my days at Tokyo Institute of Technology.

I am very in debt to Cross the border! Tokyo Tech Pioneering Doctoral Research Project for financial supports during the last two years of my doctoral study.

At last, but not the least, I would like to express my thanks to my family and friends in all aspects of my student life.

Accomplishment

Journal publications

1. Y. Chen, K. Okubo, K. Slavakis, Y. Kitamoto, Estimation of amount of biomolecule via distribution of magnetic nanoparticle clusters analyzed from AC magnetization spectra for magnetic biosensing, J. Magn. Magn. Mater. 588 (2023) 171387. https://doi.org/10.1016/j.jmmm.2023.171387.

2. Y. Chen, M. Abe, I. Tomita, Y. Kurashina, Y. Kitamoto, Synthesis and characterization of pH-responsive ferrogels comprising sulfamethazine-based polymer and magnetic nanoparticles for sensing ammonia gas, J. Magn. Magn. Mater. 565 (2023) 170201. https://doi.org/10.1016/j.jmmm.2022.170201.

Presentations

International conference (oral presentation)

1. Y. Chen, K. Okubo, K. Slavakis, Y. Kitamoto, A Machine Learning Based Analysis Method of AC Magnetization Spectra for Estimating Cluster Distribution of Magnetic Nanoparticles, IEEE International Magnetics Conference 2023 (Intermag 2023), Sendai, Japan, May 2023.

2. Y. Chen, K. Slavakis, Y. Kitamoto, A Machine Learning Based Analysis Method of AC Magnetization Spectra of Magnetic Nanoparticles and Its Application to Magnetic Biosensing, International Conference on Fine Particle Magnetism 2022 (ICFPM 2022), Yokohama, Japan, October 2022.

3. Y. Chen, M. Abe, Y. Kurashina, Y. Kitamoto, Study on ferrogel composed of pH-responsive hydrogel and iron oxide nanoparticles for biogas sensing, 20th Interfinish World Congress (INTERFINISH 2020), Online, September 2021.

Domestic conference (oral presentation)

1. Y. Chen, X. Xu, K. Slavakis, Y. Kitamoto, Analysis of AC magnetization of Magnetic nanoparticles for biosensing, Spring Meeting of the Japan Society of Powder and Powder Metallurgy 2023, Tokyo, Japan, June 2023.

2. Y. Chen, M. Abe, Y. Kurashina, Y. Kitamoto, Synthesis of composite hydrogels composed of pH-responsive polymer and iron-oxide nanoparticles, Spring Meeting of the Japan Society of Powder and Powder Metallurgy 2021, Tokyo, Japan, June 2021.

Awards

1. 20th Interfinish World Congress (INTERFINISH 2020), Student Awards.
2. Research grant, Kato Foundation for Promotion of Science, 2021.